A search for supersymmetry using the α_T variable with the CMS detector and the impact of experimental searches for supersymmetry on supersymmetric parameter space

Samuel Rogerson

Imperial College London
High Energy Physics Department

A thesis submitted to Imperial College London
for the degree of Doctor of Philosophy

Declaration

The work presented in this thesis is a result of the author's studies and research between October 2009 and April 2013. It was carried out with the support of the Imperial College High Energy Physics group, the CMS collaboration, and the Mastercode group. Any work of others included is explicitly referenced.

In the case of the experimental analysis, Chapter 4, the author's main contributions were in developing and making use of the likelihood models, and producing the final results of the analysis.

Samuel Rogerson

The copyright of this thesis rests with the author and is made available under a Creative Commons Attribution Non-Commercial No Derivatives licence. Researchers are free to copy, distribute or transmit the thesis on the condition that they attribute it, that they do not use it for commercial purposes and that they do not alter, transform or build upon it. For any reuse or redistribution, researchers must make clear to others the licence terms of this work

Abstract

A search for supersymmetry in final states with jets and missing transverse energy is performed in pp collisions at a centre-of-mass energy of $\sqrt{s} = 7\text{TeV}$. The data sample corresponds to 4.98fb^{-1} collected by the CMS experiment at the LHC in 2011. A dimensionless kinematic variable is used as the main discriminant between genuine and misreconstructed signal events. The search is performed in a signal region binned according to the scalar sum of the transverse energy of jets and the number of jets identified as originating from a bottom quark. The limits are presented in the parameter space of the Constrained Minimal Supersymmetric Standard Model (cMSSM) as well as in simplified models with particular attention paid to compressed spectra and third-generation models.

Global frequentist fits to the cMSSM and a non-universal Higgs model are also performed using the `Mastercode` framework incorporating recent experimental constraints, similar to those those presented here. Global likelihood contours are presented in the parameter planes of both the cMSSM and NUHM1, as well as a selection of 1D likelihood functions for observables.

Contents

List of Figures

Chapter 1

Introduction

The Standard Model (SM) of particle physics has proved immensely successful in accurately describing and predicting the varied phenomenology discovered in particle physics over the last several decades. There are however several areas where the SM is incompatible or incongruous with observation. As such, models of Supersymmetry (SUSY) have been proposed to remedy these issues and have been met with enthusiasm from both the theoretical and experimental communities. Detailed in this document is a search for SUSY performed at the Large Hadron Collider (LHC) as well as a detailed analysis of the impact of such searches on the parameter space of supersymmetric models.

In Chapter 2 a brief introduction and overview of the constituent particles of our universe and their governing rules is given,this is developed into an overview of the construction of the SM of particle physics. Particular attention is paid to the areas in which the SM may be either insufficient or inaccurate. These are used to motivate the existence of Beyond Standard Model (BSM) theories, of which SUSY is introduced as a key example to solve the problems facing the SM. A discussion of the minimal supersymmetric extension to the SM is given, along with derived types of supersymmetric models to be analysed in the latter portions of this document.

Chapter 3 details the specification and design of the LHC in general and the experimental components involved in the analysis of Chapter 4. Specifically the design objectives and a breakdown of the components of the Compact Muon Solenoid (CMS) detector and their performance is presented component by component with particular emphasis on their involvement in the measurement of Missing Transverse Energy ($E_{\mathrm{T}}^{\mathrm{miss}}$) signals.

Chapter 4 describes the experimental analysis carried out, in which the author was involved in the statistical analysis and limit setting procedure. The Chapter provides a background on the event selection procedures, breakdown of montecarlo samples used and the methods employed for background estimation. The results and impact of this $E_{\mathrm{T}}^{\mathrm{miss}}$ SUSY search are shown in a full SUSY model as well as several phenomenologically simplified models.

In Chapter 5 a method for the exploration and analysis of the parameter space of supersymmetric models is presented. Two models are extensively sampled and explored applying electroweak precision constraints in the first instance. In the second instance the state of the models are compared before and after applying constraints originating in the LHC-era and those coming from direct dark matter searches. The impact on the viable area of parameter space and the agreement of the models with observation is shown as well as the likelihood functions for various observables.

Finally Chapter 6 gives a brief discussion on the state of searches for SUSY and the prospects for further encroachment upon the parameter space of the benchmark models.

Chapter 2

Theory

This introductory chapter gives the necessary theoretical context for the work described in the subsequent chapters and details the current state of the Standard Model of particle physics as well as possible extensions. In particular, models of Supersymmetry are discussed and their possible phenomenology detailed.

2.1 The Standard Model

The SM describes the behavior of particles at the subnuclear scale, the scale at which the constituent particles of a nucleus become apparent.

2.1.1 Overview of particle content and phenomenology of the Standard Model

The SM contains both types of particles described in Quantum Mechanics (QM), that is fermions and bosons, and describes the interaction of these through the electromagnetic, weak and strong forces which are in turn described in detail in Sections 2.1.3, 2.1.5, and 2.1.4 respectively.

Fermions, which have half integer spin and hence obey the Pauli Exclusion Principle, make up the matter of the universe. They are subdivided into leptons and quarks, which can each be divided again into three generations. Each generation of leptons contains an electromagnetically charged particle (ℓ) and a neutral neutrino (ν_ℓ). The charged leptons participate in both electromagnetic and weak interactions, where as the neutral neutrinos only interact through the weak force. All three generations of quarks interact through the electromagnetic and weak forces as well as carrying colour charge and therefore strongly interacting.

The chirality of a particle is defined by whether a particle transforms in a right or left-handed representation of the Poincaré group[1]. One can also define handedness, the projection of a particle's spin along its momentum vector. In the massless limit chirality and handedness are identical. When left-handed particles are referred to in the text, this refers to left-chiral particles. In the case of spinors, i.e. those transforming under the $SU(2)$ symmetry, a particle can have both left and right-handed component. Therefore to separate the components it is necessary to define projection operators for handedness.

To define a projection operator of handedness we start by introducting the Gamma Matrices, a set of matrices that form a set of basis vectors for Minkowski space, defined by the anti-commutation relation

$$\{\gamma^\mu, \gamma^\nu\} = \gamma^\mu \gamma \nu + \gamma^\mu \gamma \nu = 2\eta^{\mu\nu} \tag{2.1}$$

where $\eta^{\mu\nu}$ is the metric for Minkowski spacetime. We can further define γ^5,

$$\gamma^5 = i\gamma^0\gamma^1\gamma^2\gamma^3 \tag{2.2}$$

though this does not form part of the set of basis vectors. Defining projection operators,

[1]This is the group of all possible isometries of Minkowski space-time, i.e. a 3 space-like 1 time-like dimension manifold.

	Per Generation	Q	Colour
Leptons	$\binom{\nu_\ell}{\ell}_L \; \ell_R$	$\begin{matrix}0\\1\end{matrix}$	-
Quark	$\binom{U}{D}_L \; \begin{matrix}U_R\\D_R\end{matrix}$	$\begin{matrix}+2/3\\-1/3\end{matrix}$	RGB

Table 2.1: List of SM particles, where there are three generations $\ell \in \{e, \mu, \tau\}$, $U \in \{u, c, t\}$ and $D \in \{d, s, b\}$

$$P_L = \frac{1-\gamma^5}{2} \tag{2.3}$$

$$P_R = \frac{1+\gamma^5}{2} \tag{2.4}$$

which satisfy

$$P^2_{L,R} = P_{L,R}, P_L P_R = P_R P_L = 0 \tag{2.5}$$

it can be shown that these are indeed the projection operators for chirality[99].

The electroweak force (unified electromagnetic and weak forces) distinguishes between Left Handed (LH) and Right Handed (RH) particles resulting in each generation containing LH particles in doublets and RH particles in singlets, as shown in Table 2.1. In addition to lepton flavour the only difference between the generations of particles are the masses of the leptons and quarks.

In the SM the interactions of the fundamental forces are described by the exchange of intermediate integer spin particles called bosons, each force having one or more of these bosons mediating the interactions. The electromagnetic force is mediated by the photon γ. The weak force can be split into two separate groups of interactions: the charged and neutral current interactions, which are mediated by the $W^{\pm}$ boson and linear combinations of the Z^0 boson and the photon respectively. The strong force is mediated by eight gluons, denoted $g_{i=1,\ldots,8}$.

Naively one may expect all interactions to conserve quantum numbers: parity P, charge conjugation C, time reversal T, lepton number L, baryon number B and the various other flavour quantum numbers. These quantum numbers *are* conserved in the case of the electromagnetic, photon mediated, and strong, gluon mediated, forces; the interactions for these forces only occur between particles of the same generation. While the combination of Z^0 and γ means that the weak neutral current interactions behave identically for LH and RH particles, the charged current interacts *only* with LH particles. This means that, for the charged current, parity and charge conjugation are violated maximally.

The fact that only some of forces have massive bosons (the charged and neutral bosons of the weak force) indicates that a difference in phenomenology may be expected between these forces and those with massless mediators. The photon being massless leads to the prediction of an infinite range for the electromagnetic forces, whereas the massive $W^{\pm}$ and Z^0 predict that the range of the weak force is between 10^{-17} and 10^{-16}m.

Though the strong force is mediated by massless gluons, it too is range limited. While any non-abelian force can self interact, gluons are unique in the SM as they also carry charge for the force that they mediate and so self-interact alogn their propagators. Gluon-gluon self-interactions constrain the colour fields to string-like objects which exert constant attractive force between the gluons regardless of their separation distance. Because of this constant force gluons are confined to composite particles, hadrons, effectively limiting the range of the strong force to $\sim 10^{-15}$m, which is approximately the size of an atomic nucleus.

Each of the forces have a characterizing coupling constant α. These are dependent on the energy scale μ. In Quantum Electrodynamics (QED) electrons can emit virtual photons which in turn can decay to electron-positron pairs, this means that the original electron is surrounded by a 'cloud' of other electrons that *screen* its bare charge. This means that the measurement of the charge of the electron Q depends on the distance of test charged used in measuring. Once the test charge is sufficiently close it penetrates the cloud that screens the electrons bare charge and so Q is measured at an increased value. This screen charging effect applies similarly, but in an opposite fashion, in Quantum Chromodynamics (QCD). Self-interactions of the gluon leads to "asymptotic freedom". For instance, if there were two quarks each with color $\mathcal{C}$ they would interact asymptotically via colour fields of reduced strength resulting in a state where they behave as essentially free, non-interacting particles[72].

2.1.2 Development of Quantum Electrodynamics

Attempts to describe atomic processes using the non-relativistic Schrödinger equation[106] yielded accurate results, but failed to described fine and hyperfine structures[107]. This led to attempts to combine QM and (relativistic) classical electromagnetism, resulting in Dirac formalizing Relativistic Quantum Mechanics (RQM)[54]. One test of this was a prediction of the electron's magnetic moment $\vec{\mu_{\mathrm{e}}}$,

$$\vec{\mu_{\mathrm{e}}} = -g_e \frac{e}{2m_{\mathrm{e}}} \vec{S} \tag{2.6}$$

The prediction for this from RQM was well known and gave a value of the gyromagnetic ratio $g_e = 2$ exactly. This led to the characterization of what is known as the anomalous magnetic moment of a lepton $\left(g_\ell - 2\right)$. Unfortunately measurement showed a significant deviation from $g_e = 2$, i.e. a non-zero $\left(g_\ell - 2\right)$. This, in turn, led to the combination of electromagnetism and Quantum Field Theory (QFT) into QED and solved the $\left(g_\ell - 2\right)$ problem for electrons, giving one of the most accurately verified predictions in history[67, 96].

2.1.3 Quantum Electrodynamics

Quantum Electrodynamics, and the SM as a whole, is formulated as a gauge theory. That is, there exist redundant degrees of freedom in the Lagrangian, transformations under which form a symmetry group. Starting from the Lagrangian used to describe a Dirac field,

$$\mathcal{L}_{\mathrm{Dirac}} = \bar{\psi}(i\not{\partial} - m)\psi \tag{2.7}$$

where ψ denotes the Dirac field, $\bar{\psi} \equiv \psi^\dagger\gamma^0$ is the adjoint of the field, $\not{X} \equiv \gamma^\sigma X_\sigma$ and the γ^σ matrices are the same as those defined in equation (2.1).

This Lagrangian is *not* invariant under the local gauge transformation of the $U(1)$ symmetry group,

$$\psi \to \psi' = e^{-i\alpha(x)}\psi \tag{2.8}$$

By introducing the gauge field A_μ and defining

$$D_\mu = \partial_\mu + ieA_\mu \tag{2.9}$$

equation (2.7) will be invariant under the gauge transformation of equation (2.8) if

$$A_\mu \to A_\mu + \frac{1}{e}\partial_\mu \alpha. \tag{2.10}$$

This implies that there is a coupling between electrons and A_μ the electromagnetic force which arises naturally when local gauge invariance is required.

To complete the QED Lagrangian we also need to include a term for the electromagnetic field tensor $F_{\mu\nu}$ which describes the kinematics of the free fields,

$$F_{\mu\nu} = \partial_\mu A_\nu - \partial_\nu A_\mu \tag{2.11}$$

which is gauge invariant. This gives the QED Lagrangian

$$\mathcal{L}_{\text{QED}} = -\frac{1}{4}F_{\mu\nu}F^{\mu\nu} + \bar{\psi}(i\not{\partial} - e\not{A} - m)\psi \tag{2.12}$$

2.1.4 The strong force

Analogous to the fashion of how the electromagnetic force (QED) is formalized using the symmetry of the $U(1)$ group, the strong force's description uses the $SU(3)$ group and is denoted $SU(3)_C$.

In the same way as for electrodynamics, we need to satisfy a local gauge invariance[116],

$$q(x) \to e^{i\alpha_a(x)T_a}q(x) \tag{2.13}$$

Where $a = 1, \ldots, 8$ and enumerates the eight gluons and T_a are the generators of the symmetry group $SU(3)_C$.

Since gluons carry colour charge and self-interact, an additional term is required to maintain gauge invariance of the Lagrangian

$$G^a_\mu \to G^a_\mu - \frac{1}{g}\partial_\mu \alpha_a - f_{abc}\alpha_b G^c_\mu \tag{2.14}$$

Giving the QCD Lagrangian as

$$\mathcal{L}_{\text{QCD}} = \bar{q}(\gamma^\mu \partial_\mu - m)q - g_s(\bar{q}\gamma^\mu T_a q)G^a_\mu - \frac{1}{4}G^a_{\mu\nu}G^{\mu\nu}_a \tag{2.15}$$

Where the first term describes free quarks, the second gluon-quark interactions and the final term describes gluon self-interaction.

2.1.5 Electroweak unification

The first attempt at describing the weak interactions came about via attempts to explain beta-decays through a four-body interaction involving electrons, neutrinos, protons, and neutrons[64],

$$\mathcal{L}_{\text{Fermi}} = \frac{G_F}{\sqrt{2}}\left(\bar{\psi}_p \gamma_\mu \psi_n\right)\left(\bar{\psi}_e \gamma^\mu \psi_\nu\right) \tag{2.16}$$

However, this Lagrangian is *neither* gauge invariant nor renormalizable[71], hence cannot give predictions at energy scales $E \sim \mathcal{O}(100\text{GeV})$. The theory can be rescued by introducing intermediate vector bosons, the weak interaction's equivalent of the photon in electromagnetism.

At this point it can be useful to have a description combining both the electromagnetic and weak interactions. The gauge theory for QED used the $U(1)$ symmetry group and it is necessary to preserve this behavior after the symmetry imposed for unification is broken. As such, we form a cross product of two symmetry groups, $SU(2)$ and $U(1)$ denoted,

$$SU(2)_L \otimes U(1)_Y \tag{2.17}$$

where the subscript L denotes that the $SU(2)$ symmetry is for LH particle components, and the subscript Y denotes weak hypercharge which is defined via

$$Q = T_3 + \frac{Y}{2} \tag{2.18}$$

where Q is the electric charge and T_3 is the third component of the weak isospin, a quantum number for the weak force that delineates identically behaved particles that have different electrical charge. This relationship is known as the Gell-Mann Nishijima relationship[95, 68],

The gauge fields that arise from these groups are,

$$SU(2)_L \rightarrow W_\mu^{1,2,3} \tag{2.19}$$

$$U(1)_Y \rightarrow B_\mu \tag{2.20}$$

Particles are now organized in LH doublets and RH singlets, as in Table 2.1, e.g. for the first generation

$$L = \begin{pmatrix} \nu_e \\ e \end{pmatrix}_{LL}, R = e_R \tag{2.21}$$

The result of this arrangement is that the neutrino of the LH doublet has the third $SU(2)$ isospin projection $T_3 = +\frac{1}{2}$, the electron has $T_3 = -\frac{1}{2}$ and both LH particles have hypercharge $Y = -1$, whereas the RH singlet has $Y = -2$ and substituting these values into equation (2.18) gives the correct charge for the various particles.

To write down the Lagrangian for this theory the covariant derivative needs to be defined as well as the gauge bosons' stress tensor. The covariant derivative is defined differently for LH and RH states,

$$D_\mu L = \left(\partial_\mu - ig_1 \frac{\tau^a}{2} W_\mu^a - ig_2 \frac{Y_H}{2} B_\mu - ig\right) \tag{2.22}$$

$$D_\mu R = \left(\partial_\mu + ig_2 \frac{Y_H}{2} B_\mu\right) \tag{2.23}$$

where g_1 and g_2 are the coupling constants associated with the symmetry group and τ^a are the $SU(2)$ generators.

The gauge fields' stress tensors are $W_{\mu\nu}^i$ and $B_{\mu\nu}$ defined as,

$$W_{\mu\nu}^i \equiv \partial_\mu W_\nu^i - \partial_\nu W_\mu^i + g\epsilon^{ijk} W_\mu^j W_\nu^k, \tag{2.24}$$

$$B_{\mu\nu}^i \equiv \partial_\mu B_\nu - \partial_\nu B_\mu \tag{2.25}$$

where ϵ^{ijk} is the Levi-Civita symbol, the fully anti-symmetric matrix.

We can now write down the full electroweak Lagrangian for one lepton family,

$$.\mathcal{L}_{\mathrm{EWK}} = \bar{R} i \not{D} R + \bar{L} i \not{D} L + \frac{1}{4} W_{\mu\nu}^i W^{\mu\nu i} - \frac{1}{4} B_{\mu\nu} B^{\mu\nu} \tag{2.26}$$

While this is considerably more complex than the simple QED case given in equation (2.12), the charged gauge bosons of the weak interaction can be defined such that $\mathcal{L}_{\mathrm{Fermi}}$, equation (2.16), is the low energy limit of $\mathcal{L}_{\mathrm{EWK}}$ (equation (2.26)).

In the limit of low energy the physical states are defined by

$$W_\mu^\pm = \frac{1}{\sqrt{2}} (W_\mu^1 \mp W_\mu^2) \tag{2.27}$$

and the coupling constant g is defined relative to G_F,

$$\frac{g^2}{4\sqrt{2}} = M_W^2 G_F \tag{2.28}$$

The the theory must also produce the heavy neutral boson Z_μ and the electromagnetic force's A_μ,

$$\begin{pmatrix} A_\mu \\ Z_\mu \end{pmatrix} = \begin{pmatrix} \cos\theta_W & \sin\theta_W \\ -\sin\theta_W & \cos\theta_W \end{pmatrix} \begin{pmatrix} B_\mu \\ W_\mu^3 \end{pmatrix} \tag{2.29}$$

where θ_W is the weak mixing angle[124],

$$\cos\theta_W = \frac{g_1}{\sqrt{g_1^2 + g_2^2}} \tag{2.30}$$

The electromagnetic coupling constant (i.e. charge) is then

$$e = g\sin\theta_W \tag{2.31}$$

The extension of the electroweak symmetry group $SU(2)_L \otimes U(1)_Y$ described here, with $SU(3)_C$ described in Section 2.1.4 giving $SU(3)_C \otimes SU(2)_L \otimes U(1)_Y$ gives the gauge group of the SM.

2.1.6 The Higgs mechanism

One of the main missing pieces of the SM so far is the origin the particles' masses. The electroweak Lagrangian, equation (2.26), does not contain mass terms for the particles because these would violate the symmetry. Mass terms would be of the form

$$m^2\bar{\psi}\psi \tag{2.32}$$

and since these would contain both ψ_L and ψ_R which transform differently the gauge invariance would be broken.

However, scalar fields could have mass terms which do not break gauge invariance. The Higgs mechanism[62, 77, 85, 74, 78] is based on inserting a scalar doublet into the

SM to create mass terms, making use of spontaneously breaking the symmetry of the lagrangian.

The spontaneous breaking of a *global* symmetry of the lagrangian results in the appearance of massless spinless particles, named the Goldstone bosons[69, 70]. If a local gauge symmetry is spontaneously broken, the degrees of freedom associated with the Goldstone bosons become longtudinal degress of freedom, meaning that these bosons become massive. There is a massive vector boson that corresponds to each of the Goldstone bosons. It should be noted that, in the SM while we require massive $W^{\pm}$ and Z vector bosons, we also require that the photon, γ, remain massless. Therefore the symmetry breaking pattern must preserve the $U(1)$ symmetry, that is

$$SU(2)_L \otimes U(1)_Y \rightarrow U(1)_{\mathrm{EM}}, \tag{2.33}$$

To achieve this we start by looking at the lagrangian for a scalar field Φ

$$\mathcal{L}_{\mathrm{Higgs}} = (D_\mu \Phi)^\dagger (D^\mu \Phi) - V\big(\Phi^\dagger, \Phi\big) \tag{2.34}$$

where D_μ is the covariant derivative

$$D_\mu = \partial_\mu - ig_2 \frac{\tau_a}{2} W_\mu^a - ig_1 \frac{Y_H}{2} B_\mu - ig_s \frac{\lambda_a}{2} G_\mu^a \tag{2.35}$$

and $V\big(\Phi^\dagger, \Phi\big)$ is the potential

$$V\big(\Phi^\dagger, \Phi\big) = \mu^2 \Phi^\dagger \Phi + \lambda \big(\Phi^\dagger \Phi\big)^2 \tag{2.36}$$

which is termed the *mexican hat potential* and can be seen in Figure 2.1,

To break the $SU(2)_L \otimes U(1)_Y$ symmetry, we must choose Φ to have a non-vanishing hypercharge and weak isospin. As we are attempting to give three vector bosons mass, this is the number of Goldstone bosons required. Hence we can choose to decompose Φ as

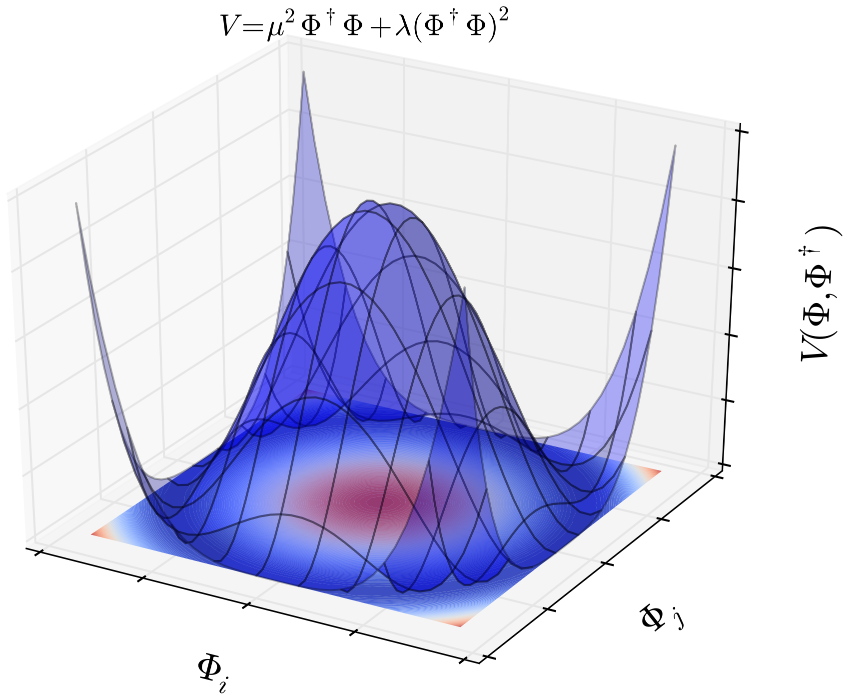

Figure 2.1: A view of a version of the potential in $\mathcal{L}_{\mathrm{higgs}}$ where we only use two components for simplicity. The continuous circular group of minima is clearly visible

$$\Phi = \begin{pmatrix} \Phi^+ \\ \Phi^0 \end{pmatrix} = \frac{1}{\sqrt{2}} \begin{pmatrix} \Phi_1 + i\Phi_2 \\ \Phi_3 + i\Phi_4 \end{pmatrix} \tag{2.37}$$

where Φ_i are all real fields. We must ensure that the potential term of Φ's lagrangian is bounded from below therefore restricting $\lambda > 0$. Further choosing $\mu^2 < 0$ results in the potential shown in Figure 2.1 where there is an infinite number of minima present, occuring at the value

$$\Phi^\dagger \Phi = -\frac{\mu^2}{2\lambda} \tag{2.38}$$

Recalling that

$$\Phi^\dagger\Phi = \frac{1}{2}\left(\Phi_1^2 + \Phi_2^2 + \Phi_3^2 + \Phi_4^2\right) = \frac{1}{2}\Phi_i\Phi^i \tag{2.39}$$

These minima correspond to an infinite number of arrangement of the components of Φ, and the spontaneous breaking of the $SU(2)_L \otimes U(1)_Y$ symmetry will occur once one of these minima is chosen. We can this make the simplest choice of

$$\Phi_1 = \Phi_2 = \Phi_4 = 0, \Phi_3^2 = -\frac{\mu^2}{\lambda} \equiv \nu^2 \tag{2.40}$$

such that the vacuum expectation value of Φ is now,

$$\langle\Phi\rangle_0 \equiv \langle 0|\Phi|0\rangle = \frac{1}{\sqrt{2}}\begin{pmatrix} 0 \\ \nu \end{pmatrix} \tag{2.41}$$

Recalling we can express the field Φ in the exponential form,

$$\Phi_{\text{vacua}}(x) = \frac{1}{\sqrt{2}} e^{i\theta_a(x)\tau^a(x)/\nu}\begin{pmatrix} 0 \\ \nu + h(x) \end{pmatrix} \tag{2.42}$$

then, making use of the unitary gauge[125]

$$\Phi(x) \rightarrow \Phi'(x) = e^{-i\theta_a(x)\tau^a(x)/\nu}\Phi(x) = \frac{1}{\sqrt{2}}\begin{pmatrix} 0 \\ \nu + h(x) \end{pmatrix} \tag{2.43}$$

we can see that we have removed the three θ_a fields, chosen a specific direction for the minima, and broken three of the four global symmetries of the Lagrangian in equation (2.39).

We can now take our gauge transformed field $\Phi'(x)$ and put this back into the Lagrangian equation (2.34). Concentrating on the kinetic term, and dropping the $'$ for convenience

$$(D^\mu\Phi)^\dagger(D_\mu\Phi) \equiv |D_\mu\Phi|^2 = \left|\left(\partial_\mu - ig_2\frac{\tau_a}{2}W_\mu^a - ig_1\frac{Y_H}{2}B_\mu\right)\right| \tag{2.44}$$

Expanding this around the minimum we get

$$
\begin{aligned}
|D_\mu \Phi|^2 &= \frac{1}{2}(\partial^\mu h)^2 \\
&+ \frac{g_2^2}{8}(\nu + h)^2 (W_1^\mu + iW_2^\mu)(W_\mu^1 - iW_\mu^2) \\
&+ \frac{1}{8}(\nu + h)^2 \left(g_2 W_3^\mu - g_1 Y_H B^\mu\right)^2
\end{aligned} \tag{2.45}
$$

And collecting together relevant terms,

$$
\begin{aligned}
|D_\mu \Phi|^2 &= \frac{g_2^2 \nu^2}{8} \left(W_1^\mu + iW_\mu^2\right)\left(W_\mu^1 - iW_\mu^2\right) \\
&+ \frac{\nu^2}{8} \left(g_2 W_3^\mu - g_1 Y_H B^\mu\right)^2 \\
&+ \frac{1}{2} \left(\partial^\mu h\right)^2 + \ldots
\end{aligned} \tag{2.46}
$$

We can see that the first term is $(M_W^2) W_\mu^+ W^{-\mu}$ where we have made the identification

$$
W^\pm = \frac{1}{\sqrt{2}} \left(W_\mu^1 \mp iW_\mu^2\right) \tag{2.47}
$$

$$
M_W = \frac{g_2 \nu}{2}. \tag{2.48}
$$

Making use of equation (2.28) we can solve for ν in terms of known parameters

$$
\nu = \frac{1}{(\sqrt{2} G_F^{1/2}} \simeq 246 \mathrm{GeV} \tag{2.49}
$$

Finally the second term of equation (2.46) involves the two neutral components of the gauge fields. If we construct the following linear combinations of W_3^μ and B_μ,

$$A_\mu = \frac{g_1 B_\mu + g_2 W_\mu^3}{\sqrt{g_1^2 + g_2^2}} \tag{2.50}$$

$$Z_\mu = \frac{-g_1 B_\mu + g_2 W_\mu^3}{\sqrt{g_1^2 + g_2^2}} \tag{2.51}$$

we can then see that second term of equation (2.46) is actually of the form $(\frac{1}{2}M_Z^2)Z_\mu Z^\mu$ with

$$M_Z = \frac{1}{2}\nu\sqrt{g_1^2 + g_2^2} \tag{2.52}$$

In a similar fashion to this, mass is given to the leptons and gauge invariance is maintained by using Yukawa couplings[127, 99] between the leptons and the higgs field,

$$-G_\ell \left[\bar{R}\big(\Phi^\dagger L\big) + \text{h.c.}\right] = -\frac{G_\ell(\nu + h)}{\sqrt{2}}\big(\bar{\ell}_R \ell_L + \bar{\ell}_L \ell_R\big) \tag{2.53}$$

where G_ℓ is the Yukawa constant, ℓ is one of the lepton generations $\ell \in e, \mu, \tau$ and h.c. denotes a hermitian conjugate of the previous term. From this it can be shown that $m_\nu = 0$ and $m_\ell = G_\ell \nu\sqrt{2}$. And the value of the Yukawa coupling of the lepton with the Higgs is specified as,

$$C_{\ell\ell H} = \frac{M_\ell}{\nu} \tag{2.54}$$

and hence the coupling is proportional to the mass of the lepton.

2.1.7 Beyond the Standard Model

While the lack of terms for neutrino masses indicates physics beyond the SM there is other significant evidence for entirely new regimes of physics at or above the TeVenergy scale. These are summarised in this section.

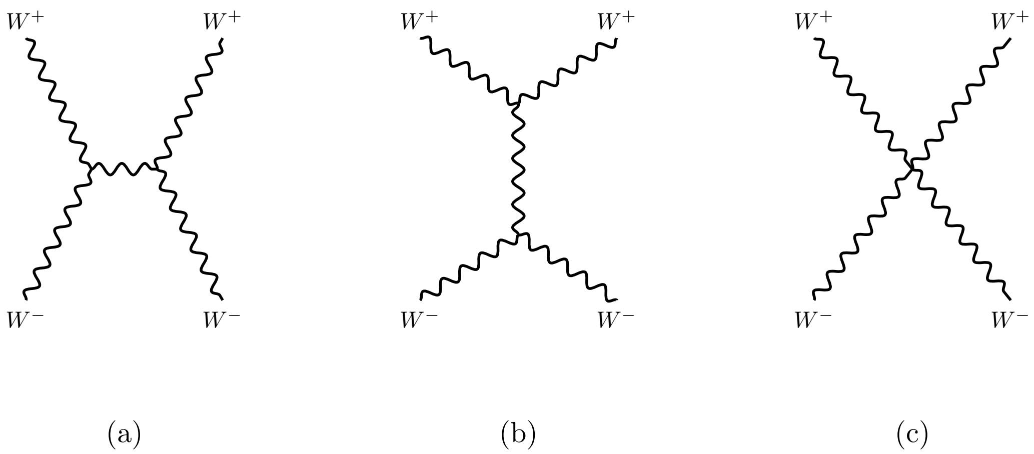

Figure 2.2: The tree-level (a) s-channel, (b) t-channel, and (c) quartic W scattering processes involving only the W-boson

W-scattering cross-section

One of the key motivations for including a scalar boson in models of new physics comes from the WW scattering cross-section, $\sigma(\mathrm{WW} \to \mathrm{WW})$.

The tree-level contributions for this process arising from processes involving only the W-boson are shown in Figure 2.2. Considering only these diagrams, the total amplitude can be shown to be[82],

$$\Sigma \mathcal{M}_{\mathrm{WW}} = \frac{g^2 P^2}{2m^2}(1 + \cos\theta) + \mathcal{O}\big(P^0\big), \tag{2.55}$$

where P is the three-momentum and $P >> m$, θ is the angle between the initial and final state W^+ particles, and $\mathcal{M}_{\mathrm{WW}}$ is the matrix element for this process.

If these are the only diagrams contributing to the WW scattering process it is clear that equation (2.55) diverges as $P \to \infty$ and unitarity is violated.

It is possible to reconcile this and recover unitarity by introducing a new mediator for the process and so additional diagrams are included in the calculation. By including a complex scalar doublet the original diagrams are preserved while two new diagrams are introduced with a scalar propagator ϕ and a coupling $m\phi W^{+}{}_{\mu}W^{-\mu}$. These diagrams are shown in Figure 2.3.

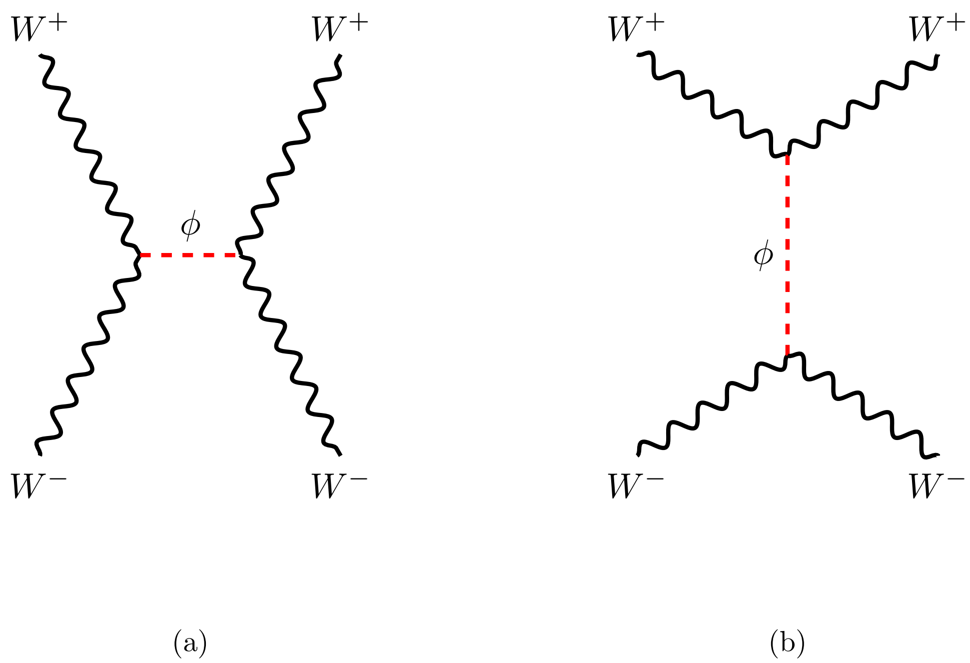

Figure 2.3: The tree-level (a) s-channel and (b) t-channel W scattering processes involving a scalar propagator ϕ

These diagrams contribute to the amplitude as[82],

$$\mathcal{M}_{2s} = \frac{g^2 P^2}{2m^2}(1 - \cos\theta) + \mathcal{O}\big(P^0\big) \tag{2.56}$$

$$\mathcal{M}_{2t} = -\frac{g^2 P^2}{2m^2} + \mathcal{O}\big(P^0\big), \tag{2.57}$$

such that these scalar-mediated diagrams' amplitude cancel the divergence of those in Figure 2.2 and hence unitarity is recovered.

By use of the Higgs mechanism to provide masses to the particles, as in Section 2.1.6, a complex scalar doublet is indeed introduced into our model and hence the addition of the

Higgs to the SM provides a solution for preserving unitarity in W W scattering.

Divergence of the Higgs mass and the hierarchy problem

In introducing the Higgs doublet and thereby providing mass terms for the SM particles and fixing unitarity for the W W-scattering process, unfortunately a further problem is also introduced.

In calculating the mass term for the Higgs particle the loop contributions, see Figure 2.4, quadratically diverge.

For a Dirac fermion ψ the Higgs coupling is described by the term $-\lambda_f H\bar{\psi}\psi$, where λ_f is the Yukawa coupling for the particle, and hence the loop correction to m_H^2 coming from the diagram in Figure 2.4a is[90],

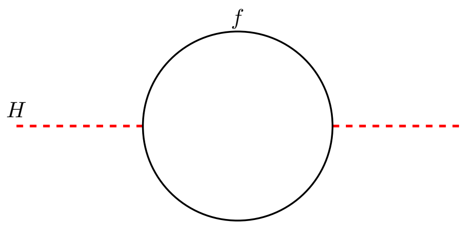

(a)

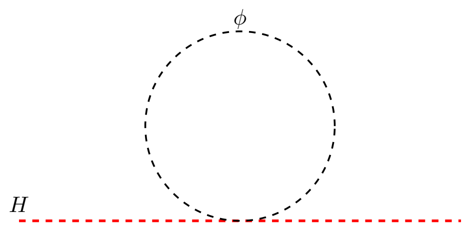

(b)

Figure 2.4: One-loop corrections to the Higgs mass parameter $m^2_{\mathrm{h}^0}$ arising from (a) fermion and (b) scalar particles

$$\Delta m_h^2 = -\frac{|\lambda_f|^2}{8\pi^2}\Lambda_{\mathrm{UV}}^2 + \ldots \tag{2.58}$$

where Λ_{UV} is called the ultra-violet cut off and is equal to or greater than the energy at which the SM can be considered valid. While any of the fermions of the SM can be substituted in here the Yukawa couplings λ_f are proportional to mass and as such the contributions will be dominated by the top quark for which $\lambda_f \simeq 1$. If the SM is considered a valid description of all particle physics up to the Planck scale, M_P these corrections, and hence the Higgs mass, explode. Since all of the quarks, leptons, and massive gauge bosons in the SM have mass terms involving H, e.g. equation eqs. (2.48) and (2.53), all of them become sensitive to the cut off Λ_{UV}. This means that there must exist some scale below M_P where physics beyond the SM becomes apparent. Not only this, but however that new regime is described, it must regulate the loop integral as well as include new propagators for the loops and not reintroduce instabilities (as there will exist Δm_h terms similar to equation (2.58) for the virtual contributions from any arbitrarily massive particles that couple to the Higgs).

Even in a theory where any new particles do not couple to the Higgs, if they share gauge interactions with the Higgs field they will create corrections to the Higgs mass. This means that contributions to Δm_h^2 are sensitive to both the heaviest particles that share gauge interactions with the SM and the ultraviolet cutoff of the theory. In this system one would therefore expect the natural mass of the Higgs to be $m_h^2 \sim M_P^2$[90]. To realize an electroweak scale Higgs mass[2] and hence reconcile theory with the experimentally favored regions for m_h a theory must, ideally, create a systematic cancellation between the various contributions.

Dark Matter

Current gravitational measurements[113] of the content of the universe provide significant evidence for the existence of matter, and energy, which emit little to no electromagnetic radiation and make up the majority of our universe's mass-energy.

This content is generally broken down into two categories: dark energy, which is beyond the scope of this document, and Dark Matter (DM).

The vast majority of DM is thought to be non-baryonic, interact extremely weakly with the electromagnetic force, and be travelling relatively slowly with respect to the speed of light[56]. This is largely due to the lack of direct observation of dark matter. If DM were highly energetic or eletromagnetically charged then observation would likely follow.

[2]This is related to what is know as the hierarchy problem; that if the Higgs mass is to be of the electroweak scale we either require exceptionally fine tuned cancellations between the radiative correction and the bare mass, or that these corrections naturally cancel within the theory of BSM physics

Hence this type of matter is termed Cold DM (CDM). Searches[56] currently report measure of the CDM content to be

$$\Omega_{\mathrm{CDM}} h^2 = 1.1120 \pm 0.0057 \tag{2.59}$$

where Ω is the matter density parameter defined as $\frac{\rho_{\mathrm{CDM}}}{\rho_{\mathrm{crit}}}$ and ρ_{crit} is the critical density of the Universe, and $h = \frac{H_0}{100km/s/Mpc}$ where H_0 is Hubble's constant.

The SM provides no particle(s) which can possibly fulfill the role of CDM. Though neutrinos are massive and weakly charged, they travel at ultrarelativistic velocities and hence are candidates for what is termed Hot DM (HDM). HDM alone cannot account for early galactic formation[30] and as such CDM is still required.

Anomalous magnetic moment of the muon

In Section 2.1.2 the magnetic moment of the electron was presented as motivation for the development of QED as well as a precision test of the SM. In a similar fashion, the anomalous magnetic moment of the muon acts as a precision test of the SM and shows a discrepancy between the predicted and observed values.

The anomalous magnetic moment of the muon is defined as

$$a_\mu = \frac{g_\mu - 2}{2} \tag{2.60}$$

and the SM diagrams contributing to this are shown in Figure 2.5.

The SM prediction for a_μ disagrees with the experimental value[26] by approximately 3.4σ

The naturalness problem

The naturalness problem is concerned with the relative scales of the various inputs into the SM.

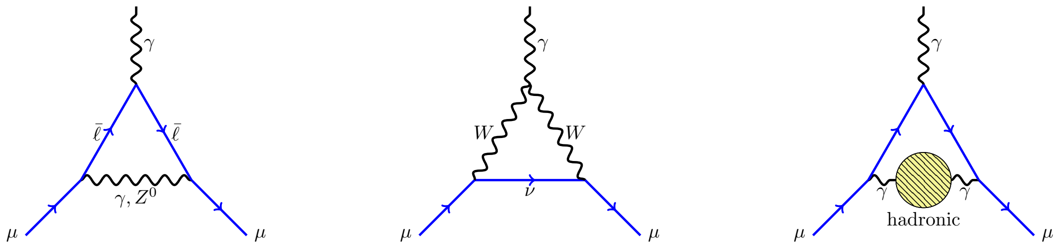

(a) (b) (c)

Figure 2.5: Example SM diagrams contributing to the anomalous magnetic moment of the muon for (a) QED, (b), weak, and (c) hadronic processes

In a natural theory all terms that preserve the symmetries of the action of the system have *natural* coefficients[79], defined as having the form[110]

$$C = c\Lambda^{4-d} \tag{2.61}$$

where Λ is, again, the cutoff scale of the theory, d is the dimensionality of the quantum mechanical operator, and c is a number with $c \lesssim 1$. Further, naturalness requires that the dependence of c on the energy scale Q must be proportional at most to $\log Q/\Lambda$[79].

In the SM both the coefficient of the Higgs mass term, see Section 2.1.7, and the phase θ of the Lagrangian terms leading to CP violation in the strong force seem to be unnaturally small and in the case of the former have a quadratic dependence on the energy scale, see equation (2.58).

2.2 Supersymmetry

While the SM, along with extensions to incorporate neutrino masses, provides a precise and accurate description of physics at the electroweak scale sections 2.1.7 to 2.1.7 indicate that there are obviously physical phenomena that the SM does not predict, or predicts inaccurately. Not only this, but attempts to calculate the Higgs mass in the SM, Section 2.1.7, suggests that there must be new physics at some scale between the

(s)particles	spin
$[u, d, c, s, t, b]_{L,R}\ [e, \mu, \tau]_{L,R}\ [\nu_{e,\mu,\tau}]_L$	$\frac{1}{2}$
$[\widetilde{\mathrm{u}}, d, c, s, t, b]_{L,R}\ [e, \mu, \tau]_{L,R}\ [\nu_{e,\mu,\tau}]_L$	0
$g(\mathrm{W}^{\pm}, H^{\pm})\ (\gamma, H_1^0, H_2^0)$	1/0
$\tilde{g}\tilde{\chi}_{1,2}^{\pm}\ \tilde{\chi}_{1,2,3,4}^{0}$	$\frac{1}{2}$

Table 2.2: The particle content of a supersymmetric theorys

electroweak and the Planck scale.

Supersymmetry is a symmetry proposed in addition to those incorporated in the SM in an attempt to resolve these issues. This symmetry relates fermions and bosons and ultimately leads to the prediction of a new generation of partner particles to those of the SM, called sparticles originating from the defining transformation:

$$\hat{Q}\,|\mathrm{Boson}\rangle = |\mathrm{Fermion}\rangle \tag{2.62}$$

where $\hat{Q}$ is the supersymmetric operator. A table of these particle is given in Table 2.2

Hence, the mutliplets (doublets and singlets) of the SM are replaced with supermultiplets each containing both fermionic and bosonic states that are partners of each other under the symmetry, where each member of the fermion-boson supermultiplet are a combination of the supersymmetric operators $\hat{Q}$ and $\hat{Q}^{\dagger}$.

In unbroken theories of SUSY, i.e. where the symmetry is exact, the sparticles are identical to their SM partners in all quantum numbers other than differing by half-integer spin, and as such have the same mass. In these theories the quadratic divergences in the Higgs mass squared, equation (2.58), are cancelled *exactly* by the existence of the new couplings.

If SUSY were unbroken then sparticles would have been detected in many previous searches for instance [12, 13], due to their low masses. This requires that if sparticles do exist, they must arise from a model of *broken* SUSY. That is, there is a scale between the universal scale and the electroweak scale at which the new symmetry is broken.

Broken models of SUSY allow the masses of the sparticles to differ significantly from those of their SM partners, and hence allow these sparticles to have escaped detection therefore reconciling the existence of SUSY with observation.

The Higgs boson, if it is to be included in such a theory, must reside within one of the supermultiplets, and to avoid a gauge anomaly[90] it is necessary to have at least *two* of these Higgs supermultiplets such that their weak hypercharge values, $Y = \pm 1/2$, cancel each other out. This existence of two Higgs supermultiplets leads the prediction of five physical higgses denoted $h^0, H^0, A^0, H^{\pm}$ where h^0 is the SM-like Higgs.

2.2.1 Supersymmetry and solving the problems facing the Standard Model

If the addition of an extra symmetry to the SM is to be justified it must resolve the outstanding issues with the SM. We have already seen, in the previous section, that the fermion-boson symmetry resolves the issues with the correction to the Higgs mass if the symmetry is exact. The hierarchy problem, though not solved, is reduced to the little hierarchy problem[90]. What remains is a for a mechanism for SUSY to produce Dark Matter and resolve the theoretical-experimental discrepancy of the anomalous magnetic moment of the muon.

$(g-2)_\mu$ in Supersymmetry

The superpartner particles present in SUSY contribute to $(g-2)_\mu$ through diagrams similar to those shown in Figure 2.6. The specific contributions are dependent on the mass of the sparticles involved, and so will be dependent on the parameter values of the supersymmetric terms in the Lagrangian. Therefore, since SUSY does not explicitly fix the value of $(g-2)_\mu$, the experimental value becomes useful in constraining the possible values of the parameters of SUSY.

Dark Matter in Supersymmetry

As discussed in Section 2.1.7, DM is required to interact extremely weakly with the electromagnetic force, and be stable. If one imposes a condition on models of SUSY

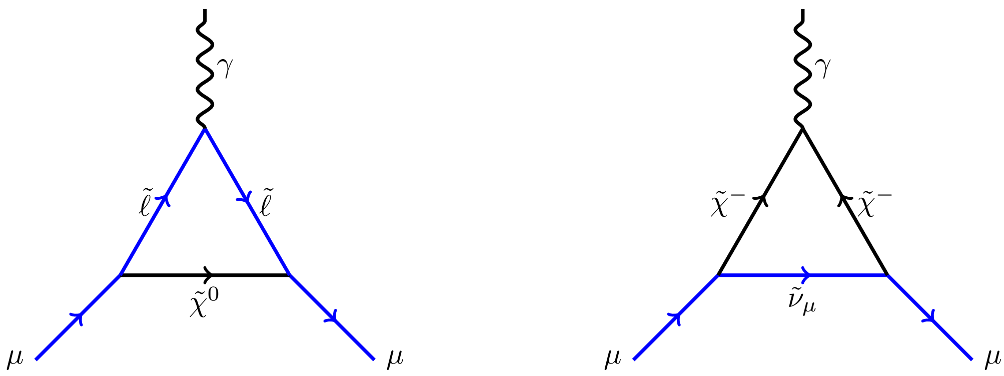

(a) Neutralino and slepton (b) Chargino and sneutrino

Figure 2.6: One-loop Supersymmetry diagrams contributing to the anomalous magnetic moment of the muon

that the Lightest Supersymmetric Particle (LSP) cannot decay to two SM particles, then it must by definition be stable. If this particle is also electromagnetically neutral then, assuming it also satisfies the cosmological constraints, it is a candidate particle for DM.

2.2.2 Softly broken Supersymmetry

In Section 2.2 it was noted that SUSY must be a broken symmetry. If broken models of SUSY are to accurately represent nature then the symmetry may not be arbitrarily broken, but must be only *softly* broken. That is, the process of breaking the symmetry must not lead to a reappearance of ultraviolet divergences in the theory[53], e.g. similar to the issues described in Section 2.1.7.

The effect of insisting on softly-broken supersymmetry is that supersymmetry must be *explicitly* broken. Terms are introduced to the supersymmetric Lagrangian that break the symmetry, where it is assumed these terms originate in some unknown sector where SUSY is broken spontaneously[53] (i.e. all the terms in the Lagrangian respect the symmetry).

2.2.3 R-Parity

Part of the impact of SUSY is that lepton number and baryon number are no longer explicitly conserved. However, since the conservation of these has been experimentally tested to a high precision, any theory of SUSY must not lead to a violation of the conservation rules incompatible with experimental data. To this end a new symmetry, called R-Parity, is imposed on the SUSY fields that forbids such couplings. R-Parity is defined by the multiplicatively conserved quantity,

$$P_r = (-1)^{2s+3B+L} \tag{2.63}$$

where s, B and L denote spin, baryon number, and lepton number respectively. This means that for the SM particles $P_r = 1$, whereas SUSY particles have $P_r = -1$. Therefore the LSP, in R-Parity respecting models, is stable as once the decay chain reaches the LSP, which is still heavier than any SM particle, it is impossible for this particle to decay to two SM particles and still conserve R-Parity.

Alongside reconciling R-Parity conserving models of SUSY with observation, R-Parity leads to models having a natural candidate particle for dark matter in the form of the now stable LSP if this is the neutralino $\widetilde{\chi}_1^0$, meeting the criteria discussed in Section 2.1.7.

2.3 Minimal Supersymmetry

The Minimal Supersymmetric Standard Model (MSSM) is the minimal extension to the SM that describes a supersymmetric model. This model is both softly broken and includes R-Parity conservation[3].

[3] Extensions of the MSSM allow for varying degrees of R-Parity violation[90] however the terms that cause this are excluded in the MSSM

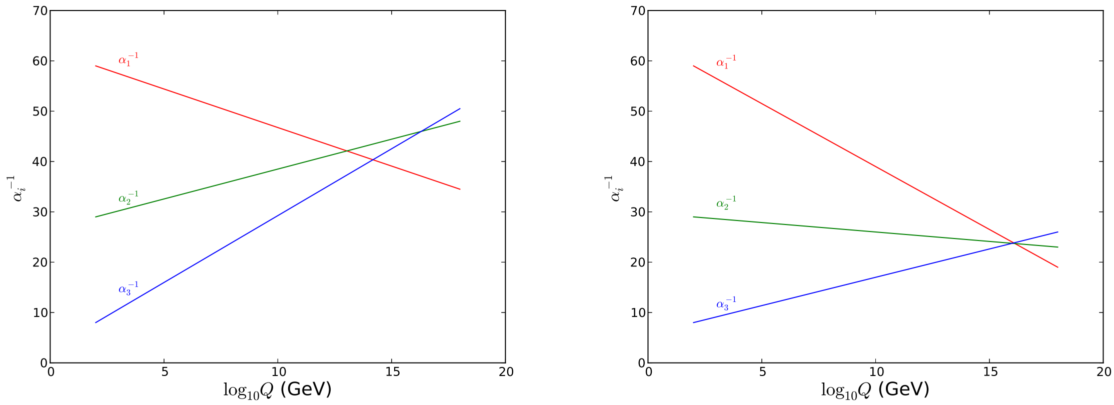

(a) (b)

Figure 2.7: Gauge couplings as a function of the energy scale Q in the (a) SM and (b) MSSM

2.3.1 Gauge unification in the Minimal Supersymmetric Standard Model

The behavior of a coupling constant g varies with the energy scale Q according to its respective beta function[115] defined as,

$$\beta(g) = \frac{\partial g}{\partial \log Q} \tag{2.64}$$

where the implicit dependence of $\beta(g)$ on the scale Q is contained within the evolution of g with Q. The calculation of the β functions in the SM do not converge at any scale, however when calculated in the MSSM assuming TeV scale superpartners, they converge at a scale $Q \sim 10^{16}$GeV[52]. This can be seen in in Figure 2.7. The unification of the gauge couplings in the MSSM has been one of the motivations for both the MSSM and low-mass SUSY in general.

2.4 Models of Supersymmetry

Though the MSSM was constructed to solve many of the problems facing the SM, the parameter space and breadth of phenomenological behavior contained within are diverse and hence non-trivial to analyse. The minimum number of parameters needed to define a point in the parameter space of the MSSM is $\sim$ 100[90]. Hence it is necessary to apply constraints to the MSSM in order to reduce the parameter space and make specific predictions of the phenomenology.

2.4.1 Constrained Minimal Supersymmetric Standard Model

By imposing the unification of some of the parameters of the MSSM at the Grand Unified Theory (GUT) scale (m_{GUT}) the number of input parameters is immediately reduced and all other parameters can be calculated at the electroweak scale by solving the Renormalization Group Equations (RGEs)[91].

Hence at m_{GUT} the following relationships are imposed,

$$\begin{aligned}
A_t = A_b = A_\tau &\equiv A_0, \\
m_{H_1}^2 = m_{H_2}^2 = m_L^2 = m_R^2 &\equiv m_0^2, \\
m_Q^2 = m_U^2 = m_D^2 &\equiv m_0^2, \\
M_1 = M_2 = M_3 &\equiv m_{1/2}.
\end{aligned}$$

Here A_i denotes the trilinear coupling of i, $m_{H_{1,2}}$ are the masses associated with each of the Higgs doublets, $m_{L,R}$ are the masses of the leptonic multiplets, $m_{Q,U,D}$ are the masses of quark multiplets and $M_{1,2,3}$ are the masses of the gauginos corresponding to $U(1)$, $SU(2)$, and $SU(3)$ respectively.

This reduces the number of free parameters of the model to five, m_0, $m_{1/2}$, A_0, sign(μ) (the sign of the Higgs mixing parameter), and $\tan\beta$ (the ratio of the Higgs vacuum expectation values). This defines the Constrained Minimal Supersymmetric Standard Model (cMSSM).

It is important to note that, by insisting on a CDM candidate the relationship between the mass parameters, m_0 and $m_{1/2}$, is restricted. To achieve a possible CDM candidate the LSP must be a neutralino, as such for any value of m_0 that is picked, there is a corresponding maximum value of $m_{1/2}$ (or vice versa) for which the lightest neutralino and the stau have similar mass and beyond which the LSP is no longer a neutralino.

2.4.2 The Very Constrained Minimal Supersymmetric Standard Model and Minimal Super Gravity

One can further constrain the parameter space by enforcing a relationship[59],

$$A_0 = B_0 + m_0, \tag{2.65}$$

where A_0 and B_0 are the unified trilinear and bilinear coupling values respectively, and m_0 is the unified scalar mass. This reduces the number of free parameters to three, namely m_0, $m_{1/2}$, and A_0. $\tan\beta$ is now fixed by the radiative Electroweak Symmetry Breaking (EWSB) conditions[57]. This model is known as the Very Constrained Minimal Supersymmetric Standard Model (vcMSSM)[60].

By making an assumption about the existence of a gravitino $\tilde{G}$ (partner of the graviton), and constraining its mass to be $m_{3/2} = m_0$, we can define a further sub-model termed Minimal Super Gravity (mSUGRA)[59, 61]. mSUGRA shares the same input parameters as the vcMSSM however there is a constraint on the relative values of m_0 and $m_{1/2}$ if the lightest neutralino, $\widetilde{\chi}_1^0$, is to remain the LSP. The mass of the lightest neutralino, $m_{\widetilde{\chi}_1^0}$, can be approximated as $m_{\widetilde{\chi}_1^0} \sim 0.4 \times m_{1/2}$[61]. If we wish to ensure that the gravitino is not the LSP then we require $m_{3/2} > m_{\widetilde{\chi}_1^0}$ or, in terms of m_0 and $m_{1/2}$,

$$m_{1/2} < 2.5 m_0 \tag{2.66}$$

2.4.3 Non-Universal Higgs Models

Rather than imposing more constraints, we can relax the unification rules of the cMSSM for the Higgs sectors. Assuming that all other relationships are kept, we can then define two other models: Non-Universal Higgs Model (NUHM) 1 and NUHM 2[58].

In the NUHM 1 the Higgs doublet masses are both equal, but are *not* required to be equal to the unified scalar mass m_0 , such that we gain an input parameter $m_{H_{1,2}}$.

In the NUHM 2 the Higgs doublet masses are not required to be equal to m_0 nor each other, therefore we gain two input parameter m_{H_1} and m_{H_2} .

Due to this extra freedom present in NUHMs the strict relationship between m_0 and $m_{1/2}$ to maintain a neutralino CDM candidate is modified. In both NUHM1 and NUHM2 the masses of the neutralinos depend on the degrees of non-universality and so it is possible to go to lower values of $m_{1/2}$ (for a particular m_0) and still maintain a neutralino LSP. Also this extra degree of freedom allows for a wider range of the mass-scale parameter space to provide reasonable relic dark matter abundance. By tuning the non-universality parameter it is possible to maintain rapid annihilation funnels to the LSP by maintaining $m_X \sim 2 \times m_{\tilde{\chi}_1^0}$.

Specifically, this arises because one can choose to use as the extra two independent parameters $m_A^2(Q)$ and $\mu(m_Z)$ where $Q \equiv \left(m_{\tilde{t}_R} m_{\tilde{t}_L}\right)^{1/2}$. These relate back to $m_{H_{1,2}}$ through the electroweak symmetry breaking conditions[58] giving

$$m_A^2(Q) = m_{H_1}^2(Q) + m_{H_1}^2(Q) + 2\mu^2(Q) + \Delta_A(Q) \tag{2.67}$$

$$\mu^2 = \frac{m_{H_1}^2 - m_{H_2}^2 \tan^2\beta + \frac{1}{2} m_Z^2 (1 - \tan^2\beta) + \Delta_\mu^{(1)}}{\tan^2\beta - 1 + \Delta_\mu^{(2)}} \tag{2.68}$$

where Δ_X are loop corrections. Hence by moving through the parameter space of $m_{H_{1,2}}$ for fixed m_0 ,$m_{1/2}$ it is possible to find inputs where $m_A \sim 2 \times m_{\tilde{\chi}_1^0}$.

Chapter 3

The Large Hadron Collider and the Compact Muon Solenoid detector

3.1 The Large Hadron Collider

The LHC[63, 31] is a two-ring circular synchrotron with a circumference of 26.7 km located on the Franco-Suisse border, in the tunnel originally used to house the Large Electron Positron Collider (LEP) collider[94]. It is designed to collide beams of protons resulting in proton-proton collisions with a maximum center of mass energy $\sqrt{s} = 14\text{TeV}$ and with a luminosity $\mathcal{L} \sim 10^{34}$ particles $cm^{-2}s^{-2}$.

The LHC is a discovery machine for which the main design objectives were the discovery of the Higgs particle as well as detection of BSM physics, e.g. particles originating from supersymmetric models or the measurement of branching ratios inconsistent with the SM. In both of these cases for these effects and particles to have evaded detection the processes must have small cross-sections and/or involve particles with high masses, hence the LHC's high center of mass energy and design luminosity; Figure 3.1 shows the production cross-section as a function of center of mass energy for a selection of processes.

As well as searching for new physics the aims include the study of known phenomena and to allow precise determination of effects already included in the SM, such as CP

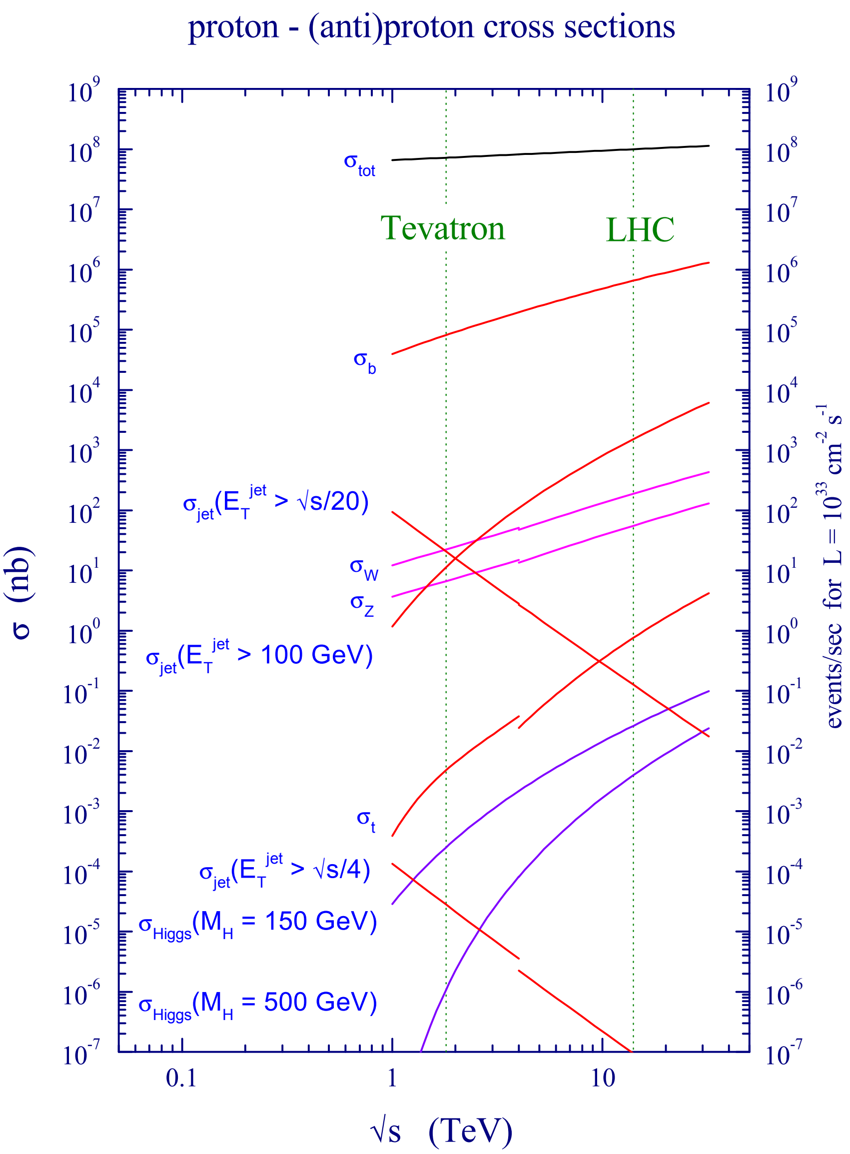

Figure 3.1: The production cross-section by process as a function of center of mass energy[39], with $p\bar{p}$ lines to the left ($\sqrt{s} < 4$TeV) and pp lines to the right ($\sqrt{s} > 4$TeV)

Violation (CPV).

The collider uses two counter-rotating beams of protons, arranged in bunches that are roughly cylindrical in shape, orbiting the LHC and producing a collision rate of approximately 40MHz.

3.1.1 Beams at the Large Hadron Collider

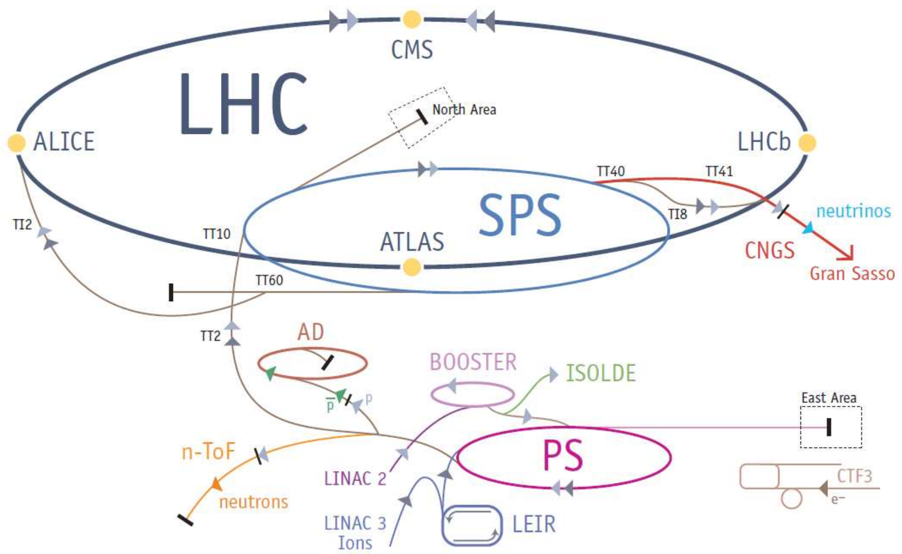

Figure 3.2: A schematic of the LHC accelerator complex[87]

The protons that the beam consists of begin their life at the LHC as a hydrogen gas which is then ionized to produce free protons. These protons are then fed into the linear accelerator, LINAC2. Here they are accelerated up to energies of 50MeV per proton and subsequently injected into the Proton Synchrotron Booster (PSB) where they are further accelerated up to 1.4GeV. The Proton Synchrotron (PS) and Super Proton Synchrotron (SPS) are the next stages where the protons are accelerated to energies of 25GeV and 450GeV respectively. Once these stages are complete the protons are transferred into the LHC and accelerated up to the running center of mass energy, either 3.5TeV(2011) or 4.0TeV(2012). The components of this accelerating process are shown in Figure 3.2.

Once at the designated center of mass energy, the beams are deflected at the interaction points around the ring of the LHC. At each of these interaction points sits a detector. There are four main experiments present at the LHC; Large Hadron Collider Beauty (LHCb)[2] which deals with precision b-physics interactions, A Large Ion Collider Experiment (ALICE)[117] which is used for the study of heavy ion physics, and two general purpose detectors designed to study TeV scale physics, A Toroidal LHC Apparatus (ATLAS)[46] and Compact Muon Solenoid (CMS)[120].

3.1.2 Center of mass energy

While the maximum design center of mass energy of the LHC is $\sqrt{s} = 14$TeV the decision was made, following an incident in 2009, to begin data-taking runs with a center of mass energy of $\sqrt{s} = 7$TeV starting in March 2010. This was subsequently increased to $\sqrt{s} = 8$TeV in March 2012. These high energy and luminosity environments require carefully designed detectors.

3.1.3 Detecting Supersymmetry

The decays of supersymmetric particles, such as squarks and gluinos, in R-parity conserving models of SUSY result in cascades always containing a stable LSP. As discussed in Section 2.2.3 the LSP interacts very weakly, and hence passes through detectors without interacting. For an SM-like event one expects the vector sum of the transverse components of momentum (p_{T}) of the final state particles to be balanced, i.e. zero, within the precision of the detector if all particles are measured accurately. However in an event where one or more particles escape the detector without measurement there should be a degree of imbalance in the transverse plane characterized by the Missing Transverse Energy ($E_{\mathrm{T}}^{\mathrm{miss}}$) term. To achieve good resolution of the $E_{\mathrm{T}}^{\mathrm{miss}}$ it is necessary to have a high degree of hermeticity and absorption for all particles involved in the events.

The remaining parts of these supersymmetric cascades result in many leptons and jets (b-quark and τ jets in particular) as well as hard isolated[1] photons for instance, from

[1] An object is isolated when the energy associated with the object is above a object type-dependant fraction of the total energy within a cone surrounding the object.

Gauge Mediated Symmetry Breaking (GMSB) like models of SUSY).

As well as the signal processes it is necessary to have good understanding and control of the SM process that produce the background to the signal. These originate mainly from QCD and Electroweak (EWK) processes and are specific to the particular analysis being undertaken (see Section 4.6 for examples).

3.2 Compact Muon Solenoid

The CMS detector[120] is one of the two general purpose detectors situated at the LHC. It is comprised of, from outermost to innermost component, four muon chambers interleaved with iron return yokes, an outer Hadronic Calorimeter (HCAL), a $3.8T$ superconducting electromagnet, a sampling brass-plastic HCAL, an active lead tungstate Electromagnetic Calorimeter (ECAL), a silicon strip tracker, and a pixel tracker.

Over the two year running period 2011-2012 operating at both 7TeV and 8TeV center of mass energy CMS has recorded a total of 5.55fb^{-1} and 21.79fb^{-1} respectively; see Figure 3.3 for the cumulative luminosity for the two operating periods.

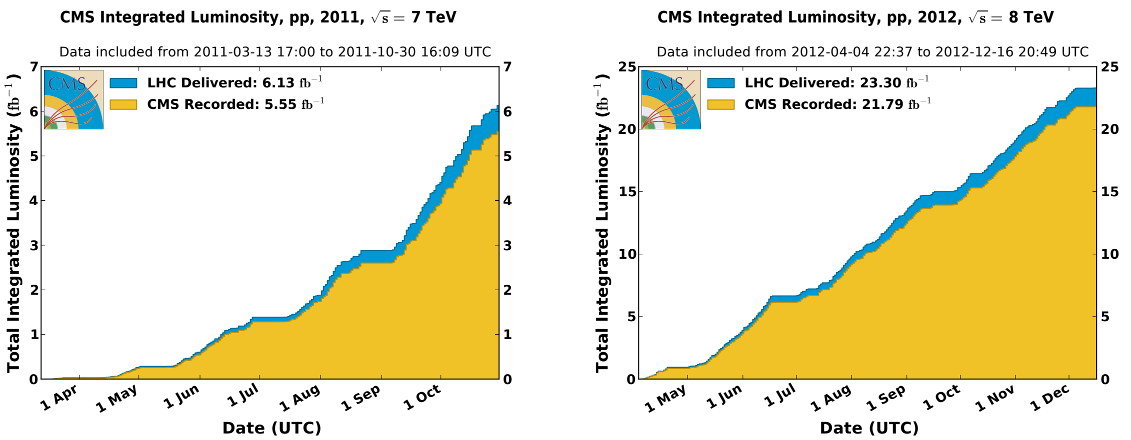

Figure 3.3: Cumulative luminosity over time for 2011 (7TeV, left) and 2012 (8TeV, right), showing both the total delivered by the LHC and the total recorded by the CMS detector.

3.2.1 Coordinates

Many features and design requirements of the CMS detector are given with respect to a specific coordinate system, detailed below:

- z-axis: points along the beam pipe
- y-axis: points vertically upward
- x-axis: points towards the center of the LHC ring with the origin being at the interaction point of the two beams
- ϕ (Azimuthal angle): extends from the x-axis in the $x - y$ plane
- θ (Polar angle): extends from the z-axis and is expressed in terms of the Lorentz invariant quantity pseudo-rapidity defined as

$$\eta = -\log\left[\tan\frac{\theta}{2}\right] \tag{3.1}$$

3.2.2 Design Requirements

The design requirements laid out at the point of design [120] were:

- Strong muon identification and momentum resolution over a large range of momenta in the region $|\eta| < 2.5$, and a mass resolution of a dimuon system of 1% at 100GeV/c^2 and unambiguous determination of the charge of muons with momentum less than 1TeV.
- Good momentum resolution and reconstruction efficiency for charged particles; efficient triggering and offline identification of b-quark and τ jets.
- High resolution for electromagnetic energy, di-photon and di-electron mass resolutions of similar order to those required of the di-muon systems. Wide geometric coverage $|\eta| < 2.5$ and measurement of the direction of photons as well as the correct localizations of the primary interaction vertex.

The most relevant for the searches laid out here is the requirement of good $E_{\mathrm{T}}^{\mathrm{miss}}$ and di-jet mass resolution, requiring high hermeticity over the range $|\eta| < 5$ and fine lateral segmentation in the detector components ($\Delta\eta \times \Delta\phi < 0.1 \times 0.1$).

3.3 Components of CMS

To meet the design requirements there are multiple special purpose sub-detectors that comprise CMS as laid out in Section 3.2 and shown in Figure 3.4

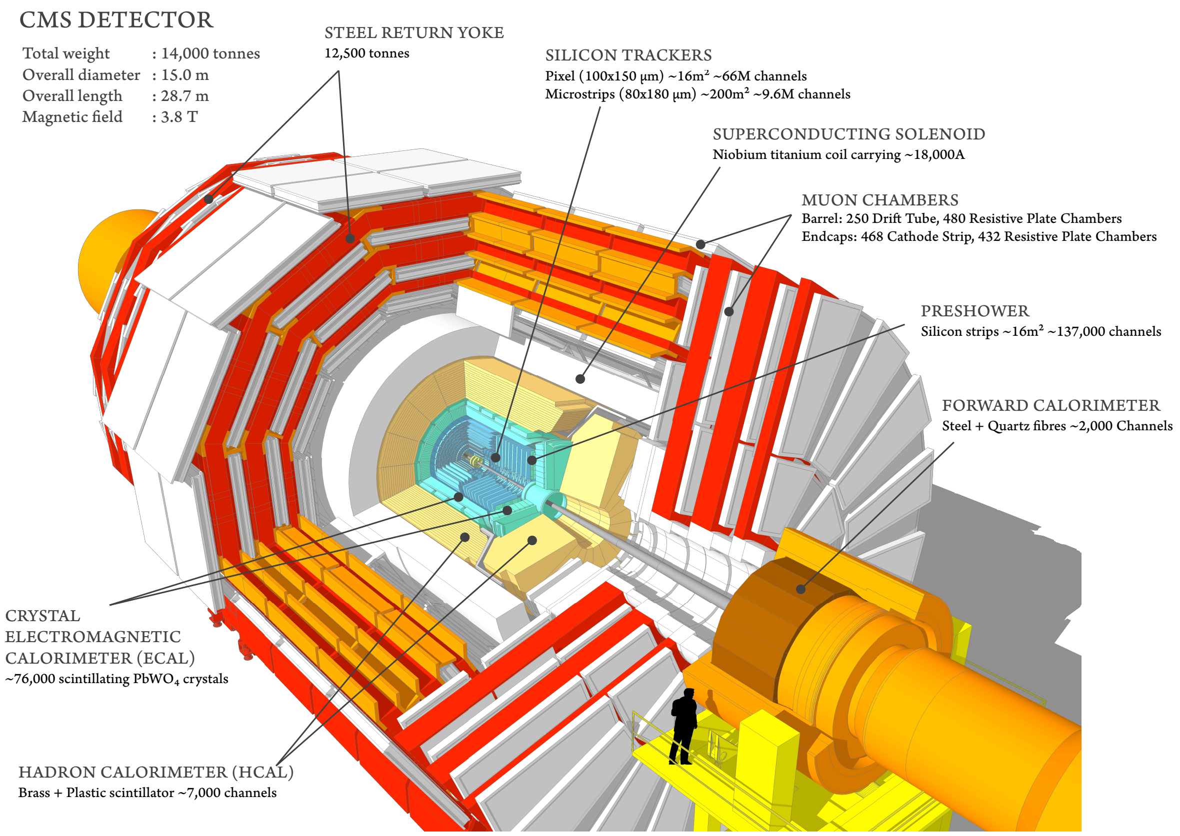

Figure 3.4: Cutaway view of the CMS detector[104]

3.3.1 Muon chambers

Muons do not interact via the strong force, and are too massive for Bremsstrahlung to have a significant effect[2], hence their energy is lost via ionisation. Muons are detected via three types of gaseous chambers that comprise part the muon system, chosen to cover the different radiation environments in which they operate.

Drift Tube (DT) chambers cover the region $|\eta| < 1.2$, where the muon and background rates are low. In the high background low muon rate region ($0.8 < |\eta| < 2.4$) Cathode Strip Chambers (CSCs) are used. Overlapping both of these regions are the Resistive Plate Chambers (RPCs), deployed in the $|\eta| < 1.6$ range[3].

These three sections are used complementarily for triggering and reconstruction. The best performance is achieved when the data from these is combined with other systems that identify or measure muons e.g. those described in Section 3.3.5.

3.3.2 Superconducting magnet

Inside the muon chambers sits a large superconducting solenoid[120]. The bending effect of a solenoid begins at the primary vertex, i.e. the centre of the magnet. Superconducting magnets provide a large bending power to size ratio[122].

The size and structure of this magnet are essential to the structure and layout of CMS. The magnet must be large enough to contain the calorimetry and provides the structural base for the outer systems.

The bending power of the magnet is determined by the performance requirements of the muon systems e.g. the unambiguous determination of sign and a resolution of $\frac{\Delta p}{p} \simeq 10\%$ for momenta of $\sim$ 1TeV. The relationship of the length and radius of the magnet is also tuned to provide good momentum resolution in the forward regions.

The conductor lining the magnet carries a current of $20kA$ through an overall cross-section of $64 \times 22\text{mm}^2$. The solenoid consists of five modules, each wrapped with four lengths of conductor.

[2]For acceleration perpendicular to the direction of motion the power radiated as a result of Bremsstrahlung goes as $P \sim m^{-4}$

Parameter	Value
Field	3.8T
Inner Bore	5.9m
Length	12.9m
Number of Turns	2168
Current	19.5kA
Stored energy	2.6GJ
Hoop stress	64atm

Table 3.1: Parameters of the CMS magnet[120]

3.3.3 Hadronic Calorimeter

The majority of the hadronic calorimetry, and all the non-hadronic calorimetry in CMS, is located inside the magnet coil[121]. There is a layer of scintillators outside the magnet that make up the hadron outer (HO) detector and are part of the HCAL system. The HO scintillators are arranged to match the ϕ segmentation of the muon system's DT chambers and this helps to minimize punch-through from penetrating particles into the muon systems.

The HCAL found inside the magnet coil is broken down into three sections, the hadron barrel (HB), the hadron endcap (HE), and the hadron forward (HF)

Hadron barrel

The HB covers the region $|\eta| < 1.4$ with a segmentation of $\Delta\eta \times \Delta\phi = 0.087 \times 0.087$.

Using a 100GeVtest beam the resolution was determined to be[120]

$$\frac{\sigma(E)}{E} = \frac{94.3\%}{\sqrt{E}} \oplus 8.4\% \tag{3.2}$$

This is compared to the design resolution of $\frac{\sigma(E)}{E} = \frac{100\%}{\sqrt{E}} \oplus 4.5\%$.

Hadron endcap

Each of the two HEs covers the region $1.3 < |\eta| < 3.0$ with a similar segmentation in η to the HB for the outermost towers (low η), but a higher segmentation ($0.09 < \Delta\eta < 0.34$) at higher values of η. These are constructed of brass, again for high absorption and non-magnetic properties, reinforced with stainless steel back plates and are approximately 10 absorption lengths thick.

Hadron forward

The HF calorimeter provides coverage of the range $3.0 < |\eta| < 5.0$. Its main purposes are to aid in identification and reconstruction of very forward jets (hence its position) and improve the overall coverage of the HCAL system thereby improving measurements of $E_{\mathrm{T}}^{\mathrm{miss}}$.

The HF is constructed as a block of copper with quartz fibers embedded within which run parallel to the beam axis. Because of its location it is subject to very high particle fluences; incident particles will create showers that lead to high neutron flux in the calorimeter. However the quartz fibers are able to be used as charge collectors via the Cherenkov effect, as being neutral neutrons will not contribute to this. This allows the HF to function in the very high radiation environment to which it is subjected.

Combined

Each of these components act together to maximise the geometric hermeticity of the hadronic calorimetry, as well as bring the total depth to 11 radiation lengths (including the HO). These two design features maximise the absorption of particles from hadronic showers enabling a high resolution for $E_{\mathrm{T}}^{\mathrm{miss}}$ measurements which are, as discussed, essential to direct searches for the presence of SUSY.

3.3.4 Electromagnetic Calorimeter

The ECAL[119] is designed to measure the energy of electrons and photons which lose energy via electromagnetic processes, e.g. Bremsstrahlung in the case of the electron. The CMS ECAL covers a region of $|\eta| < 3$ for which it has higher precision in the region $|\eta| < 2.5$.

The ECAL is constructed from more than 75000 lead tungstate crystals. This material scintillates when particles deposit energy. These scintillation photons are then collected and amplified by photo diodes (PDs). Within the CMS ECAL there are two types of PDs: silicon avalanche photodiode which are located in the barrel, and vacuum phototriodes located in the endcaps. The latter have a lower gain, but a higher radiation hardness.

Lead tungstate is selected as, along with being radiation hard, it has a short radiation length ($\sim 0.9cm$) and its Molierè radius is low ($\sim 2.1cm$) leading to a high degree of absorption. Each crystal is approximately 26 radiation lengths long transversely[3] meaning that on average all the energy from incident electrons can be absorbed and 90% of the shower arising from a photon can be contained within a single crystal.

With the same test system as used to determine the resolution of the HCAL, see equation (3.2), the energy resolution of the ECAL was determined to be[120],

$$\frac{\sigma(E)}{E} = \frac{2.8\%}{\sqrt{E}} \oplus \frac{124\text{MeV}}{E} \oplus 0.26\% \tag{3.3}$$

which, notably, is better than the design resolution of $\frac{\sigma(E)}{E} < 0.6\%$ at 100GeV.

3.3.5 Tracker

The aim of the CMS tacker[83] is to determine the trajectories and momenta charged particles. In particular, the bending effect of the magnet, and the fact that the tracker resides within it, enables the measurement of particle momenta.

[3]The dimensions are $22 \times 22 \times 230mm$

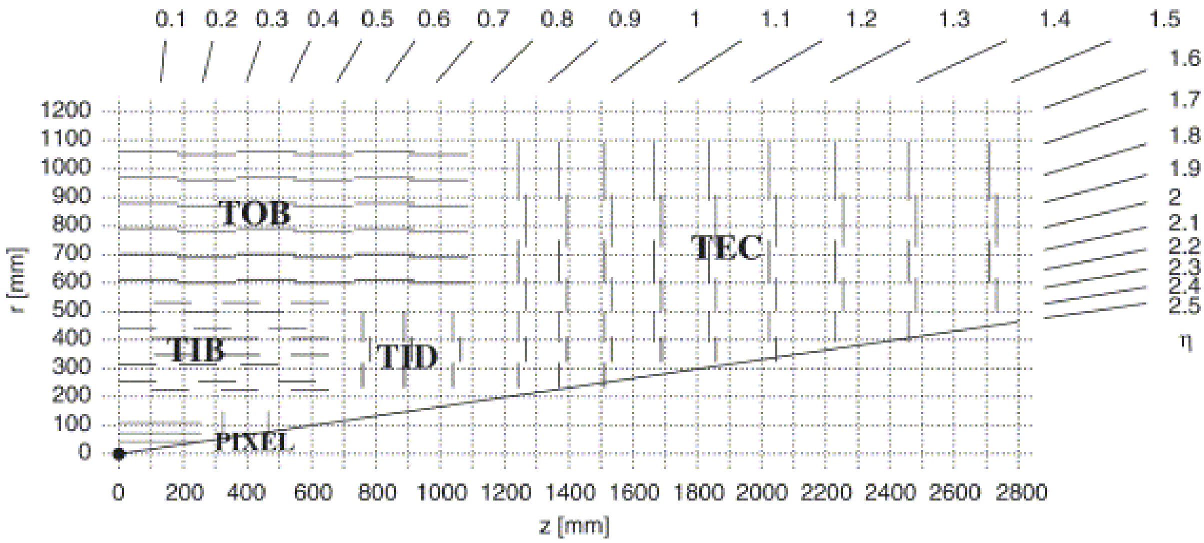

Figure 3.5: Projection of a section of the CMS tracker in rz showing the regions of coverage in η. Lighter segments are single sided, darker segments are double sided[120].

The CMS tracker is split into two main parts, an inner pixel detector which is closest to the beam pipe, and an outer strip tracker which is itself split into several parts. Between these two the tracker covers a region of $|\eta| < 2.5$.

Both sections of the tracker are constructed from silicon, which release charge as particles pass through them. This charge can be collected, enabling high precision reconstruction of praticle tracjectories.

Pixel Detector

The silicon pixel detector is the component of the CMS detector that is closest to the beam pipe, occupying the space between $4.3-10.2cm$, and as such experiences the highest particle fluences of any of the detector subsystems.

The resolution of the pixel detector is $\sim 10\mu m$ in $r\phi$ and $15 - 20\mu m$ in z and there are approximately 45×10^6 readout channels used to enable the pixel detector to seed particle track reconstruction.

Strip Detector

The silicon strip tracker is comprised of several parts, the tracker inner barrel (TIB), the tracker outer barrel (TOB), the tracker inner disks (TID), and the tracker outer endcaps (TEC).

The TIB occupies the space $|z| < 65cm$. The first two layers provide measurements in both $r\phi$ and rz planes, with resolutions of $23 - 34\mu m$ and $230\mu m$ respectively.

The TIB extends out from the pixel detectors up to $|z| < 110cm$. In this region it is possible to use thicker silicon strip due to lower radiation levels

Thicker silicon strips can be used here than in the TIB as the radiation levels are lower. These provide resolutions of $35-42\mu m$ in the $r\phi$ plane and $530\mu m$ in the z direction.

Chapter 4

Exploring models of Supersymmetry with the α_T variable

As detailed in Section 3.1.3, in models of R-parity conserving SUSY, supersymmetric particles are pair produced and decay to the LSP which, in many models, is a Weakly Interactive Massive Particle (WIMP). These models of SUSY, when combined with the initial proton-proton (*pp*) interactions, result in production of coloured sparticles which decay producing event signatures consisting of jets and significant Missing Transverse Energy ($E_{\mathrm{T}}^{\mathrm{miss}}$).

The high energy *pp* collisions at the LHC result in a significant proportion of multi-jet events originating from QCD. Given that the signal events characteristic of the presence of SUSY-like physics are also multijet events it is essential to be able to discriminate between the signal multijet events with an LSP that escapes the detector, and the background multijet events caused by SM QCD. To this end, there are two possible approaches. Either developing an accurate model of the behavior of the significant QCD events in the analysis's signal region, or choosing a signal discriminant which rejects the vast majority of these QCD events.

Though most models of R-Parity preserving SUSY naturally give rise to events with significant $E_{\mathrm{T}}^{\mathrm{miss}}$ further consideration can be given to the details of the other properties and content of events originating from SUSY signal models.

As discussed in Section 2.1.7, to prevent quadratically divergent corrections to the Higgs mass one hopes for a low energy ($\sim$ TeV scale) realisation of SUSY. The driving terms in the corrections to the Higgs mass come from the mass of the superpartner to the top, as well as the top quark Yukawa coupling. The magnitude of the corrections increases with increasing stop mass, hence to avoid large diveregences one requires a sufficiently light stop, e.g. not significantly heavier than the top[126]. Also, given the recent discovery of a Higgs-boson candidate[41, 5] at $m_{\mathrm{h}^0} \sim 125$GeV this further motivates the presence of light third generation squarks due to the low mass window of the result.

The existence of these low mass third generation squarks would result in events with final states that are rich in jets originating from a bottom quark.

4.1 Events with $E_{\mathrm{T}}^{\mathrm{miss}}$: The α_T variable

Given the exceptional complexity and difficulty involved in accurately modelling QCD events, in the analysis presented here we make use of the α_T variable[101] to efficiently reject multijet events without genuine $E_{\mathrm{T}}^{\mathrm{miss}}$.

For the purpose of the analysis presented here the transverse energy, E_{T}, is defined as the scalar sum of the transverse projections of the calorimetry energy deposits. $E_{\mathrm{T}}^{\mathrm{miss}}$ is the vector which balances the vectorial sum of these transverse projections.

sum of the magnitude of the calorimetry read outs projected in the transverse plane, and the $E_{\mathrm{T}}^{\mathrm{miss}}$ is defined as the vector which balances the vectorial sum of the E_{T} values.

The QCD multijet background is characterized mostly by low total $E_{\mathrm{T}}^{\mathrm{miss}}$. Large $E_{\mathrm{T}}^{\mathrm{miss}}$ values exist largely due to statistically small fluctuations, and detector mismeasurement effects.

The kinematic variable α_T can be defined which selects high $E_{\mathrm{T}}^{\mathrm{miss}}$ events and selects against mismeasured events, for instance when mutliple jets from the event fall below some energetic threshold imposed for selection.

In a dijet system α_T is defined as

$$\alpha_T = \frac{E_{\mathrm{T}}^{j_2}}{M_T} \tag{4.1}$$

where j_2 denotes the jet with the lowest E_{T} and M_T is the transverse mass of the dijet system defined as

$$M_T^2 = \left(\sum E_{\mathrm{T}}^{j_i}\right)^2 - \left(\sum P_x^{j_i}\right)^2 - \left(\sum P_y^{j_i}\right)^2 \tag{4.2}$$

where the sums are carried out over N_{jet}, which in this case is two.

For an event where the jets are back to back in ϕ but one jet is mismeasured, so the event is unbalanced, $\alpha_T < 0.5$; when there is no mismeasurement in the back to back case $\alpha_T = 0.5$; for di-jet systems that are not back to back, and hence have the two jets recoiling against genuine $E_{\mathrm{T}}^{\mathrm{miss}}$, $\alpha_T > 0.5$.

The definition of α_T can be extended beyond the dijet case. Where when $N_{\mathrm{jet}} > 2$ the jets are clustered into two pseudo-jets where the E_{T} of the pseudo-jet is the scalar sum of the jets clustered to form it.

Defining the total visible transverse energy associated with all jets as

$$H_{\mathrm{T}} = \sum_j E_{\mathrm{T}}^j, \tag{4.3}$$

i.e. the scalar sum of the transverse energy of jets enumerated by j. The two pseudo-jets are formed of jet combinations such that they minimize the difference in total jet E_{T} between the two systems (ΔH_{T}). This provides the maximum separation between multi-jet background events and events with genuine $E_{\mathrm{T}}^{\mathrm{miss}}$.

For the case of $N_{\mathrm{jet}} \geq 3$ α_T is defined as

$$\begin{aligned}\alpha_T =& \frac{1}{2}\frac{H_{\mathrm{T}} - \Delta H_{\mathrm{T}}}{\sqrt{H_{\mathrm{T}}^2 - {H_{\mathrm{T}}^{\mathrm{miss}}}^2}} \\ =& \frac{1}{2}\frac{1 - (\Delta H_{\mathrm{T}}/H_{\mathrm{T}})}{\sqrt{1 - (H_{\mathrm{T}}^{\mathrm{miss}}/H_{\mathrm{T}})^2}} \end{aligned} \tag{4.4}$$

$$\tag{4.5}$$

Extremely rare fluctuations in the measurments from the calorimetry can lead to values of $\alpha_T \gtrsim 0.5$. Such events can be removed by raising the cut on α_T to require $\alpha_T > 0.55$. An example distribution of the number of events as a function of α_T is shown in Figure 4.1, where the rapid drop off of QCD multijet events at $\alpha_T \geq 0.55$ is clear.

Rather than using the total missing transverse energy, we can define a quantity to characterize the missing momentum in the transverse plane,

$$H_{\mathrm{T}}^{\mathrm{miss}} = \left| \sum_{i=0}^{N_{\mathrm{jet}}} \vec{p_{\mathrm{T}}} \right| \tag{4.6}$$

the absolute value of the vector sum of the jets' Transverse Momentum (p_{T}) where N_{jet} is the number of jets that are considered in the event. By only considering the jet component of an event (i.e. the part of the event measured in the HCAL) the $H_{\mathrm{T}}^{\mathrm{miss}}$ acts as an estimator for the total $E_{\mathrm{T}}^{\mathrm{miss}}$ of the event. This provides a tool to deal with the case where multiple jets fall below the minimum energy required and so fake a $H_{\mathrm{T}}^{\mathrm{miss}}$ signal. This can be accounted for by comparing the $H_{\mathrm{T}}^{\mathrm{miss}}$ to the *total* $E_{\mathrm{T}}^{\mathrm{miss}}$ which is measured across all calorimetry systems and has no miminum energy requirement imposed. A significant discrepancy would suggest that it was likely the event contained multiple jets that were missed.

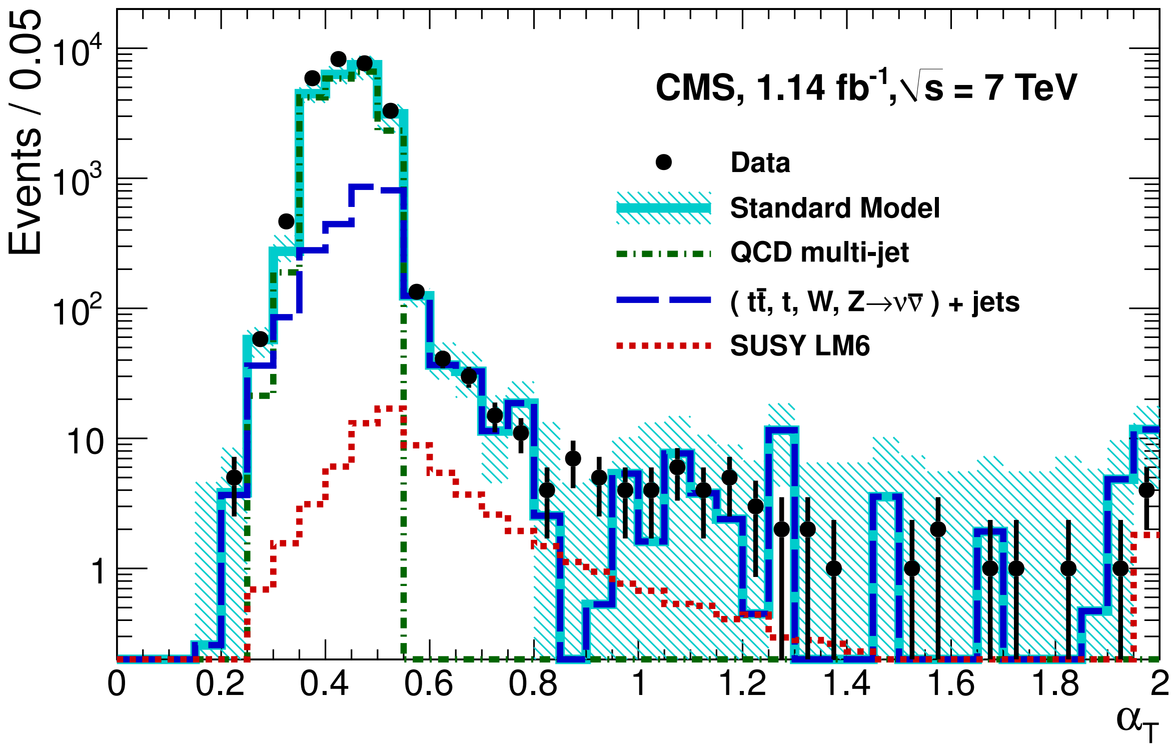

Figure 4.1: Distribution of events with α_T. An $H_{\mathrm{T}}^{\mathrm{miss}}$ cut has been applied to the SM MC to more accurately reflect the data which has an implicit H_{T} cut due to triggering

4.2 Events with jets originating from a b-quark

A jet that originates from a bottom quark is identified through a secondary vertex displaced with respect to the primary interaction vertex. The Combined Secondary Vertex algorith with Medium working point (CSVM)[27] attempts to distinguish between jets originating from bottom quarks and jets originating from other sources (e.g. light flavour quark jets). The CSV algorithm provides a discriminator variable for which this analysis selects the medium working point value > 0.679 which leads to a quark miss-tag rate of 1% for $p_{\mathrm{T}}^{\mathrm{jet}} = 80\mathrm{GeV}$ and b-tagging efficiency of between 60 and 70% which is $p_{\mathrm{T}}^{\mathrm{jet}}$ dependent.

H_{T} range (GeV)	Trigger efficiency (%)
275–325	$83.3^{+0.5}_{-0.6}$
325–375	$95.9^{+0.7}_{-0.9}$
375–475	$98.5^{+0.5}_{-0.9}$
475–∞	$100.0^{+0.0}_{-4.8}$

Table 4.1: Efficiencies of the offline α_T triggers used in the 7TeV α_T analysis on 5fb^{-1}of LHC data, relative to the `Mu_HT` triggers

4.3 Triggers

The efficiency of a trigger is defined with respect to some inclusive sample. It is the fraction of the number of events remaining in the signal region after the trigger is applied.

This analysis uses a specialised joint α_T-H_{T} trigger[92], `HT_AlphaT`, which is designed to have high analysis efficiency and low rate.

For an event with n-jets, each with $E_{\mathrm{T}}^{\mathrm{jet}} > 40$GeV, where the jets are ordered by p_{T}, the trigger algorithm forms the two pseudo jets from the k highest p_{T} jets where $k \in [2, n]$. If for some value of k the event passes the H_{T}-α_T requirements then the event is accepted. If $k = n$ is reached and the event has failed for all values of k then the event is rejected. If however there are more than 15 jets with $E_{\mathrm{T}}^{\mathrm{jet}} > 40$GeV the event is accepted regardless.

The thresholds for the trigger are $H_{\mathrm{T}} > 250$GeV and $\alpha_T > 0.53$ where the threshold on α_T was increased to $\alpha_T > 0.6$ towards the end of the 2011 run.

The efficiency for this trigger, with respect to the `Mu_HT` trigger, is given in Table 4.1.

4.4 Event selection

Due to the large and varied background composition it is necessary to define strict cuts and vetoes while still selecting for a variety of SUSY all hadronic topologies.

For the purpose of this analysis a jet is defined to be a collection of clustered particles[1] reconstructed from energy deposits in the calorimetry towers. The energy of the jets are corrected to produce a uniform response in pseudo-rapidity η (to account for the different depths in radiation lengths the particles travel through before reaching the calorimeter towers). The energy of the jets is also corrected to take account of pile-up effects; here the `L1Offset` [44] jet energy corrections are applied. The jets are also calibrated for absolute response in p_{T}.

A jet energy threshold is imposed, requiring $E_{\mathrm{T}}^{\mathrm{jet}} > 50\mathrm{GeV}$. The jet with the highest E_{T} in the event is required to be in the region $|\eta| < 2.5$, i.e. in the central tracker acceptance region, so that it is well measured in the tracker and likely highly boosted. The two highest E_{T} jets are further required to have $E_{\mathrm{T}}^{\mathrm{jet}} > 100\mathrm{GeV}$ as this ensures a sufficiently small background level for $\mathrm{Z} \rightarrow \nu\overline{\nu} + \mathrm{jets}$ which is a source of genuine $E_{\mathrm{T}}^{\mathrm{miss}}$ in the SM (see Section 4.6.1).

A suppression of SM processes with $E_{\mathrm{T}}^{\mathrm{miss}}$ caused by neutrinos escaping the detector can be achieved by vetoing events with isolated electrons or muons which have $p_{\mathrm{T}} > 10\mathrm{GeV}$; note that this *does not* reduce the sources outlined in Section 4.6.2 as they deal with a hadronically decaying τ, detector effects, or where this cut veto is not relevant.

A further veto is applied if any jet passing the jet E_{T} threshold falls in $|\eta| > 3$ as a way of preserving the $H_{\mathrm{T}}^{\mathrm{miss}}$ resolution as jets ouside of this range are not inclued in the $H_{\mathrm{T}}^{\mathrm{miss}}$ calculation (this region roughly represents the change between the HB and HF sections of the HCAL).

Isolated photons which have $p_{\mathrm{T}} > 25\mathrm{GeV}$ are vetoed to reduce the ensure that we are considering events arising solely from multijet topologies.

Finally significant hadronic activity is required for an event to be considered, defined as the event satisfying $H_{\mathrm{T}} > 275\mathrm{GeV}$.

[1] specifically clustered using the anti-k-t algorithm[38] with with a distance parameter of $R = 0.5$

4.4.1 Hadronic control sample

An independent data set is formed by inverting the requirement on α_T (i.e. $\alpha_T < 0.55$), leading to a data set rich in QCD multijet events. This is used in the modelling of any remaining background originating from QCD that may enter the signal region. The process of this modelling is described in Section 4.11.2.

4.5 Signal Region

As discussed in Section 4.4 and Section 4.1 respectively, we define the region of interest to have $H_\mathrm{T} > 275$, and $\alpha_T > 0.55$. The H_T requirement is chosen to be as low as reasonably possible to allow for inclusion of softer jets. The signal is then separated into eight bins in H_T, in GeV: 275-325, 325-375, 375-875 in steps of 100, and > 875GeV. This binning allows for cross-correlations and determination of shape information, and hence improved sensitivity to higher H_T events.

The jet energy threshold is lowered in the first two bins of H_T (to 36.7 and 43.3GeV for the lowest and second lowest bins respectively). This maintains a higher event H_T to jet energy threshold ratio, and maintains event jet multiplicities.

The signal region is further separated into bins of the number of jets identified as originating from a bottom quark, n_b. These bins are $n_b = 0, 1, 2$ and $n_b \geq 3$. By doing this we improve the sensitivity to a variety of signal models. For instance, the highest b-tag multiplicity bins have exceptionally low SM rates, and as such by binning in this fashion it is possible to easily identify high b-tag multiplicity signal events (e.g. from light-stop signal models).

As well as being binned, the signal region has several cleaning filters applied to reduce the effects of the pre-selection requirements and detector effects in generating background. These are detailed in Section 4.5.1 and 4.5.2

The acceptance for an identified object is defined as the set of kinematic requirements for the object to be included in the signal or control region

4.5.1 Dead ECAL cut

There exist some regions of the ECAL where there are either dead or mis-reporting read-outs. These regions have been masked. Alongside these there is the gap between the barrel and the endcap regions of the detector at $|\eta| = 1.5$; this region is also masked.

The vectorial $\vec{H}_{\mathrm{T}}^{\mathrm{miss}}$ is used to identify jets most likely to be associated with the $H_{\mathrm{T}}^{\mathrm{miss}}$ by selecting the jet closest in ϕ to the resulting total $\vec{H}_{\mathrm{T}}^{\mathrm{miss}}$ when that jet is subtracted from the event. The separation in ϕ from $\vec{H}_{\mathrm{T}}^{\mathrm{miss}}$ is denoted $\Delta\phi^*$.

Any event with minimum $\Delta\phi^* < 0.5$ rejected if the distance in (η, ϕ) between the jet and the nearest masked ECAL region meets $\Delta R_{\mathrm{ECAL}} < 0.3$ or if the jet lies in the surrounding $\Delta\eta < 0.3$ region of the barrel-endcap. This effectively vetos events where the possible cause of significant $H_{\mathrm{T}}^{\mathrm{miss}}$ in an event is from a jet which has been measured in a problematic area of the detector.

4.5.2 $H_{\mathbf{T}}^{\mathbf{miss}}/E_{\mathbf{T}}^{\mathbf{miss}}$ cut

The $H_{\mathrm{T}}^{\mathrm{miss}}$ calculated from the jets passing our selection criteria is compared to the $E_{\mathrm{T}}^{\mathrm{miss}}$ measured in the calorimeters, i.e. $E_{\mathrm{T}}^{\mathrm{miss}}$ coming from all objects detected after vetoes have been applied. A ratio is defined and required to be $R_{\mathrm{miss}} = H_{\mathrm{T}}^{\mathrm{miss}}/E_{\mathrm{T}}^{\mathrm{miss}^{\mathrm{calo}}} < 1.25$ else the event is rejected. This reduces the contamination of events where there are multiple jets under the jet energy threshold which lead to a fake $H_{\mathrm{T}}^{\mathrm{miss}}$ signal, where because the $E_{\mathrm{T}}^{\mathrm{miss}}$ calculation imposes no such jet energy threshold the value of R increases.

4.6 Sources of background

The SM production of $\mathrm{t\bar{t}}$, $\mathrm{W} \to \ell\nu$ and $\mathrm{Z} \to \nu\bar{\nu}$ can all produce significant missing energy signals which form part of the background to this search.

4.6.1 Z $\rightarrow \nu\overline{\nu}$

Events with a Z produced with high p_{T} along with jets, where the Z decays to a neutrino anti-neutrino pair can form a genuine SM $E_{\mathrm{T}}^{\mathrm{miss}}$ signal.

Notably the kinematics of Z $\rightarrow \nu\overline{\nu}$ events and $\gamma +$jets are expected to be similar in cases where the photon has $p_{\mathrm{T}} > m_{\mathrm{Z}^0}$. This is discussed in further detail in Section 4.8.1. The rate of this process falls with rising E_{T} [49].

4.6.2 W $\rightarrow \ell\nu$

In a similar fashion to Z $\rightarrow \nu\overline{\nu}$ events, events with a high p_{T} W that decays to a neutrino and a lepton form a background to the search. Three mechanism make up the majority of the background originating from W $\rightarrow \ell\nu$;

- A lepton (e^- or μ^-) can fail the requirements used to identify this process (isolation, for example) or can fail to be reconstructed
- A lepton (τ) can decay hadronically
- A lepton (e^- or μ^-) can fall outside our defined detector acceptance range or otherwise not be included (e.g. if its p_{T} is under the minimum p_{T} required)

4.6.3 $\mathrm{t\overline{t}}$

Direct pair production of top quarks decaying semi-leptonically can produce a significant background to $E_{\mathrm{T}}^{\mathrm{miss}}$ analyses. This occurs when the the pair decay through t $\rightarrow$ bW decays, and the W decays as W $\rightarrow \ell\nu$ for one of the top-pair and hadronically for the other. This contributes significantly to the background as the single lepton can be missed, and hence one of the entire W decays is missed.

4.7 Background composition

In the case of dijet events, the largest contribution comes from W $\rightarrow \ell\nu$ (Section 4.6.2) and Z $\rightarrow \nu\overline{\nu}$ (Section 4.6.1). For higher jet multiplicities one also has to consider $\mathrm{t\bar{t}}$ (Section 4.6.3) production that results in a semileptonic weak top quark decay.

All composition percentages below are given as inclusive values summed over b-tag multiplicities, and originate from an MC study of the signal region[109].

Though the rate of Z $\rightarrow \nu\overline{\nu}$ falls with rising E_{T}, the proportion of the background in the signal region rises with H_{T}; for the lowest H_{T} bin it forms 43% of the total background, rising to 53% for the highest inclusive H_{T} bin. Because this is a genuine source of $E_{\mathrm{T}}^{\mathrm{miss}}$ in the SM, it forms part of the irreducible background.

Another significant contribution comes from associated production of W or Z decaying to electrons or muons where the veto fails to exclude the event. These contribute between 25% to 13% of the background, from low to high H_{T}.

Hadronically decaying τ leptons form 22% to 27% of the background from low to high H_{T}. Leptonically decaying τ leptons, which are also missed by the leptonic vetoes, account for 10% of the background.

In the b-tag dimension, n_b, for low b-tag multiplicities the dominant contribution comes from both W + jets and Z + jets, and with increasing multiplicity begins to be dominated by $\mathrm{t\bar{t}}$ decays.

4.8 Background estimation from data control samples

Within the defined signal region for this analysis the QCD multi-jet events are expected to give negligible contributions.

On top of the major backgrounds described in Section 4.6, contributions are also expected from Drell-Yan, single top and di-boson production.

To accurately estimate the contributions of these and the other sources of background, three control samples are selected. These are data control samples chosen to be kinematically similar to the processes they are modelling and binned identically such that subtle effects that are not modelled in MC can be accounted for.

The $\mathrm{Z} \rightarrow \nu\overline{\nu} + \mathrm{jets}$ contribution is estimated from an SM-enriched combination of $\mu\mu + \mathrm{jets}$ and $\gamma + \mathrm{jets}$ samples where in both samples at least two jets are required and they are binned identically to the signal sample. These are used as they are kinematically similar to $\mathrm{Z} \rightarrow \nu\overline{\nu} + \mathrm{jets}$. The remaining background, formed mainly by $\mathrm{W} + \mathrm{jets}$ and $\mathrm{t\bar{t}}$ is estimated from a single μ+jets sample, where again at least two jets are required.

To make use of these control samples translation factors are used, these are functions of both signal binning variables (H_{T} and n_b) and are calculated independently for each control sample. Hence we have one translation factor per bin per sample.

The expectation of an SM background process in a bin of the signal region (H_{T},n_b) is given by:

$$N_{\mathrm{pred}}^{\mathrm{signal}}(H_{\mathrm{T}}, n_b) = N_{\mathrm{obs}}^{\mathrm{control}}(H_{\mathrm{T}}, n_b) \times \frac{N_{\mathrm{MC}}^{\mathrm{signal}}(H_{\mathrm{T}}, n_b)}{N_{\mathrm{MC}}^{\mathrm{control}}(H_{\mathrm{T}}, n_b)} \tag{4.7}$$

where $N_{\mathrm{obs}}^{\mathrm{control}}(H_{\mathrm{T}}, n_b)$ is the observed yield in a control sample bin, and the fraction is the translation factor defined as the ratio of simulated yields in the signal bin, $N_{\mathrm{MC}}^{\mathrm{signal}}(H_{\mathrm{T}}, n_b)$, to the corresponding bin of the control sample, $N_{\mathrm{MC}}^{\mathrm{control}}(H_{\mathrm{T}}, n_b)$.

This definition means that yields originating in MC are not used directly but only in ratios, where any systematics arising from mismodelling will largely cancel.

When building up the total control MC the following proceesses are considered: W+jets, $\mathrm{t\bar{t}}$+jets, $\mathrm{Z} \rightarrow \nu\overline{\nu} + \mathrm{jets}$, DY+jets, single top + jets and di-bison (WW, WZ, ZZ +jets) denoted N_W, $N_{\mathrm{t\bar{t}}}$, $N_{\mathrm{Z}\rightarrow\nu\overline{\nu}}$, N_{DY}, N_{top} and $N_{\text{di-boson}}$ respectively. These are produced in the following way. The W + jets and $\mathrm{Z} \rightarrow \nu\overline{\nu} + \mathrm{jets}$ are simulated using `MADGRAPH V5` [17] event generator. The $\mathrm{t\bar{t}}$+jets and single-top events are generated using `POWHEG` [66]. The di-boson events are produced with `PYTHIA 6.4` [112]. All parton showering and hadronisation processes are simulated using `PYTHIA 6.4`, and the detector simulation is handled by the `GEANT4` [15] tool. Each set of calculations is normalized the most accurate available cross-section calculations, usually at Next to Leading Order (NLO) accuracy.

The total MC control sample yield is then

$$N_{\mathrm{MC}}^{\mathrm{control}}(H_{\mathrm{T}}, n_b) = N_W + N_{\mathrm{t\bar{t}}} + N_{\mathrm{Z}\to\nu\bar{\nu}} + N_{\mathrm{DY}} + N_{\mathrm{top}} + N_{\text{di-boson}} \tag{4.8}$$

4.8.1 Control Samples

μ + jets

This control sample is used to estimate the background from W + jets and $\mathrm{t\bar{t}}$ processes that are in the hadronic signal sample due to leptons that have failed acceptance, or are not reconstructed, or contain hadronically decaying taus.

In this sample events are selected to find $\mathrm{W} \to \mu\nu$ events. The same cuts on H_{T}, $H_{\mathrm{T}}^{\mathrm{miss}}$ and α_T from the signal region are applied, and the same H_{T} binning is used, but the muon is ignored in all such calculations.

Events are required to have one isolated muon with $p_{\mathrm{T}} > 10\mathrm{GeV}$ and in the region $|\eta| < 2.5$. Multi-jet QCD events are suppressed by requiring $M_T\big(\mu, E_{\mathrm{T}}^{\mathrm{miss}}\big) > 30\mathrm{GeV}$. If the muon falls within $\Delta R(\mu, \mathrm{jet}) < 0.5$ of any jet or if a second muon candidate is detected that fails the same requirements placed on the first muon and the two muon system has an invariant mass in the range $m_Z - 25 < m_{\mu_1\mu_2} < m_Z + 25$[2] then the event is vetoed.

The statistical power of this sample can be increased by removing the α_T requirement, as the kinematic selection criteria mean that there is little QCD contomination in this sample. However, removing the α_T requirements means that the `HT_AlphaT` trigger can no longer be used and instead a `Mu_HT` cross-trigger is used in place. Due to the p_{T} requirement in the muon-leg and the threshold in the H_{T}-leg, this trigger cannot be used in the lowest two H_{T} bins ($H_{\mathrm{T}} < 375\mathrm{GeV}$). For these two bins we make use of the `HT_AlphaT` cross-trigger again, and hence impose the α_T requirement offline.

[2] Suppresses likely $\mathrm{Z} \to \mu\mu$ events

$\mu\mu + \textbf{jets}$

As discussed in Section 4.6.1, $\mathrm{Z} \rightarrow \nu\overline{\nu} + \mathrm{jets}$ forms a significant proportion of the background. However these events have similar kinematic properties to those of $\mathrm{Z} \rightarrow \mu\mu + \mathrm{jets}$ only with a different branching ratio. Since the muons are required to be in our $|\eta|$ acceptance range and for real $\mathrm{Z} \rightarrow \nu\overline{\nu} + \mathrm{jets}$ no such requirement can be made on the neutrinos, a small difference in the kinematic properties of the samples is introduced.

Using the $\mu\mu + \mathrm{jets}$ control sample it is possible to estimate the contribution to the irreducible background coming from $\mathrm{Z} \rightarrow \nu\overline{\nu} + \mathrm{jets}$.

As with the $\mu + \mathrm{jets}$ control sample the two muons are not considered when calculating H_{T}, $H_{\mathrm{T}}^{\mathrm{miss}}$ and α_T; the same cuts and binning are used as in the hadronic signal region, with the same $H_{\mathrm{T}} > 375\mathrm{GeV}$ and $n_b \geq 1$ regions making use of the `Mu_HT` trigger as opposed to the `HT_AlphaT` trigger. The same requirements on p_{T}, $|\eta|$, and ΔR are placed on the muons as in the $\mu + \mathrm{jets}$ sample, however the di-muon system is required to have an invariant mass within $m_Z - 25 < m_{\mu_1\mu_2} < m_Z + 25$ as to select a sample containing Z bosons.

$\gamma + \textbf{jets}$

As well as using the $\mu\mu + \mathrm{jets}$ sample to estimate $\mathrm{Z} \rightarrow \nu\overline{\nu} + \mathrm{jets}$, we can also make use of a $\gamma + \mathrm{jets}$ sample. This is formed of events requiring exactly one tightly isolated photon with $p_{\mathrm{T}} > 150\mathrm{GeV}$[3] and in $|\eta| < 1.45$. If the photon falls within $\Delta R(\gamma, \mathrm{jet}) < 1.0$ the event is vetoed.

Again, when calculating H_{T}, $H_{\mathrm{T}}^{\mathrm{miss}}$, and α_T the photon is discarded, and the same cuts and binning as in the hadronic signal region are used. This control sample is only used in the region $H_{\mathrm{T}} > 375\mathrm{GeV}$ due to the high p_{T} requirement of the trigger for the photon.

[3] This value is selected based on the $H_{\mathrm{T}}^{\mathrm{miss}}$ implied by the α_T cut, which results in $H_{\mathrm{T}}^{\mathrm{miss}}/H_{\mathrm{T}} \approx 0.4$ which when combined with the H_{T} region considered, gives $0.4 \times 375\mathrm{GeV} = 150\mathrm{GeV}$

4.8.2 QCD multijet background

After defining the signal region as $H_{\mathrm{T}} > 275$, $\alpha_T > 0.55$ and applying the pre-selection cleaning filters (i.e. the $H_{\mathrm{T}}^{\mathrm{miss}}/E_{\mathrm{T}}^{\mathrm{miss}}$ and $\Delta\phi^*$ cuts) the QCD multi-jet background is expected to be reduced to negligible levels. However if non-zero, it can be modelled and taken into account in the likelihood calculations.

A variable, R_{α_T}, is defined as the ratio of events above and below the cut value of α_T ($\alpha_T = 0.55$) in each H_{T} bin.

An exponentially decaying form with respect to H_{T} is assumed for R_{α_T}. This can be motivated by the increasing jet energy resolution with increasing H_{T}, the reduction of pathological effects with increasing energy, and finally the narrowing of the α_T distribution in the region $H_{\mathrm{T}} > 375$ due to increasing jet multiplicity. Therefore R_{α_T} is assumed to fit,

$$R_{\alpha_T}(H_{\mathrm{T}}) = A_{n_b} e^{-kH_{\mathrm{T}}} \tag{4.9}$$

Where the decay constant k is assumed to be fixed for all b-tag multiplicities, and the normalization factor A_{n_b} has a per b-tag multiplicity value.

The value of, and error on, k is constrained through the use of side-bands where anti-selections of the different cuts are taken. These side-bands can be seen in Figure 4.2, where the labelled signal region corresponds to $\alpha_T > 0.55, H_{\mathrm{T}}^{\mathrm{miss}}/E_{\mathrm{T}}^{\mathrm{miss}} < 1.25$. Region B corresponds to the side-band obtained by inverting the α_T cut only. Region C is defined by inverting both the α_T and the $H_{\mathrm{T}}^{\mathrm{miss}}/E_{\mathrm{T}}^{\mathrm{miss}}$ cut, i.e. selecting events with $\alpha_T < 0.55$ and $H_{\mathrm{T}}^{\mathrm{miss}}/E_{\mathrm{T}}^{\mathrm{miss}} > 1.25$. Region C is then binned in α_T in steps of 0.1 in the range $0.52 < \alpha_T < 0.55$ and labelled C_1, C_2, C_3 for decreasing values of α_T. This creates a significantly enriched QCD sample, where the binning allows for determination of the behavior of this sample with respect to α_T. By inverting the $H_{\mathrm{T}}^{\mathrm{miss}}/E_{\mathrm{T}}^{\mathrm{miss}}$ cut Region D is obtained, which again is a mutli-jet enriched sample, which is used in a cross-check on the exponential model of R_{α_T}.

The α_T anti-selection, Region B, is used to constrain the central value of k, and the variation between α_T slices in the $H_{\mathrm{T}}^{\mathrm{miss}}/E_{\mathrm{T}}^{\mathrm{miss}}$ anti-selection, Regions $C_{1,2,3}$, is used to

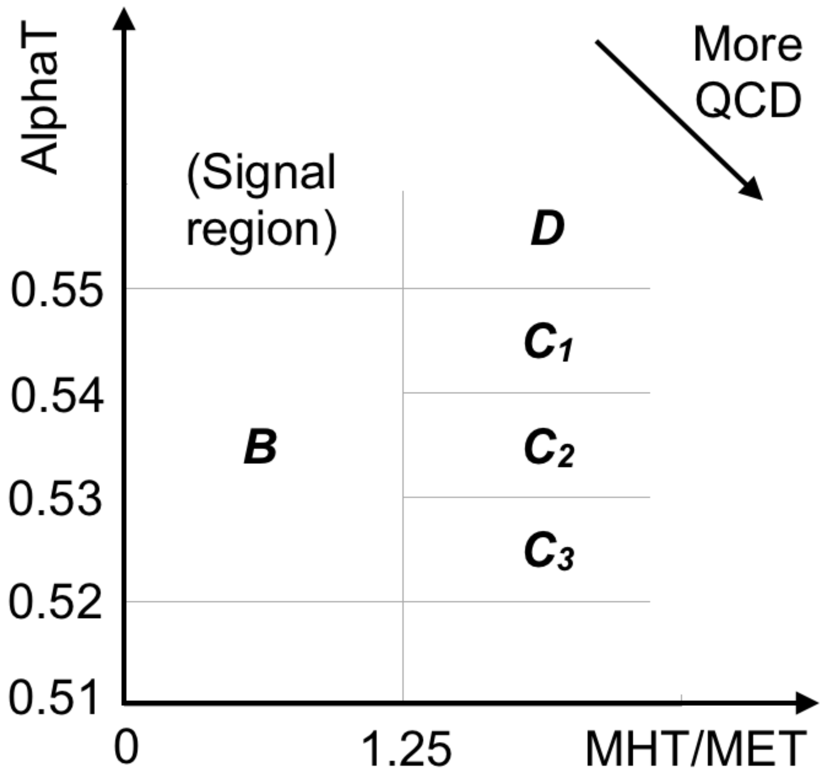

Figure 4.2: Pictorial representation of the QCD side-bands[109]

estimate a systematic uncertainty on k, giving a result of $k = -2.96 \pm 0.61(\text{stat}) \pm 0.46(\text{syst})$ which is used to constrain terms in the likelihood, see Section 4.11.2.

4.9 Improving estimates for high b-jet multiplicity events

As discussed in Section 4.8.1, the μ+jets data sample provides estimates for the dominant $t\bar{t}$ and W + jets production in the SM. In the case of high b-tag multiplicity (i.e. $n_b = 2$, $n_b \geq 3$), the contribution to the background from $Z \to \nu\overline{\nu}$ is negligable. In this region then, the μ + jets sample is used to estimate the $Z \to \nu\overline{\nu}$ sample, as the $\mu\mu$ + jets and γ + jets data samples become increasingly statistically limited with increasing b-tag multiplicity. So for events in the $n_b = 2$ and $n_b \geq 3$ bins the total SM background is estimated using *only* the $\mu + \text{jets}$ sample; in all other bins all three $\mu + \text{jets}$, $\mu\mu + \text{jets}$ and $\gamma + \text{jets}$ samples are used.

4.9.1 Formula method for translation factor prediction

Since only the one data sample is used to estimate the total SM background for high b-tag multiplicities it is necessary to make maximum use of the statistical power of the available simulations.

We can estimate the distribution of b-tag multiplicity by comparing reconstructed and generator level simulations. For each event in the MC sample the generator level jets are looped over and matched to the nearest reconstructed jet within $\Delta R < 0.5$, where $\Delta R = \sqrt{\Delta\eta^2 + \Delta\phi^2}$ and provided that $0.5 < p_{\mathrm{T}}^{gen}/p_{\mathrm{T}}^{reco} < 1.5$. The number of reconstruction level jets that are matched to generator level b, c, and other light flavour quarks are denoted n_b^{gen}, n_c^{gen} and n_q^{gen} respectively. The total number of matched jets per H_{T} bin is $N\left(n_b^{\mathrm{gen}}, n_c^{\mathrm{gen}}, n_q^{\mathrm{gen}}\right)$. MC is also used to determined the b-tagging efficiency and mistag probabilities, ϵ and f_q respectively, for each H_{T} bin. These values are correct with respect to data on a per-jet basis as described in [40]. From these values it is possible to predict the event yield in a given H_{T} bin[43],

$$N(n_b) = \sum_{n_b} \left(N\left(n_b^{\mathrm{gen}}, n_c^{\mathrm{gen}}, n_q^{\mathrm{gen}}\right) \times P_b \times P_c \times P_q \right) \tag{4.10}$$

where $P_x \equiv P(n_x^{\mathrm{tag}}; n_x^{\mathrm{gen}}, f_x)$ and n_x^{tag} is the number of times that a reconstructed b-jet's assocatied generator level jet is of type $x \in \{b, c, q\}$ and $f_b \equiv \epsilon$. P_x are the probabilities for these arrangements to happen. Finally, the sum is performed over all values of possible n_b^{tag}, n_c^{tag} and n_q^{tag} such that $n_b = \sum_{x\in\{b,c,q\}} n_x^{\mathrm{tag}}$

The accurate determination of f_c and f_q is essential as $n_b \geq 3$ is likely to be dominated by events with two real b-jets with a further mis-tagged jet (e.g. $\mathrm{t\bar{t}}$), as genuine three b-jet events are rare in the SM.

4.9.2 Signal scans

Each phenomenological model considered, the cMSSM and the various simplified models, is broken down into individual signal models, representing a single point in the model's parameter space. For each signal model considered 10000 events are generated. These are reconstructed using fast-simulation which requires scale-factor corrections to be brought into line with full-simulation reconstruction, which again needs corrections to be brought into line with data. To accomplish this two-step re-weighting, the scans have point-by-point corrections applied.

Consider an event in which there are two generator level b-jets, and two generator level non-b-jets all matched to reconstruction level jets, but one of each pair is b-tagged. The probability of mis-tagging a non-b-jet, and missing one of the b-jets is[109],

$$\begin{aligned} p = {} & \epsilon\Big(p_{\mathrm{T}}^{\mathrm{jet}^1}, \eta^{\mathrm{jet1}}\Big) \\ & \times \Big(1 - \epsilon\Big(p_{\mathrm{T}}^{\mathrm{jet}^2}, \eta^{\mathrm{jet2}}\Big)\Big) \\ & \times m\Big(p_{\mathrm{T}}^{\mathrm{jet}^3}, \eta^{\mathrm{jet3}}, \mathrm{ID}^{\mathrm{jet3}}\Big) \\ & \times \Big(1 - m\Big(p_{\mathrm{T}}^{\mathrm{jet}^4}, \eta^{\mathrm{jet4}}, \mathrm{ID}^{\mathrm{jet4}}\Big)\Big) \end{aligned} \tag{4.11}$$

where ϵ and η are the b-tagging efficiency and mis-tagging rates, and the lines of the equation correspond to a b-jet that tags correctly, a b-jet that is not b-tagged, a non-bjet that is mis-tagged and a non-b-jet that is not mis-tagged respectively.

For this example event the re-weighting factor, w is given by,

$$w = \frac{SF_b\epsilon \times (1 - SF_b\epsilon) \times SF_{c,\mathrm{light}}m \times (1 - SF_{c,\mathrm{light}}m)}{\epsilon \times (1-\epsilon) \times m \times (1-m)} \tag{4.12}$$

where SF_b is the scale-factor for b-tag efficiency, and $SF_{c,\mathrm{light}}$ are the mis-tagging scale factors for c quarks or other light flavors where the values of these are specific to the b-tagger used in the analysis (CSVM)[118] and are multiplicatively made from the fast-simulation to full-simulation and the full-simulation to data scale factors[109].

4.10 Systematic Uncertainties

While the use of translation factors reduces the effect of systematics from mis-modelling it is important to understand any possible uncertainty on them. The fit used to predict the total background through the yields in the hadronic signal sample and the control samples also makes use of the translation factors. As such, having well motivated systematic uncertainties on the translation factors is essential to the accuracy of the fitting procedure.

Uncertainties on the translation factors can be motivated through the use of closure tests where a control sample is used to mimic signal; that is for a well closed translation factor one would expect

$$R_{\text{closure}} = \frac{N_{\text{obs}} - N_{\text{pred}}}{N_{\text{pred}}} \sim 0 \tag{4.13}$$

where N_{obs} is the observed yield and N_{pred} is the predicted yield. The statistical error from the translation factor, based on the MC sample size, is combined with the error on the number of events in the sample being used as a predictor. This gives the final error on the closure ratio and means that the value of R gives the level of closure of the translation factors as a predictor *per bin*.

The set of closure tests shown here are used to test various aspects of the background modelling and test the MC's modelling of the kinematics. That is that it correctly reproduces the α_T, μ and γ acceptance. It also tests the modelling of the production and decay cross-sections and how they contribute to the total SM background as well as testing the modelling of reconstruction efficiencies.

The closure of the tests that take $\mu +$ jets and the $\mu\mu +$ jets with no α_T requirement to the same selection but with $\alpha_T > 0.55$ show that the MC correctly models the depedence of these events on α_T.

Note that reference is made to closure tests in the form $\mathcal{X} \rightarrow \mathcal{Y}$, where this denotes the $\mathcal{X}$ sample being used to predict the $\mathcal{Y}$ sample.

The $\mu+$jets $\rightarrow \mu\mu+$jets closure tests of the ratio of Z and W cross-section (σ_Z/σ_W) and

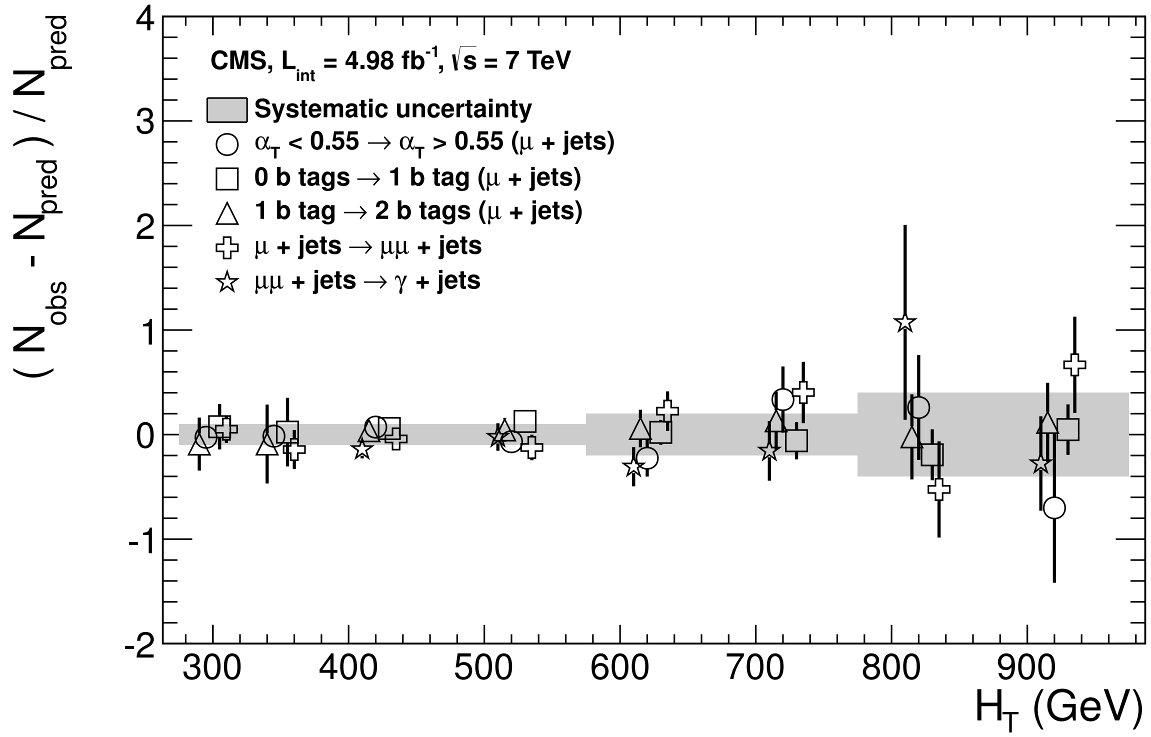

Figure 4.3: A set of closure tests overlaid on top of grey bands representing the systematic uncertainties assigned for use in three H_{T} regions in the simultaneous fit[43].

any effect of the acceptence difference due to selecting muons. The $\mu\mu + \text{jets} \rightarrow \gamma + \text{jets}$ is used to check the ratio of the production cross-sections of $\mathrm{Z} + \text{jets}$ to $\gamma + \text{jets}$, and again any acceptence difference between the photon and the muons.

Dedicated closure tests on the b-tag multiplicity bins is done, where the $\mu + \text{jets}$ sample with $n_b = 0 \rightarrow n_b = 1$, $n_b = 1 \rightarrow n_b > 1$ and finally $n_b = 0 \rightarrow n_b > 1$ where in all three tests the sample being translated to has no α_T requirement. These along side the two closure tests of $\mu + \text{jets} \rightarrow \mu\mu + \text{jets}$ each with $n_b = 0$ and $n_b = 1$ check that the re-weighting method described in Section 4.9.1 is correct, and that it is possible to translate between the different b-tag multiplicity bins.

The results of these closure tests are shown in Figure 4.3.

Figure 4.3 also shows that the H_{T} distribution of the systematic uncertainty associated with the closure tests is split into three regions: $275 < H_{\mathrm{T}} < 575\text{GeV}$, $575 < H_{\mathrm{T}} <$

775GeV, and $H_{\mathrm{T}} > 775$GeV. This splitting is done to decorrelate the systematic uncertainties, and results in a more conservative approach to the values of the systematics. For each region the weighted mean and variance is calculated using each of the values and uncertainties of each closure test contained in the region. Then a systematic is assigned for the translation factors in that region that gives 95% coverage. This conservative choice of systematic uncertainty ensures coverage of any possible small biases in the MC modelling. These uncertainties are assumed to be completely uncorrelated when used in the fit, though one should expect strong correlations between adjacent bins in H_{T}. The results of this method are then rounded up to 10%, 20%, and 40% for each of the respective H_{T} regions.

4.11 Likelihood model

A likelihood model is developed to interpret the signal and control samples. It is broken down into components representing the hadronic sample, electroweak control sample, and signal samples respectively.

4.11.1 Hadronic sample

Assume there are N bins in H_{T}, in this case $N = 8$, not necessarily of equal width. Then n^i is the number of events passing the selection requirements in H_{T} bin i, b^i is the number of expected SM background events in H_{T} bin i, and s^i is the expected yield of signal events in i. The likelihood for the hadronic sample can then be defined as

$$L_{\mathrm{hadronic}} = \prod_i \mathrm{Pois}\big(n^i | b^i + s^i\big) \tag{4.14}$$

where it is assumed $b^i \equiv \mathrm{EWK}^i + \mathrm{QCD}^i$ where EWK^i is the expected number of background electroweak events and QCD^i is the expected number of background QCD events in H_{T} bin i.

4.11.2 Parameters evolving with H_T

As discussed in Section 4.8.2 it is hypothesized that for for any process p the ratio between events above and below the α_T cut value $\alpha_T = 0.55$ falls exponentially with H_T, that is

$$R_{\alpha_T}(H_\mathrm{T}) = Ae^{-kH_\mathrm{T}} \tag{4.15}$$

and the parameters A and k have their values determined from a fit. In an H_T bin i we denote the number of events below the α_T threshold as m_i, and their mean H_T values as $\langle H_\mathrm{T}\rangle^i$. Then the expected background b_p^i from the process p is

$$b_p^i = \int_{x_i}^{x_{i+1}} \frac{dN}{dH_\mathrm{T}} R_{\alpha_T} dH_\mathrm{T} \tag{4.16}$$

where the integral is performed over the lower and upper bin edges, $\frac{dN}{dH_\mathrm{T}}$ is the distribution in H_T of events failing the α_T cut. In this analysis it is assumed that the per-bin distribution of events all occur at the mean value of H_T, $\langle H_\mathrm{T}\rangle^i$.

Equation 4.16 can then be rewritten as

$$b_p^i = \int_{x_i}^{x_{i+1}} m^i \delta\Big(x - \langle H_\mathrm{T}\rangle^i\Big) Ae^{-kx} dx = m^i Ae^{-k\langle H_\mathrm{T}\rangle^i} \tag{4.17}$$

where we identify

$$\mathrm{EWK}^i = m^i A_\mathrm{EWK} \tag{4.18}$$

$$\mathrm{QCD}^i = m^i A_\mathrm{QCD} e^{-k_\mathrm{QCD}\langle H_\mathrm{T}\rangle^i} \tag{4.19}$$

i.e. the EWK background is a constant scale and the QCD multijet background falls with H_T.

4.11.3 Electroweak samples

As discussed in Section 4.7 the only irreducible SM background comes from $\mathrm{Z} \to \nu\overline{\nu}$+jets . A good fit to the proportion of EWK background that comes from $\mathrm{Z} \to \nu\overline{\nu}$ is to model it as a linear function of H_{T}. That is,

$$f^{i}_{\mathrm{Zinv}} \equiv \frac{\mathrm{EWK}^{i}_{\mathrm{Zinv}}}{\mathrm{EWK}^{i}} \tag{4.20}$$

such that $f^{i}_{\mathrm{Zinv}} \in [0,1]$. Since we model the H_{T} dependence of f_{Zinv} as linear, two floating parameters can be defined f^{0}_{Zinv} and f^{N-1}_{Zinv}. These are the proportion of EWK background that is from $\mathrm{Z} \to \nu\overline{\nu}$ in the first bin, and the last bin respectively. Hence, the contribution of $\mathrm{Z} \to \nu\overline{\nu}$ in any bin i can be calculated,

$$f^{i}_{\mathrm{Zinv}} = f^{0}_{\mathrm{Zinv}} + \frac{\langle H_{\mathrm{T}}\rangle^{i} - \langle H_{\mathrm{T}}\rangle^{0}}{\langle H_{\mathrm{T}}\rangle^{N-1} - \langle H_{\mathrm{T}}\rangle^{0}} \left(f^{N-1}_{\mathrm{Zinv}} - f^{0}_{\mathrm{Zinv}} \right) \tag{4.21}$$

One can also define ttW^{i}, that is the expected number of events from SM W-boson production which also includes decays from top quarks which are in the signal sample, such that

$$\mathrm{ttW}^{i} \equiv \left(1 - f_{\mathrm{Zinv}}\right) \times \mathrm{EWK}^{i} \tag{4.22}$$

$$\mathrm{EWK}^{i} \equiv \mathrm{ttW}^{i} + \mathrm{Zinv}^{i} \tag{4.23}$$

where Zinv^{i} is the raw number of $\mathrm{Z} \to \nu\overline{\nu}$ events expected in H_{T} bin i of the signal sample, defined as $\mathrm{Zinv}^{i} \equiv f^{i}_{\mathrm{Zinv}}\mathrm{EWK}^{i}$.

For each bin of the photon and muon control samples we define n^{i}_{ph}, n^{i}_{μ}, $n_{\mu\mu}$, MC^{i}_{ph}, MC^{i}_{μ}, and $MC^{i}_{\mu\mu}$ where n_X are the event counts in the X control sample, and MC_X is the corresponding yield in the MC.

The MC simulation also provides expected compositions of Zinv and ttW in the signal sample denoted MC_{Zinv} and MC_{ttW}. The MC simulations used on CMS analyses have been validated extensively [14].

One can subsequently define ratios,

$$r^i_{ph} = \frac{MC^i_{ph}}{MC^i_{\mathrm{Zinv}}} \tag{4.24}$$

$$r^i_{\mu\mu} = \frac{MC^i_{\mu\mu}}{MC^i_{\mathrm{Zinv}}} \tag{4.25}$$

$$r^i_{\mu} = \frac{MC^i_{\mu}}{MC^i_{\mathrm{ttW}}} \tag{4.26}$$

which are then used to define the likelihood functions

$$L_{ph} = \prod_i \mathrm{Pois}\Big(n^i_{ph}|\rho^j_{ph\mathrm{Z}} r^i_{ph} \mathrm{Zinv}^i\Big) \tag{4.27}$$

$$L_{\mu\mu} = \prod_i \mathrm{Pois}\Big(n^i_{\mu\mu}|\rho^j_{\mu\mu\mathrm{Z}} r^i_{\mu\mu} \mathrm{Zinv}^i\Big) \tag{4.28}$$

$$L_{\mu} = \prod_i \mathrm{Pois}\Big(n^i_{\mu}|\rho^j_{\mu\mathrm{W}} r^i_{\mu} \mathrm{ttW}^i + s^i_{\mu}\Big) \tag{4.29}$$

where $\mathrm{Pois}(n|\lambda)$ denotes the Poisson distribution function $f(n|\lambda) = \frac{\lambda^n e^{-\lambda}}{k!}$.

These can then be used to cross-predict the composition of our sample. For example, equation (4.27) can be used to estimate the value for Zinv^i given knowledge of the photon control sample. Zinv^i can also be estimated from the di-muon control sample and the single muon control sample can be used to estimate ttW^i. Note, that these ratios r_X are the *inverses* of the translation factors (equation (4.7)).

The parameters denoted ρ_X are correction factors to accommodate the systematic uncertainties associated with the control-sample background constraints as described in Section 4.10. Further, the relative systematic uncertainties for the control sample constraints can be taken account with likelihood functions,

$$L_{\text{EWK syst}} = \prod_j \text{Gauss}\Big(1.0|\rho^j_{\mu\text{W}}, \sigma^j_{\mu\text{W}}\Big) \times \text{Gauss}\Big(1.0|\rho^j_{\mu\mu\text{Z}}, \sigma^j_{\mu\mu\text{Z}}\Big) \times \text{Gauss}\Big(1.0|\rho^j_{ph\text{Z}}, \sigma^j_{ph\text{Z}}\Big) \tag{4.30}$$

where Gauss$(x|\mu,\sigma)$ is the Gaussian distribution function $f(x|\mu,\sigma) = \frac{1}{\sigma\sqrt{2\pi}}e^{-\frac{(x-\mu)^2}{2*\sigma^2}}$ and σ_X are the uncertainties on their respective ρ_X terms.

As detailed in Section 4.8.1, at high b-multiplicity ($n_b \geq 2$) the statistics of some of the MC samples are insufficient to use the same method, as such the single muon control sample is used to predict the total electroweak background. Defining the ratio

$$r' \equiv \frac{MC^i_\mu}{MC^i_{\text{ttW+Zinv}}} \tag{4.31}$$

and hence the likelihood term

$$L_\mu = \prod_i \text{Pois}\Big(n^i_\mu|\rho^j_{\mu\text{W}} r'^i_\mu \text{EWK}^i + s^i_\mu\Big) \tag{4.32}$$

In this case, the likelihood terms from the photon and di-muon likelihoods are ignored, and the parameters f_{Zinv} are also dropped.

4.11.4 Signal contribution

For a particular H_T bin i, our analysis has an efficiency ϵ^i_{had} (ϵ^i_μ) for the hadronic signal (single muon control) sample. There is a relative uncertainty, δ, on the signal yield which is assumed to be fully correlated among the H_T bins, and hence there is a correction factor ρ_{sig} to accommodate this uncertainty.

If there is a particular signal model with cross section x and the analysis considers a recorded luminosity l, then the expected yield in the hadronic signal selection is defined

$$s^i \equiv f\rho_{sig}xl\epsilon^i_{had} \tag{4.33}$$

and the signal contamination in the muon control sample is defined similarly

$$s^i_\mu \equiv f\rho_{sig}xl\epsilon^i_\mu \tag{4.34}$$

where f is a multiplicative factor on the cross section of the signal model which shall have a range determined.

The likelihood model then requires a term to account for the systematic uncertainty on the signal,

$$L_{sig} = \text{Gauss}(1.0|\rho_{sig}, \delta) \tag{4.35}$$

4.11.5 Combined likelihood

For any selection k the likelihood is given as

$$L^k = L^k_{\text{hadronic}} \times L^k_\mu \times L^k_{ph} \times L^k_{\mu\mu} \tag{4.36}$$

Each selection has $3 + N$ associated nuisance parameters: the QCD normalization factor A_{QCD}, the fractional values of Zinv in the EWK background f^0_{Zinv} and f^{N-1}_{Zinv}, and the N electroweak background yields $\{\text{EWK}^i\}^{N-1}_{i=0}$, where N is the number of bins in the selection (e.g. the eight H_T bins).

There are 11 parameters used to describe the SM background, constructed from the sum of the EWK and QCD contributions: the QCD H_T evolution decay constant k_{QCD}, the signal correction factor ρ_{sig} and the sets of the three correction factors $\rho^j_{ph\text{Z}}, \rho^j_{\mu\mu\text{Z}}$ and $\rho^j_{\mu\text{W}}$ with $j \in \{0, 1, 2\}$. So the total likelihood is then given by,

$$L = L_{sig} \times L_{\text{EWK sys}} \times \prod_k \left(L^k_{\text{hadronic}} \times L^k_\mu \times L^k_{ph} \times L^k_{\mu\mu}\right) \tag{4.37}$$

4.12 Fitting models

For a particular signal model, the likelihood is maximised over all parameters thus providing parameter values and yields from the fit with uncertainties that are determined from pseudo-experiments.

Further, a goodness of fit can be determined following the procedure laid out in [103]. For a particular data set $L^{\text{model}}_{\text{max}}$ is noted. Then treating the likelihood function at the Maximum Likelihood (ML) values as an Probability Distribution Function (PDF) pseudo-experiments can be created. For each pseudo-experiment the maximisation routine is repeated and the value of $L^{\text{max}}_{\text{pseudo}}$ is noted. A histogram of the values of $L^{\text{max}}_{\text{pseudo}}$ is then constructed and the p-value of the model being tested is the quantile of $L^{\text{data}}_{\text{max}}$ in this histogram.

In the case of testing the SM the same procedure is carried out but the signal terms in the likelihood function are ignored.

4.13 Testing signal models

The CL_s method, described in [102], is used to test signal models. A test statistic, fully described in [47], is selected to rank models in terms of their signal-like properties,

$$q_\mu = \begin{cases} -2\log\lambda(\mu) & \mu > \hat{\mu} \\ 0 & \text{otherwise} \end{cases} \tag{4.38}$$

where μ is the same multiplicative factor on the signal cross-section as f in equation (4.34), $\lambda(\mu)$ is the profile likelihood ratio defined as

$$\lambda(\mu) = \frac{L(\mu, \theta_\mu)}{L\left(\hat{\mu}, \hat{\theta}\right)} \tag{4.39}$$

where $\hat{\mu}$ is the ML value of μ, $\hat{\theta}$ is the set of ML valued nuisance parameters, and θ_μ is the set of conditional ML values of the nuisance parameters for a given value of the signal strength μ.

For a given model treated at nominal cross-section ($\mu = 1$), pseudo-experiments are produced in a similar manner as described in Section 4.12. The values $\mathrm{CL_{s+b}}$ and $\mathrm{CL_b}$ are defined as one minus the quantile of the observed value of q_1 in the signal+background and background-only distributions respectively. Further $\mathrm{CL_s}$ is defined as $\mathrm{CL_s} \equiv \mathrm{CL_{s+b}}/\mathrm{CL_b}$. Hence a model can be said to be excluded at $X\%$ if the $\mathrm{CL_s} \leq 1. - (X/100)$.

4.14 Results

4.14.1 Standard Model Fit

The fit described in Section 4.12 is carried out for the SM. Figures 4.4, 4.5, 4.6 and 4.7 show comparisons of observed yields and SM expectations given by this fit in the bins of H_T with zero, one, two, and more than two b-tagged jets per event respectively for the signal region in $\alpha_T > 0.55$. Across all b-tag categories good agreement is observed between the SM expectation and the observed yields in data. There is no significant excess above the SM expectation. More quantitative details of the fit and yields are summarised in Table 4.2. It should be noted that the shape difference in the $n_b \geq 1$ slices in the $\mu +$jets and $\mu\mu +$jets samples is due to the different trigger requirements in the $H_\mathrm{T} \lesseqgtr 375$ regions, described in Section 4.8.1.

H_T (GeV)	275–325	325–375	375–475	475–575	575–675	675–775	775–875	875–∞
0 b jets SM	2933^{+56}_{-52}	1139^{+17}_{-40}	783^{+17}_{-27}	261^{+14}_{-8}	$81.5^{+6.5}_{-6.5}$	$34.2^{+4.0}_{-3.8}$	$10.4^{+2.8}_{-1.8}$	$5.3^{+1.7}_{-1.1}$
0 b jets Data	2919	1166	769	255	91	31	10	4
1 b jet SM	630^{+26}_{-25}	271^{+10}_{-16}	202^{+10}_{-6}	$78.0^{+6.9}_{-1.9}$	$24.2^{+2.9}_{-2.0}$	$10.6^{+1.7}_{-1.3}$	$2.9^{+0.9}_{-0.5}$	$2.2^{+0.7}_{-0.4}$
1 b jet Data	614	294	214	71	20	6	4	0
2 b jets SM	162^{+13}_{-12}	$61.8^{+4.8}_{-6.3}$	$58.8^{+4.8}_{-2.6}$	$28.0^{+3.5}_{-1.1}$	$9.0^{+1.4}_{-1.0}$	$7.1^{+1.4}_{-1.0}$	$0.6^{+0.3}_{-0.2}$	$0.9^{+0.4}_{-0.2}$
2 b jets Data	160	68	52	19	11	7	0	2
≥ 3 b jets SM	$10.5^{+3.5}_{-2.2}$	$7.1^{+2.2}_{-1.8}$	$5.8^{+1.4}_{-0.9}$	$3.1^{+1.0}_{-0.7}$	$1.7^{+0.5}_{-0.4}$	$0.7^{+0.5}_{-0.4}$	$0.1^{+0.1}_{-0.1}$	$0.2^{+0.1}_{-0.1}$
≥ 3 b jets Data	10	8	8	1	0	0	0	0

Table 4.2: Comparison of the measured yields in the different H_T and b jet multiplicity bins for the hadronic sample with the SM expectations and combined statistical and systematic uncertainties given by the simultaneous fit.

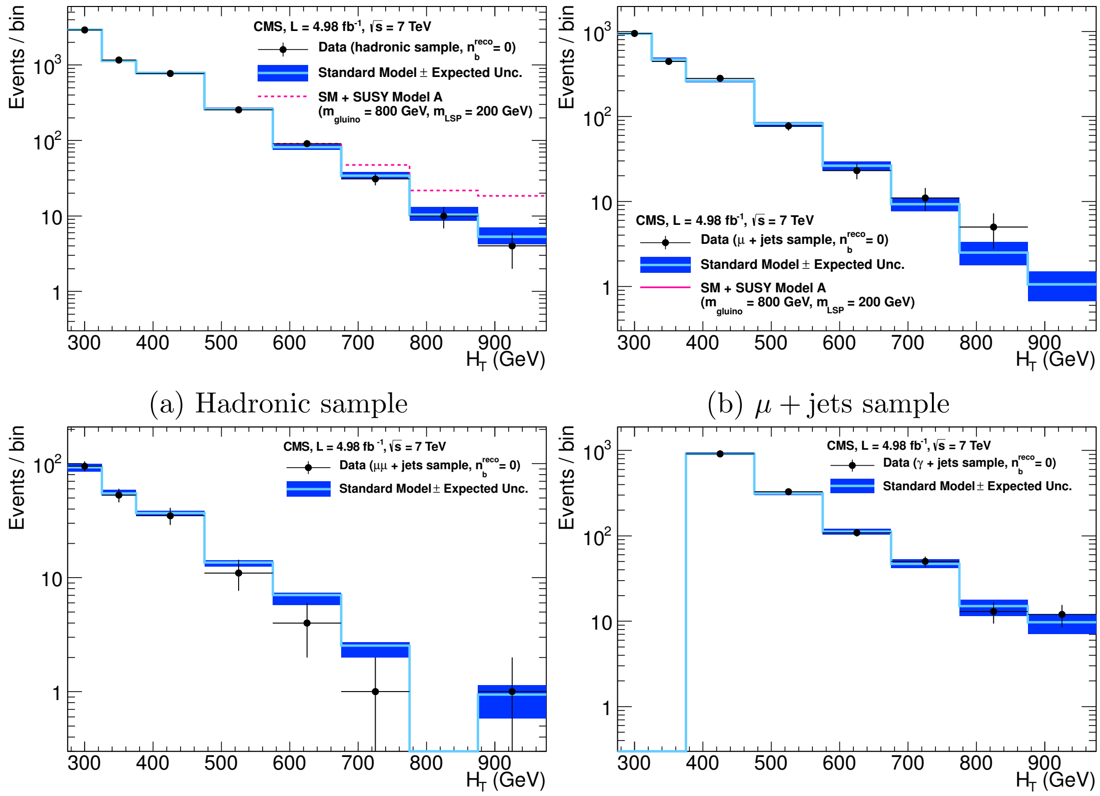

(a) Hadronic sample

(b) $\mu +$ jets sample

(c) $\mu\mu +$ jets sample

(d) $\gamma +$ jets sample

Figure 4.4: Comparison of the observed yields and SM expectations given by the simultaneous fit in bins of H_{T} for the (a) hadronic, (b) $\mu +$ jets, (c) $\mu\mu +$ jets, and (d) $\gamma +$ jets samples when requiring exactly zero reconstructed b-jets. The black dots show the observed event yields in data, and the light blue solid line with dark banding shows the expectation and uncertainty determined by the simultaneous fit. A sample signal model is superimposed as the magenta solid line[43].

4.14.2 Model limits

This analysis sets limits in the cMSSM parameter space as well as in various Simplied Model Spectra (SMS).

cMSSM

In the case of the cMSSM a signal model is defined to be a single point in the cMSSM parameter space defined by four continuous parameters and one binary parameter. In

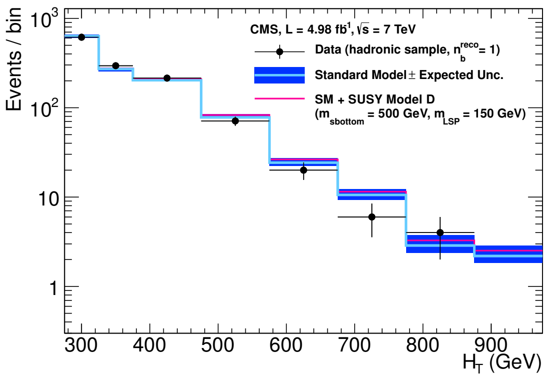

(a) Hadronic sample

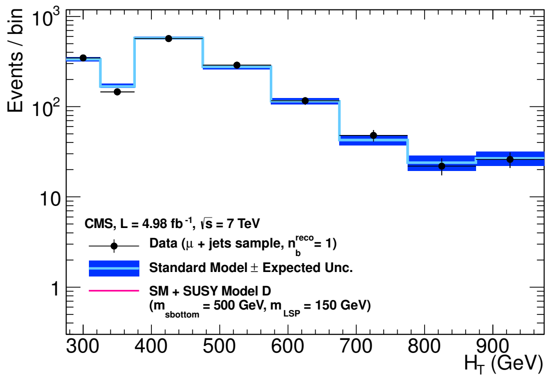

(b) $\mu +$ jets sample

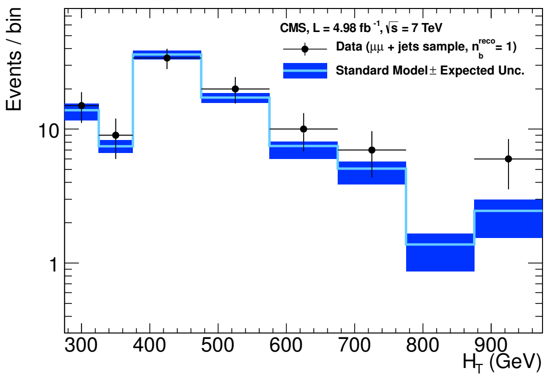

(c) $\mu\mu +$ jets sample

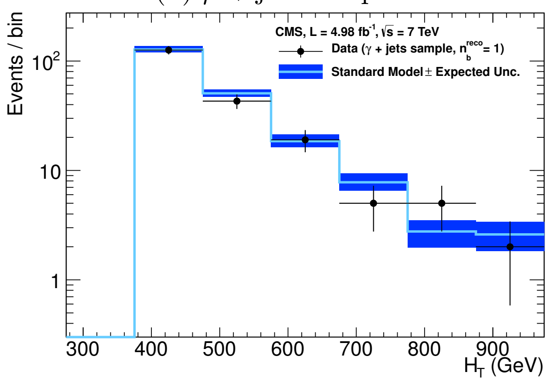

(d) $\gamma +$ jets sample

Figure 4.5: Comparison of the observed yields and SM expectations given by the simultaneous fit in bins of H_{T} for the (a) hadronic, (b) $\mu +$ jets, (c) $\mu\mu +$ jets, and (d) $\gamma +$jets samples when requiring exactly one reconstructed b-jet. The black dots show the observed event yields in data, and the light blue solid line with dark banding shows the expectation and uncertainty determined by the simultaneous fit. A sample signal model is superimposed as the magenta solid line[43].

this analysis, we consider the binary parameter, sign(μ), to be fixed along with two of the four continuous parameters. Specifically,

$$\tan\beta = 10, A_0 = 0, \mathrm{sign}(\mu) = 1 \tag{4.40}$$

and the remaining two mass-scale parameters are scanned. m_0 is scanned in steps of 20GeV in the range $[0, 2\mathrm{TeV}]$, and $m_{1/2}$ is scanned in steps of 20GeV in the range $[0, 800\mathrm{GeV}]$. At each point in the scan the mass spectrum is calculated and signal events

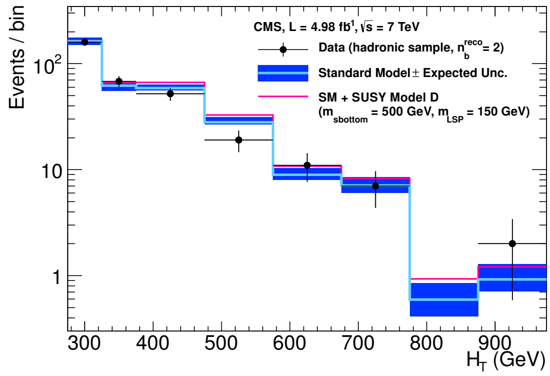

(a) Hadronic sample

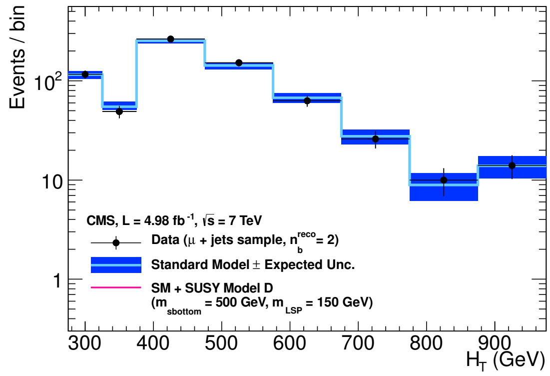

(b) $\mu +$ jets sample

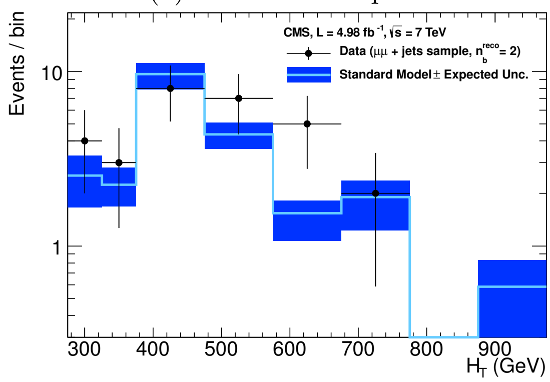

(c) $\mu\mu +$ jets sample

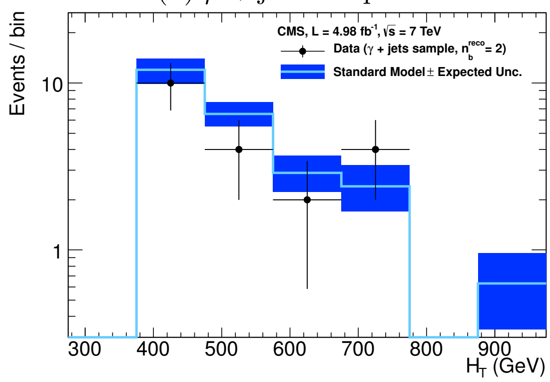

(d) $\gamma +$ jets sample

Figure 4.6: Comparison of the observed yields and SM expectations given by the simultaneous fit in bins of H_{T} for the (a) hadronic, (b) $\mu +$ jets, (c) $\mu\mu +$ jets, and (d) $\gamma +$ jets samples when requiring exactly two reconstructed b-jets. The black dots show the observed event yields in data, and the light blue solid line with dark banding shows the expectation and uncertainty determined by the simultaneous fit. A sample signal model is superimposed as the magenta solid line[43].

are generated. These simulated events are reweighted such that the distribution of the number of reconstructed vertexes per beam crossing matches between simulation and data.

Signal contributions to each of the four data samples are allowed but this contribution is only significant in the cMSSM for the hadronic signal sample.

Figure 4.8 shows the observed and expected exclusion limit for the cMSSM using the $\mathrm{CL_s}$ method in the m_0 ,$m_{1/2}$ plane. For this set of fixed input parameters this analysis excludes $m_{\tilde{q}} < 1250\mathrm{GeV}$ at 95% CL. For the region $m_0 < 600$, $m_{\tilde{g}} < 1250$ is also

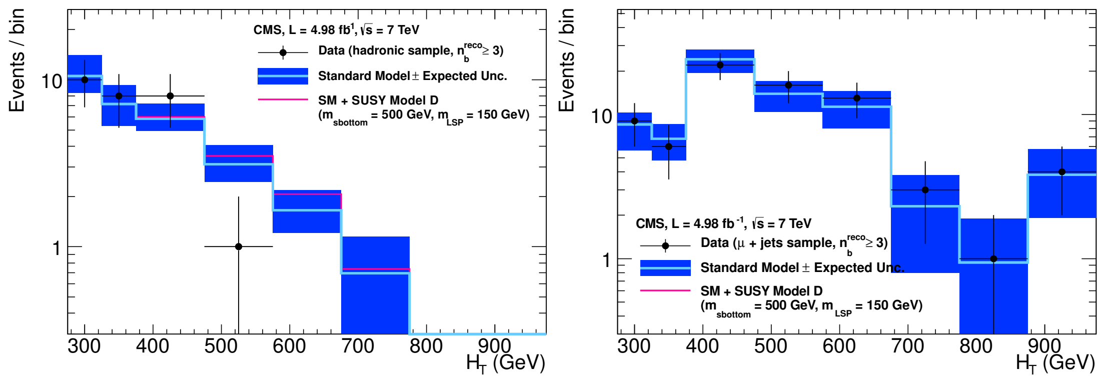

(a) Hadronic sample (b) $\mu +$ jets sample

Figure 4.7: Comparison of the observed yields and SM expectations given by the simultaneous fit in bins of H_{T} for the (a) hadronic and (b) $\mu +$ jets samples when requiring exactly two reconstructed b-jets. The black dots show the observed event yields in data, and the light blue solid line with dark banding shows the expectation and uncertainty determined by the simultaneous fit. A sample signal model is superimposed as the magenta solid line[43].

excluded at the same confidence. For m_0 in the region $600 < m_0 < 3000$GeV this analysis excludes $m_{\widetilde{g}} < 700$GeV and $m_{\widetilde{q}} < 1250 - 2500$ depending on m_0 , again all at 95% CL.

Simplied Model Spectra

Though the cMSSM provides varied particle spectra it is, by its definition, restricted from representing the full range of possible phenomenology within the MSSM. In particular the cMSSM has a near-fixed relationship between the gluino mass and the LSP ($\widetilde{\chi}^0_1$) ($m_{\widetilde{g}} \sim 6 \times m_{\widetilde{\chi}^0_1}$). To account for this several SMS are selected. These are models which consist of only a few particles, where the remaining SUSY spectra is considered to be at sufficiently high masses that they have negligible contribution to any process, and hence have a low number of input parameters.

To account for fixed mass ratios in the cMSSM SMSs are selected where the mass splitting between the produced $\widetilde{g}$ or $\widetilde{q}$ and the LSP is small and the rest of the sparticles are decoupled. The models `T1` and `T2` characterize the pair production of gluinos and 1$^{\mathrm{st}}$ and 2$^{\mathrm{nd}}$ generation squarks respectively, and the mass splitting between these pair produced

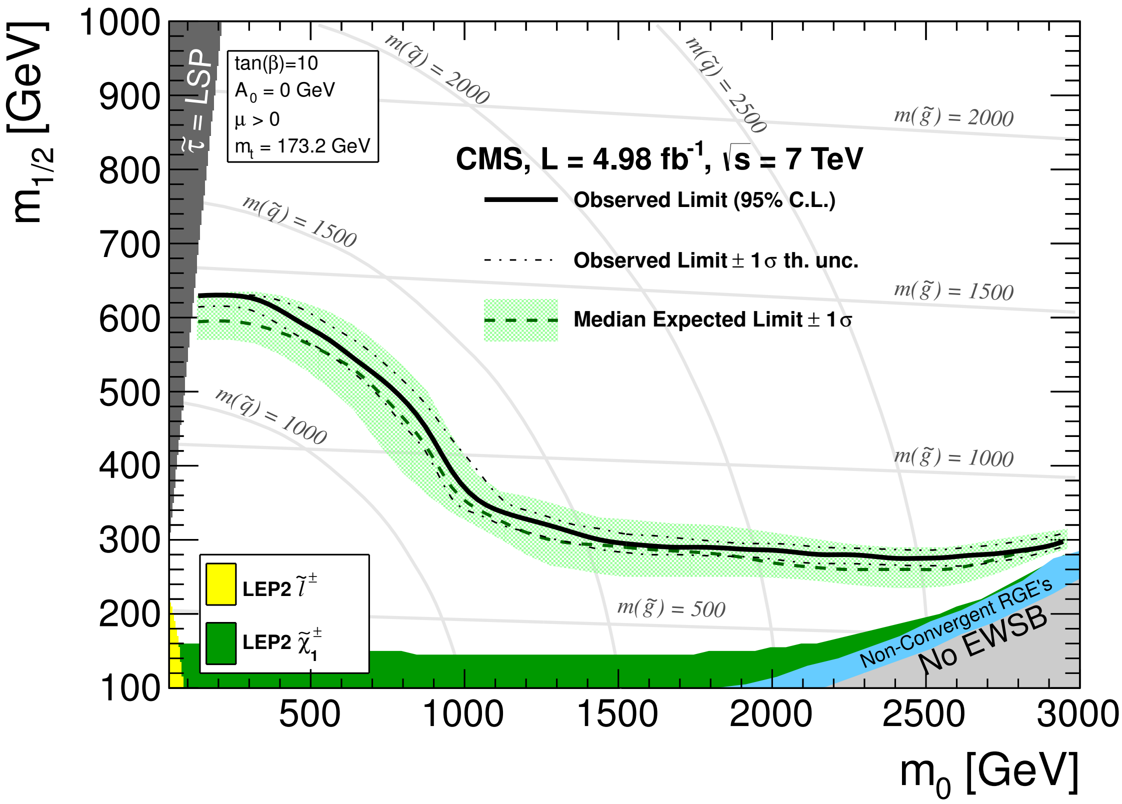

Figure 4.8: Exclusion contours at 95% CL in the cMSSM m_0 ,$m_{1/2}$ plane ($\tan\beta = 10, A_0 = 0, \mu > 0$) using the $\mathrm{CL_s}$ method. The solid black line indicates the observed exclusion region. The dotted-dashed black lines represent the observed excluded region when varying the cross-section by its theoretical uncertainty. The green dashed line and green band represent the expected median exclusion and the $\pm 1\sigma$ region respectively[43].

particles and the LSP. `T2tt`, `T2bb`, `T1tt`, and `T1bbbb` described various production an decay modes in the context of 3$^{\text{rd}}$ generation squarks. Each SMS under consideration, and their respective production and decay modes, are summarized in Table 4.3.

In general SMS with names beginning `T1` have direct pair-produced gluinos which decay via offshell quarks of the relevant flavour to the final states listed. For SMS with names beginning `T2` we get direct pair production of the squarks, and these decay directly to the listed final states.

Again, as in the cMSSM, the yield on signal events in the control samples is negligible.

Model	Production and decay modes
`T1`	$\widetilde{g}\widetilde{g} \rightarrow q\bar{q}\widetilde{\chi}^0 q\bar{q}\widetilde{\chi}^0$
`T2`	$\widetilde{q}\widetilde{q} \rightarrow q\widetilde{\chi}^0\bar{q}\widetilde{\chi}^0$
`T2tt`	$\widetilde{t}\widetilde{t} \rightarrow t\widetilde{\chi}^0\bar{t}\widetilde{\chi}^0$
`T2bb`	$\widetilde{b}\widetilde{b} \rightarrow b\widetilde{\chi}^0\bar{b}\widetilde{\chi}^0$
`T1tttt`	$\widetilde{g}\widetilde{g} \rightarrow t\bar{t}\widetilde{\chi}^0 t\bar{t}\widetilde{\chi}^0$
`T1bbbb`	$\widetilde{g}\widetilde{g} \rightarrow b\bar{b}\widetilde{\chi}^0 b\bar{b}\widetilde{\chi}^0$

Table 4.3: Production and decay modes for various simplified models.

The mass of both inputs is varied in steps of 25GeV, and at each model point 10000 events are generated and processed through the detector simulation and reconstruction chain. For a given mass pairing, an observed upper limit on the cross-section is computed, i.e. the value of the multiplicative factor on the cross-section (μ) for which $\mathrm{CL_s} = 0.05$ is calculated following the method described in Section 4.13.

These observed cross-section limits are shown in Figure 4.9 for each of the simplified models. The thicker solid black lines enclose the observed exclusion region, and the thinner black lines show the observed excluded region when the cross-section is varied by its theoretical uncertainty. The thick and dashed purple lines indicate the median expected exclusion and the $\pm 1\sigma$ experimental uncertainty regions respectively.

The general trend of the worsening limit on the cross-section as the mass of the parent particle decreases for fixed LSP mass is due to decreasing expected $E_{\mathrm{T}}^{\mathrm{miss}}$ in the events. As the difference between the daughter and parent particle masses is reduced one expects the resulting sparticles that escape the detector to be less boosted and hence produce a smaller $E_{\mathrm{T}}^{\mathrm{miss}}$ signature, thereby reducing the limit that can be put on the cross-section for processes in this region of parameter space.

The highest impact regions of the limits on the pair production of sparticles are observed at low LSP masses, where as the LSP mass increases and the spectra becomes compressed the limit on the pair produced sparticles weakens. This is due to the nature of compressed spectra, as the daughter and parent particles mass separation decreases, the decay produces significantly softer jets. For all models considered there is a value of the LSP mass for which the limit falls off entirely. For example, in the `T1` model (Figure 4.9a) for low

LSP masses gluinos masses of 950GeV are excluded and this falls to below 900GeV when $m_{\text{LSP}} > 350$GeV. The limit rapidly disappears and for $m_{\text{LSP}} > 400$GeV no limit can be placed on $m_{\widetilde{q}}$.

In the case of direct squark pair production Figure 4.9c shows that there is no expected exclusion for $m_{\text{LSP}} > 50$GeV. However a small exclusion is observed. Figure 4.10 shows this observed upper limit at 95% CL as a function of $m_{\widetilde{\mathrm{t}}}$ for a fixed $m_{\text{LSP}} = 50$GeV.

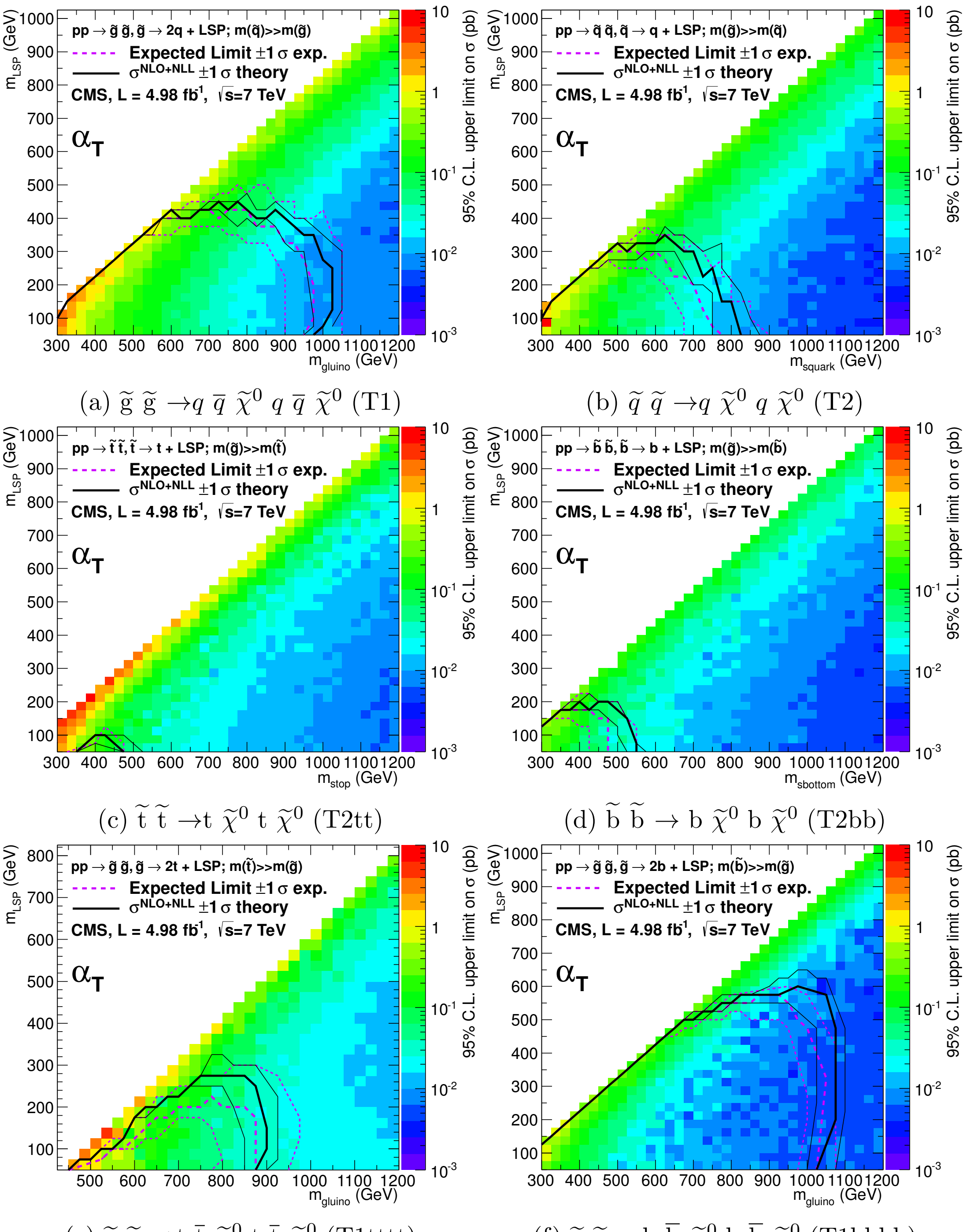

(a) $\tilde{g}\ \tilde{g} \rightarrow q\ \bar{q}\ \tilde{\chi}^0\ q\ \bar{q}\ \tilde{\chi}^0$ (T1)

(b) $\tilde{q}\ \tilde{q} \rightarrow q\ \tilde{\chi}^0\ q\ \tilde{\chi}^0$ (T2)

(c) $\tilde{\mathrm{t}}\ \tilde{\mathrm{t}} \rightarrow \mathrm{t}\ \tilde{\chi}^0\ \mathrm{t}\ \tilde{\chi}^0$ (T2tt)

(d) $\tilde{\mathrm{b}}\ \tilde{\mathrm{b}} \rightarrow \mathrm{b}\ \tilde{\chi}^0\ \mathrm{b}\ \tilde{\chi}^0$ (T2bb)

(e) $\tilde{g}\ \tilde{g} \rightarrow \mathrm{t}\ \bar{\mathrm{t}}\ \tilde{\chi}^0\ \mathrm{t}\ \bar{\mathrm{t}}\ \tilde{\chi}^0$ (T1tttt)

(f) $\tilde{g}\ \tilde{g} \rightarrow \mathrm{b}\ \bar{\mathrm{b}}\ \tilde{\chi}^0\ \mathrm{b}\ \bar{\mathrm{b}}\ \tilde{\chi}^0$ (T1bbbb)

Figure 4.9: Upper limit on cross section at 95% CL as a function of $m_{\tilde{q}}$ or $m_{\tilde{g}}$ and $m_{\rm LSP}$ for various simplified models. The solid thick black line indicates the observed exclusion region. The thin black lines represent the observed excluded region when varying the cross section by its theoretical uncertainty. The dashed purple thick and thin lines represent the median expected and $\pm1\sigma$ exclusion regions respectively[43].

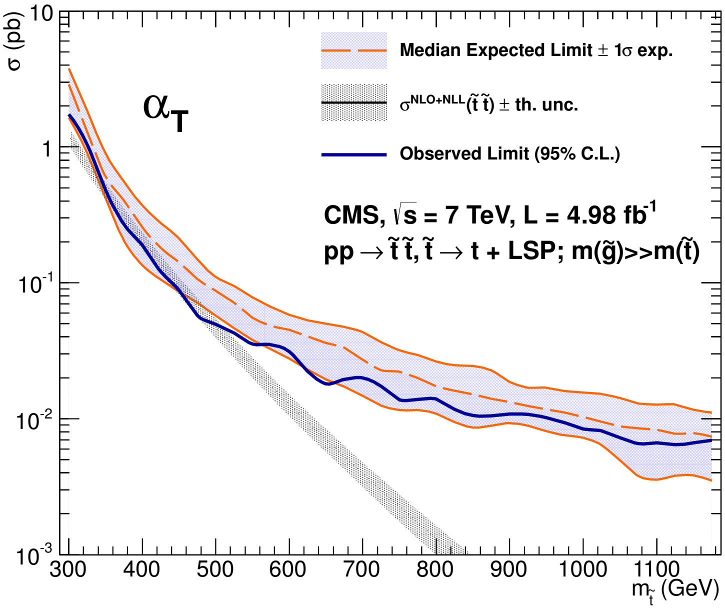

Figure 4.10: Excluded cross section versus top squark mass for the `T2tt` SMS. The solid blue line indicates the observed cross section upper limit at 95% CL as a function of the top squark mass, $m_{\tilde{t}}$. The dashed orange line and blue band indicate the median expected excluded cross section with experimental uncertainties. The solid black line with grey band indicated the NLO+NLL SUSY top squark pair-production cross section and theoretical uncertainties[43]

4.15 Summary of analysis

A search for supersymmetry was carried out based on a data sample corresponding to an integrated luminosity of 4.98fb^{-1} recorded at $\sqrt{s} = 7$TeV. Events were selected with final states consisting of at least two jets and significant $E_{\mathrm{T}}^{\mathrm{miss}}$, characteristic of the decay of high-mass pair produced sparticles. This search bins the signal region in H_{T} and the number of jets identified as originating from a bottom quark n_b. The SM background for each bin is estimated from a simultaneous binned likelihood fit to hadronic, $\mu +$ jets, $\mu\mu$ + jets and γ + jets samples. The observed data show no significant excess over the expected SM yields. Limits have been calculated in the cMSSM in the m_0 ,$m_{1/2}$ plane while the other parameters remained fixed as $\tan\beta = 10, A_0 = 0, \mu > 0$. In this selection of signal models this analysis excluded $m_{\tilde{\mathrm{g}}} < 700$GeV at 95% CL, increasing to $m_{\tilde{\mathrm{g}}} < 1250$ when $m_{\tilde{\mathrm{g}}} \sim m_{\tilde{q}}$.

Limits in simplified models are also calculated, where these models are selected to more fully cover possible phenomenology in the MSSM and also provide a special emphasis on third generation and compressed spectra scenarios. In the case of simplified models with squark pair production 1$^{\text{st}}$ and 2$^{\text{nd}}$ generation squarks are excluded for $m_{\tilde{q}} < 750$GeV for low m_{LSP}, and bottom squarks are excluded up to approximately 500GeV. It should be noted that in all simplified models presented the limit on m_{LSP} is significantly below 1TeV indicating that there still exists significant portions of SUSY parameter space not yet probed at the LHC. Though these results show the early stages of sensitivity to TeVscale supersymemtry, and we should expect future results to probe models at this scale aggressively.

Chapter 5

Constraining models of Supersymmetry

The most simple extensions of the Standard Model, discussed in Section 2.4, have at minimum four dimensions. However, it is common to see experimental results, as well as preferred regions of supersymmetric parameter space, described solely by the mass parameters. That is, the impact of the results are given in the $\left(m_0, m_{1/2}\right)$ plane while fixing $\tan\beta$ and A_0, for example see Figure 4.8 where the exclusion contour is shown with $\tan\beta = 10, A_0 = 0$.

When discussing preferred regions of a model's parameter space it is essential to incorporate the effect of all input parameters on observables, as many observables will have conflicting preferred regions for each parameter. Therefore, to fully quantify the possible range of phenomenological behaviour that these models can produce, as well as the impact of a combination of modern searches, it is necessary to scan over the full space of input parameters, calculating the value of observables at each point. It is then possible to assign a weighting to each point dependent on the consistency with any given list of measured observables. This allows statements to be made about the preferred regions of parameter space across all dimensions of the model account for any number of constraints, and hence assess the fit of the model to current experimental data.

In this analysis two models are considered, the cMSSM and the NUHM1 the details of which are disucssed in Section 2.4.1 and Section 2.4.3 respectively.

5.1 Statistical model

There are two fundamentally different approaches to quantifying this consistency, the Bayesian and frequentist interpretations of probability.

The Bayesian view is that the probability of a hypothesis H, given some data D, can be estimated given incomplete knowledge of the population and system, i.e.

$$P\left(H|D\right) = \frac{P\left(D|H\right)P\left(H\right)}{P\left(D\right)}, \tag{5.1}$$

where $P\left(H\right)$ is the probability of the hypothesis prior to the data, $P\left(D\right)$ is the probability of the data, $P\left(D|H\right)$ is the probability of the data D given the hypothesis H is true, and $P\left(H|D\right)$ is the probability of the hypothesis being true once the data D has been seen.

The frequentist approach is to interpret probability as the expected "frequency of occurrence" of an event defined by the hypothesis, that is

$$P\left(A\right) = \lim_{n_t \to \infty} \frac{n_A}{n_t} \tag{5.2}$$

where n_t is the total number of events and n_A is the total number of events where A occurred.

In this analysis the frequentist interpretation is used as, while there is a drawback of only being valid in the limit $n_t \to \infty$, it removes the dependence on priors inherent to the Bayesian interpretation (e.g. trying to specify a probability of the hypothesis being true). This is important as there is evidence that the calculations are sensitive to the choice of priors, at least for some models [123]. It is also possible to motivate the choice of frequentism in the case of a well sampled parameter space whose dependent variables are smoothly varying and define the likelihood for a given point, as in this case it becomes reasonable to assume the sample mean is in fact the true mean.

5.1.1 Chi-squared function

One can define a simple global χ^2 function to combine the constraints and the impact of the Standard Model parameters,

$$\chi^2 = \sum_i^N \frac{(C_i - P_i)^2}{\sigma(C_i)^2 + \sigma(P_i)^2} \tag{5.3}$$

where N is the number of observables, C_i is a measured value and P_i is the corresponding value predicted by the model being tested.

5.1.2 Standard Model inputs

The predictions of these minimal models of SUSY are also sensitive to SM parameters, and so in scanning over the parameter space of the models and determining the true range of phenomenological behavior, it is necessary to treat the most relevant of these inputs as nuisance parameters in the calculation of the χ^2,

$$\chi^2_{\mathrm{SM}} = \sum_i^M \frac{\left(f^{\mathrm{obs}}_{\mathrm{SM}_i} - f^{\mathrm{SUSY}}_{\mathrm{SM}_i}\right)^2}{\sigma\left(f_{\mathrm{SM}_i}\right)^2} \tag{5.4}$$

The three Standard Model parameters which need to be handled this way are denoted $f_{\mathrm{SM}} = \{\Delta\alpha_{\mathrm{had}}, m_t, m_Z\}$, and the current precision of their experimental measurement is $\sigma\left(f_{\mathrm{SM}_i}\right)$ where $\Delta\alpha_{\mathrm{had}}$ is the hadronic contribution to the shift in the electromagnetic fine structure constant, evaluated at scale $Q^2 = M_Z^2$, and m_t and m_Z are the mass of the top quark and Z-boson respectively. Originally these three parameters were chosen as they encapsulate the vast majority of the sensitivty of the observable in the early analyses as well as being well controlled experimentally. Now that the analysis is more mature and more observables are included it will become necessary to re-examine and extend this set of parameters, including e.g. α_S the strong coupling constant to which for instance the B-physics observables would be sensitive. However at this time, a full resampling with a new nuisance parameter was computationally prohibitive.

5.1.3 Model scanning

A Markov Chain Monte Carlo (MCMC) method is employed to scan the parameter spaces of the models. Specifically, a Metropolis-Hastings algorithm[93] MCMC is used to perform the sampling. An initial point, q_0, is chosen and an arbitrary proposal density is selected $Q(q|j)$ where j is the previous sample and $Q(q|j)$ is the probability density of q given j on which the only requirement is that Q be symmetric, i.e. $Q(q|j) = Q(j|q)$. In this implementation the standard choice is taken where Q is chosen to be a multi-dimensional Gaussian distribution centered around the previous sample j. To make a step t, a candidate q_c is selected from the distribution $Q(q_c|q_t)$, where q_t is the previous accepted candidate, and then an acceptance ratio is calculated;

$$\alpha = \frac{f(q_c)}{f(q_t)} = \frac{P(q_c)}{P(q_t)} \tag{5.5}$$

where P is the desired underlying distribution to be sampled, and f is some function which is proportional to the density of P. If $\alpha > 1$ it is automatically accepted, else it is accepted with probability α. Here we adjust the width of Q to keep the points with $\alpha < 1$ at an acceptance rate of $20 - 40\%$ to ensure a broad sample while remaining efficient.

It should be noted at this point that no use of the density of sampling is made to infer the underlying probability distribution P; rather, the MCMC method is used to construct a global χ^2 function that receives contributions from our constraints dependent on its position in parameter space.

For a single chain an initial point in the region of interest[1] is selected at random. The RGEs are solved to produce the mass spectrum and couplings at the EWK scale. These are then fed into a selection of programs to calculate the various observables of interest.

In this case `SoftSUSY` [16] is used to solve the RGEs. This result is then passed on to `FeynHiggs` [65] which modifies the Higgs sector. Finally this modified set of inputs is

[1]The region of interest is usually defined to be $m_0 < 4\text{TeV}$, $m_{1/2} < 4\text{TeV}$, $-5 < A_0 < 5\text{TeV}$, $2 < \tan\beta < 60$

Predictor	**Observables**
`SoftSUSY`	Couplings and sparticle mass spectrum
`FeynHiggs`	Higgs sector, $a_\mu^{\rm EXP} - a_\mu^{\rm SM}$, M_W
`MicrOMEGAs`	$\Omega_c h^2$, cross-check on $\sigma_p^{\rm SI}$
`SuperIso`	Cross-checks on $\mathrm{b} \to \mathrm{s}\gamma$ and $(g-2)_\mu$
`SSARD`	$\sigma_p^{\rm SI}$ and cross-check on $\Omega_c h^2$
`Bphysics`	$\mathrm{R}(\mathrm{BR}(\mathrm{b} \to \mathrm{s}\gamma))$, $\mathrm{BR}\left(\mathrm{B_s^0} \to \mu\mu\right)$, $\mathrm{R}(\mathrm{BR}(\mathrm{B} \to \tau\nu))$, $\mathrm{BR}\left(\mathrm{B_d^0} \to \mu\mu\right)$, $\mathrm{R}(\mathrm{BR}(\mathrm{B} \to X_s \ell\ell))$, $\mathrm{R}(\mathrm{BR}(\mathrm{K} \to \mu\nu))$, $\mathrm{R}(\mathrm{BR}(\mathrm{K} \to \pi\nu\overline{\nu}))$, $\mathrm{R}(\Delta\epsilon_K)$, $\mathrm{R}\left(\Delta M_{\mathrm{B_s^0}}\right)$, $\mathrm{R}\left(\Delta M_{\mathrm{B_s^0}}\right)/\mathrm{R}\left(\Delta M_{\mathrm{B_d^0}}\right)$
`FeynWZ`	$\sigma^0_{\rm had}$, R_l, $A_{\rm fb}(\ell)$, $A_\ell(P\tau)$, $R_{\rm b}$, $R_{\rm c}$, $A_{\rm fb}(b)$, $A_{\rm fb}(c)$, A_b, A_c, $A_\ell(\mathrm{SLD})$, $\sin^2\theta_{\rm w}^\ell(Q_{\rm fb})$, $m_{\rm W}$

Table 5.1: Listing of the observables obtained from each code-base

fed to `MicrOMEGAs` [25], `SuperIso` [89], `SSARD` [1], `Bphysics`[2], and `FeynWZ`[3] in turn. The list of observables retrieved from each program is given in Table 5.1. The values of these observables are then compared with measured values to calculate a χ^2 value for the point. This is then passed back to the controlling MCMC algorithm as the value of the target distribution at that point, and the next point is then selected. In general all attempts are made to make use of the most up to date values for all observables at the time of sampling / re-sampling.

5.1.4 Minimization

Once the parameter space has been sampled a minimization routine, for instance `MINUIT` [81], can be used to determine the best-fit point by minimization of the χ^2 with respect to the constraints. The point with the lowest χ^2 in the MCMC sampling is used as the *seed* point for the minimizer, and the program is run iteratively, with each point examined by the minimizer being added to the total sampling. Once the minimizer has completed, the parameter values are used to calculate a full χ^2 breakdown of the best fit point.

It should be noted that the LHC-era χ^2 contributions are not implemented when running the minimization routine, and as such only the pre-LHC minima have been calculated

[2]Private code

[3]Private code; based on the work in [76]

through use of minimization. For the post-LHC the minimum is defined to be the MCMC sampling point with lowest χ^2. This is due to the tools used to assess the contribution of the LHC-era constraints not having an interface with any of the available minimization routines.

P-Values

Using the χ^2 breakdown it is then possible to determine an effective p-value for the best fit point, and hence the lower limit of the fit of the model to current data.

The p-value for a chi-squared value of χ^2 with n degrees of freedom is calculated as,

$$D_r\left(\chi^2\right) = \frac{\gamma\left(\frac{1}{2}n, \frac{1}{2}\chi^2\right)}{\Gamma\left(\frac{1}{2}n\right)}, \tag{5.6}$$

where $\gamma(a, x)$ is the incomplete gamma function and $\Gamma(x)$ is the gamma function[18].

While the total χ^2 is easily calculated, due to the nature of some of the constraints the number of degrees of freedom, n, is not necessarily well known. In a simple case n is counted as

$$n = n_C - n_I, \tag{5.7}$$

where n_c is the number of constraints that produce a non-zero contribution to the total χ^2 at the point in question, and n_I is the number of inputs to the model. Some of the constraints implemented have non-zero values everywhere due to their asymptotic nature, for instance the χ^2 function approximations described in Section 5.3.1, . However, for some sets of input values the contribution to the total χ^2 is infinitesimally small and effectively flat for the neighborhood of the point.

For all other observables with non-asymptotic χ^2 functions, i.e. those given a Gaussian-like distribution (Table 5.2), the χ^2 calculation described in equation (5.3), when implemented programmatically, is unlikely to produce a χ^2-value of exactly zero due to the floating point representations used in the calculation.

Increasing the number of degrees of freedom for small or negligible increases in the total χ^2 causes a fall in the p-value. Hence, it is possible to arbitrarily lower the p-value of any point simply by increasing the list of observables that are used to calculate the χ^2. It therefore becomes necessary to impose a lower bound on the contribution to the χ^2 arising from a constraint for it to be included in the counting of n_C and hence the number of degrees of freedom. In this case this lower bound is chosen to be $\chi^2(q) > 0.1$ as in [33, 34, 32, 35].

5.2 Before the LHC

While the LHC has and will continue to significantly increase our sensitivity and ability to directly probe areas of supersymmetric parameter space, the existing constraints coming from searches for BSM physics can be applied to the parameter space of the models considered. This also allows a benchmark to be formed to assess the impact of LHC era searches for BSM physics.

Our full pre-LHC χ^2 function is constructed of several terms,

$$
\begin{aligned}
\chi^2 = &\sum_i^N \frac{\left(C_i - P_i\right)^2}{\sigma\left(C_i\right)^2 + \sigma\left(P_i\right)^2} \\
&+ \sum_i^M \frac{\left(f^{\text{obs}}_{\text{SM}_i} - f^{\text{SUSY}}_{\text{SM}_i}\right)^2}{\sigma\left(f_{\text{SM}_i}\right)^2} \\
&+ \chi^2(\text{SUSY search limits}) \\
&+ \chi^2_{\text{LEP}}\left(m_{\text{h}^0}\right).
\end{aligned} \tag{5.8}
$$

The first two terms have been discussed in Sections sections 5.1.1 and 5.1.2, respectively. The details of the measurements comprising the first term are given in Section 5.2.1. The final two terms are discussed in Sections 5.2.2 and 5.2.3 respectively.

5.2.1 Electroweak Precision Observables and B-Physics Observables

The precision to which the electroweak scale observables have been measured, for instance Flavour Changing Neutral Currents (FCNCs), and the degree to which they agree with the predictions of the SM allow constraints to be placed on the parameter space of any BSM theory. These are included through the first term of the χ^2 function described in equation (5.3). A listing of these observables and their values, along with other observables, is given in Table 5.2

5.2.2 Tevatron direct Supersymmetry searches

The direct searches for SUSY carried out at the Tevatron [13, 12] provided early lower bounds on the lightest of the sparticle masses,

$$\begin{aligned}
\min\left(m_{\widetilde{\chi}^{\pm}}\right) &> 103.0\mathrm{GeV}/c^2 \\
\min\left(m_{\widetilde{\ell}}\right) &> 90.0\mathrm{GeV}/c^2 \\
\min\left(m_{\widetilde{\nu}}\right) &> 90.0\mathrm{GeV}/c^2 \\
\min\left(m_{\widetilde{q}}\right) &> 90.0\mathrm{GeV}/c^2 \\
m_{\widetilde{\chi}_1^0} &> 50.0\mathrm{GeV}/c^2
\end{aligned} \tag{5.9}$$

where $m_{\widetilde{\chi}^{\pm}}$, $m_{\widetilde{\ell}}$, $m_{\widetilde{\nu}}$ and $m_{\widetilde{q}}$ are the masses of the charginos, sleptons, sneutrinos and squarks respectively.

Each of these is treated as a one-sided Gaussian lower limit with $\sigma = 1\mathrm{GeV}$. That is, for each point, if the relevant particle falls below this lower limit it takes a contribution

$$\chi^2 = \mathcal{G}(m|\mathrm{limit}, 1.0\mathrm{GeV}) \tag{5.10}$$

Each point is checked for consistency with these limits and a term appears in the χ^2

Observable	Source	Constraint
m_{t} [GeV]	[73]	173.2 ± 0.90
$\Delta\alpha_{\mathrm{had}}(\mathrm{Z})$	[50]	0.02749 ± 0.00010
m_{Z} [GeV]	[4]	91.1875 ± 0.0021
Γ_Z[GeV]	[76]/[4]	$2.4952 \pm 0.0023 \pm 0.001_{\mathrm{SUSY}}$
σ^0_{had} [nb]	[76]/[4]	41.540 ± 0.037
R_l	[76]/[4]	20.767 ± 0.025
$A_{\mathrm{fb}}(\ell)$	[76]/[4]	0.01714 ± 0.00095
$A_\ell(P\tau)$	[76]/[4]	0.1465 ± 0.0032
R_{b}	[76]/[4]	0.21629 ± 0.00066
R_{c}	[76]/[4]	0.1721 ± 0.0030
$A_{\mathrm{fb}}(b)$	[76]/[4]	0.0992 ± 0.0016
$A_{\mathrm{fb}}(c)$	[76]/[4]	0.0707 ± 0.0035
A_b	[76]/[4]	0.923 ± 0.020
A_c	[76]/[4]	0.670 ± 0.027
$A_\ell(\mathrm{SLD})$	[76]/[4]	0.1513 ± 0.0021
$\sin^2\theta^\ell_{\mathrm{w}}(Q_{\mathrm{fb}})$	[76]/[4]	0.2324 ± 0.0012
m_{W} [GeV]	[76]/[4]	$80.399 \pm 0.023 \pm 0.010_{\mathrm{SUSY}}$
$a_\mu^{\mathrm{EXP}} - a_\mu^{\mathrm{SM}}$	[100]/[26, 50]	$(30.2 \pm 8.8 \pm 2.0_{\mathrm{SUSY}}) \times 10^{-10}$
m_{h^0} [GeV]	[65]/[24, 105]	$> 114.4[\pm 1.5_{\mathrm{SUSY}}]$
$\mathrm{R}(\mathrm{BR}(\mathrm{b} \to \mathrm{s}\gamma))$	[48]/[23]	$1.117 \pm 0.076_{\mathrm{EXP}}$ $\pm 0.082_{\mathrm{SM}} \pm 0.050_{\mathrm{SUSY}}$
$\mathrm{BR}\left(\mathrm{B}^0_{\mathrm{s}} \to \mu\mu\right)$	[80]/[11, 108, 9, 45]	LHCb, CMS, ATLAS, CDF
$\mathrm{R}(\mathrm{BR}(\mathrm{B} \to \tau\nu))$	[80]/[23]	$1.43 \pm 0.43_{\mathrm{EXP+TH}}$
$\mathrm{BR}\left(\mathrm{B}^0_{\mathrm{d}} \to \mu\mu\right)$	[80]/[23]	$< 4.6[\pm 0.01_{\mathrm{SUSY}}] \times 10^{-9}$
$\mathrm{R}(\mathrm{BR}(\mathrm{B} \to X_s\ell\ell))$	[28]/[23]	0.99 ± 0.32
$\mathrm{R}(\mathrm{BR}(\mathrm{K} \to \mu\nu))$	[80]/[19]	$1.008 \pm 0.014_{\mathrm{EXP+TH}}$
$\mathrm{R}(\mathrm{BR}(\mathrm{K} \to \pi\nu\bar{\nu}))$	[36]/[22]	< 4.5
$\mathrm{R}\left(\Delta M_{\mathrm{B}^0_{\mathrm{s}}}\right)$	[36] /[29, 88]	$0.97 \pm 0.01_{\mathrm{EXP}} \pm 0.27_{\mathrm{SM}}$
$\mathrm{R}\left(\Delta M_{\mathrm{B}^0_{\mathrm{s}}}\right)/\mathrm{R}\left(\Delta M_{\mathrm{B}^0_{\mathrm{d}}}\right)$	[80]/[23, 29, 88]	$1.00 \pm 0.01_{\mathrm{EXP}} \pm 0.13_{\mathrm{SM}}$
$\mathrm{R}(\Delta\epsilon_K)$	[36] /[29, 88]	$1.08 \pm 0.14_{\mathrm{EXP+TH}}$
$\Omega_c h^2$	[25]/[86]	$0.1120 \pm 0.0056 \pm 0.012_{\mathrm{SUSY}}$
σ_p^{SI}	[20]	$(m_{\tilde{\chi}^0_1}, \sigma_p^{\mathrm{SI}})$ plane
jets + $E_{\mathrm{T}}^{\mathrm{miss}}$	[7]	$(m_0, m_{1/2})$ plane
$H/A, H^\pm$	[42]	$(m_A, \tan\beta)$ plane

Table 5.2: List of experimental constraints used in this work, including experimental and (where applicable) theoretical errors. The theoretical uncertainties in the interpretations of one-sided experimental limits are indicated by [...]. All constraints excluding the bottom three marked with "plane" in the final column are implemented as described in equation (5.3) *note: $R(x)$ is used to denote $x^{\mathrm{EXP}}/x^{\mathrm{SM}}$*

function to represent this,

$$\chi^2(\text{SUSY search limits}) \tag{5.11}$$

5.2.3 LEP Higgs searches

Direct searches for the light neutral Higgs boson from LEP [24, 105] already impose strong limits on constrained minimal SUSY models, requiring for cMSSM-like models that

$$m_{\mathrm{h}^0} > 114.4\mathrm{GeV}/c^2 \text{ at } 95\% \text{ CL.} \tag{5.12}$$

In other models in the MSSM this bound can be significantly lower due to more Higgs decay modes being available or reduced Higgs di-boson couplings [105], however models with these properties are not considered here.

The contribution to the χ^2 function can then be reconstructed from the χ^2 distribution of the measurement given in [24], and represented in the global χ^2 function by the term

$$\chi^2_{\mathrm{LEP}}\left(m_{\mathrm{h}^0}\right) \tag{5.13}$$

5.2.4 Pre-lhc state of models

The global χ^2 function, equation (5.8), is applied, per point, to the parameter space scan of the models discussed in Section 2.4. In all presented parameter space plots, while a full scan is carried out, a global cut of $\Delta\chi^2 < 45$ with respect to the minimum is applied to the sample to allow for efficient processing. The regions that have been excluded by this cut are coloured white in the figures. Also it should be noted that the final $\Delta\chi^2$ bin is inclusive $9 \leq \Delta\chi^2 \leq 45$.

In both models considered, the NUHM1 and the cMSSM, the χ^2 function is steep near the global minimum. Figure 5.1 shows the $\left(m_0, m_{1/2}\right)$ parameter-space for both models,

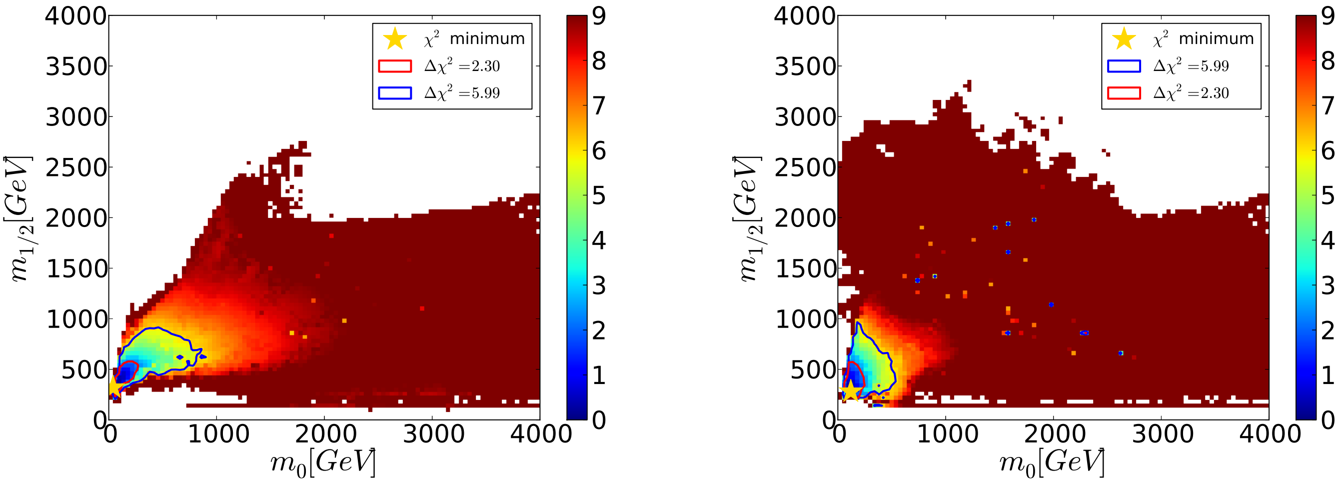

(a) cMSSM (b) NUHM1

Figure 5.1: The 2-D χ^2 parameter space for $(m_0, m_{1/2})$ for the (a) cMSSM and (b) NUHM1 in the pre-LHC regime

with the color scale denoting $\Delta\chi^2$ with respect to the minimum, and demonstrates the strong preference of these models for lower mass scales. In particular in the case of the NUHM1 (Figure 5.1b) m_0 is near to the lowest allowed value while maintaining a neutralino LSP. The strong preference for low masses is mostly driven by the $(g_\mu - 2)$ constraint which has a functional form[114],

$$(g_\mu - 2) \sim \frac{\tan\beta}{M^2_{\mathrm{SUSY}}}. \tag{5.14}$$

where M^2_{SUSY} is the mass scale of the lightest stop.

As the model moves to higher masses, SUSY begins to decouple and the value of $(g_\mu - 2)$ is returned to the SM value which has a 3σ deviation from the experimental value (see Table 5.2.

In the case of the NUHM1 there is a marginally deeper minimum, due to the ability to tune the sparticle spectrum further through the extra free parameter $m_{H_{u,d}}$. If one were to artificially remove points from the NUHM1 sample with $\chi^2_{\mathrm{NUHM1}} < \min(\chi^2_{\mathrm{CMSSM}})$ the shape and approximate extent in $(m_0, m_{1/2})$ of the cMSSM 68% CL and 95% CL

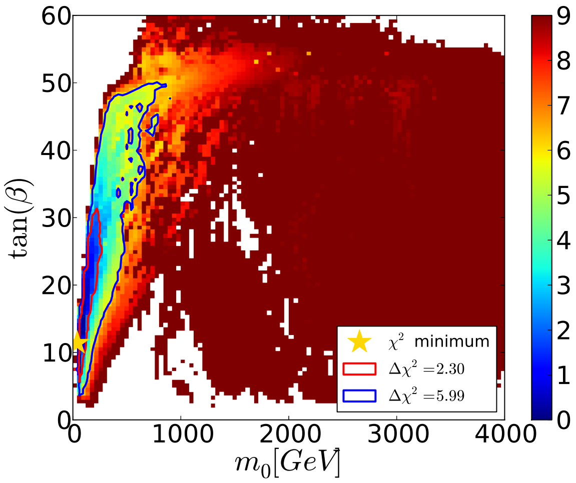

(a) cMSSM

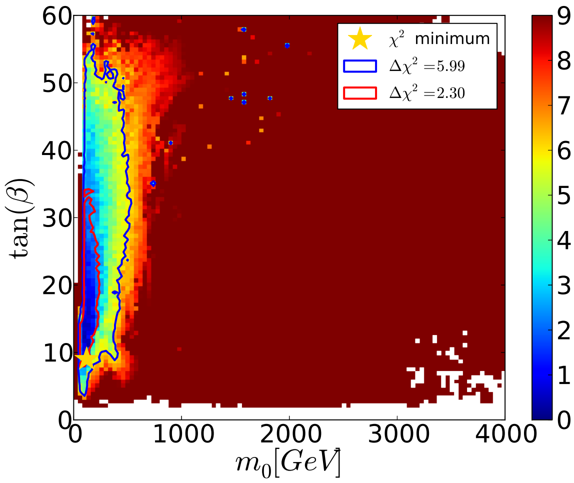

(b) NUHM1

Figure 5.2: The 2-D χ^2 parameter space for $(m_0, \tan\beta)$ for the (a) cMSSM and (b) NUHM1 in the pre-LHC regime

contours would be recovered[34].

An important feature evident in Figure 5.1 is the disfavored but present fixed $m_{1/2} \sim$ 100GeV line. This is what is known as the light higgs funnel, where the $m_{\mathrm{h}^0} \simeq 2 \times m_{\tilde{\chi}_1^0}$ and the resulting rapid annihilation is what allows this region of the model to satisfy the constraint on the relic abundance of dark matter, $\Omega_c h_c^2$[55]. In the NUHM1 a small region of this enters into the 95% CL region between $300 \lesssim m_0 \lesssim 400$GeV.

Figure 5.2 and Figure 5.3 show the $(m_0, \tan\beta)$ and $\left(\tan\beta, m_{1/2}\right)$ planes respectively. In both the cMSSM and NUHM1 we see that at higher values of $\tan\beta$ (≥ 40) higher masses start to become allowed, though still outside the 95% CL region. This is, again, due to the impact of $\left(g_\mu - 2\right)$, equation (5.14), where significant increases in $\tan\beta$ can be accounted for by increases in the mass scale.

In the NUHM1 access to lower values of m_0 is present due to the decoupling of the non-universal mass parameters from m_0. For a fixed value of $\tan\beta$ in the NUHM1 the value of m_0 can be reduced while increasing $m_{H_{1,2}}$ effectively keeping M_{SUSY} constant. This extra freedom only applies to m_0 as evidenced by the near identical shapes of the 68% CL and 95% CL contours in Figure 5.3a and Figure 5.3b.

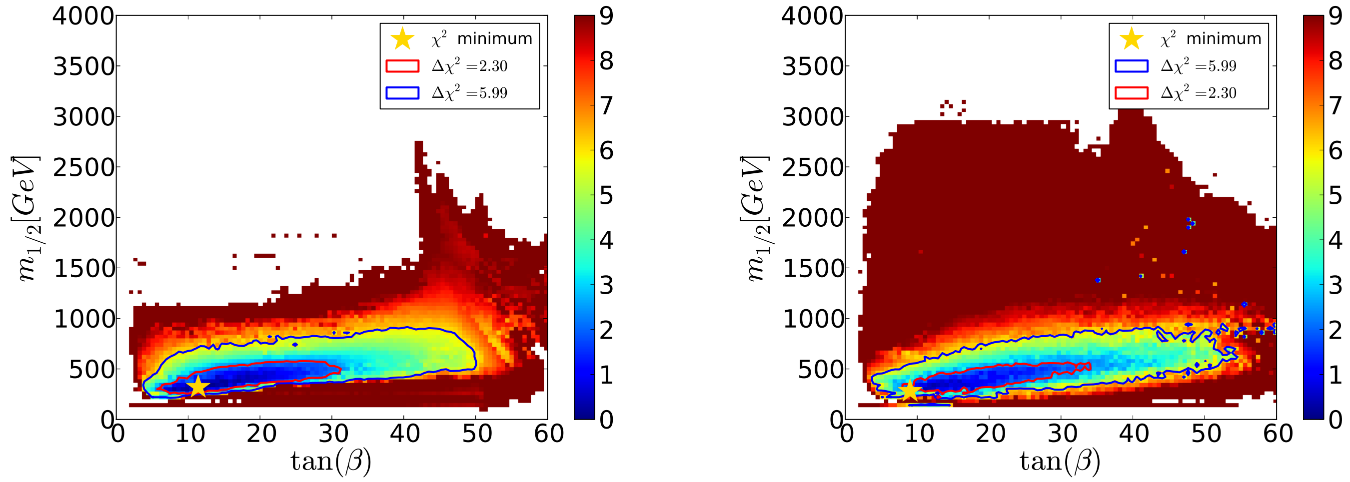

(a) cMSSM

(b) NUHM1

Figure 5.3: The 2-D χ^2 parameter space for $(\tan\beta, m_{1/2})$ for the (a) cMSSM and (b) NUHM1 in the pre-LHC regime

The low mass-scales preferred in the pre-LHC era are a large part of what led to the cMSSM model being selected as the benchmark model for direct searches for SUSY (e.g. similar to those presented in Chapter 4). A combination of low-mass and a stable LSP leads to a strong $E_{\mathrm{T}}^{\mathrm{miss}}$ signal, and the model provides a sufficiently broad parameter space to include a wide range of BSM signals.

Figure 5.4 shows the $(m_{\mathrm{A}}, \tan\beta)$ parameter spaces for both models. The main difference between the two models, is the preference for higher masses in the cMSSM. Again, this comes from being able to adjust the extra mass parameter, $m_{H_{1,2}}$, in the NUHM1.

Figure 5.5 shows the $\left(m_{\tilde{\chi}_1^0}, \sigma_p^{\mathrm{SI}}\right)$ parameter space. The apparent *smearing* here comes from the error on the calculation of σ_p^{SI}. For a fixed set of inputs $\{m_0, m_{1/2}, A_0, \tan\beta\}$ σ_p^{SI} and $\sigma(\sigma_p^{\mathrm{SI}})$ are calculated, this is covered in more detail in Section 5.3.3. However, for any value of $\sigma(\sigma_p^{\mathrm{SI}})$ of similar order to σ_p^{SI} one should expect a strong visible downward smearing due to the log-scale.

Also present in Figure 5.5b is the light higgs funnel at $m_{\tilde{\chi}_1^0} \sim 60\mathrm{GeV}$ contained within an island in the 95% CL region.

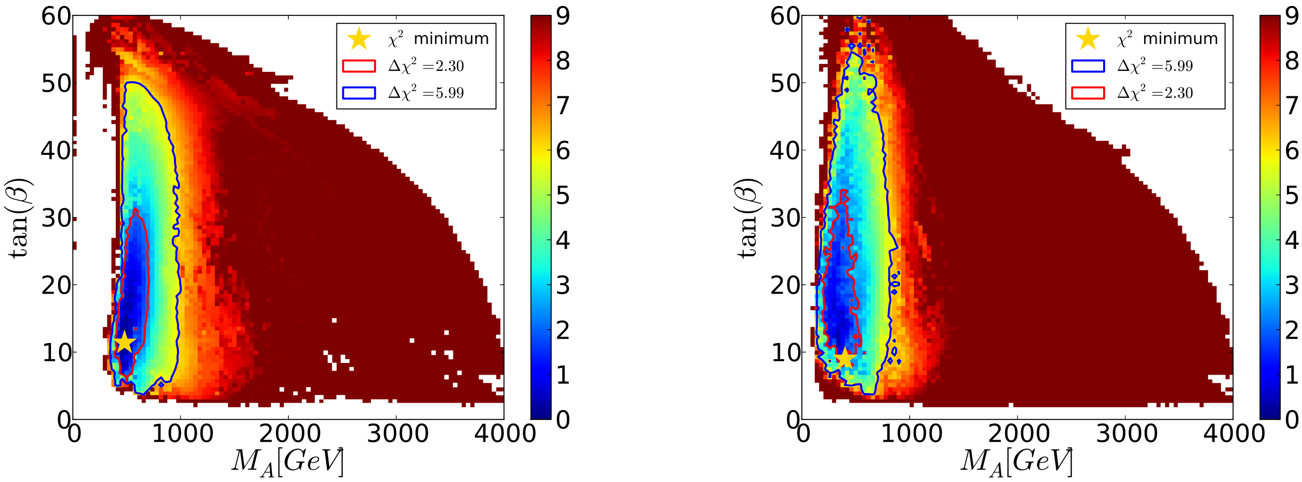

(a) cMSSM (b) NUHM1

Figure 5.4: The 2-D χ^2 parameter space for $\left(m_{\mathrm{A}}, \tan\beta\right)$ for the (a) cMSSM and (b) NUHM1 in the pre-LHC regime

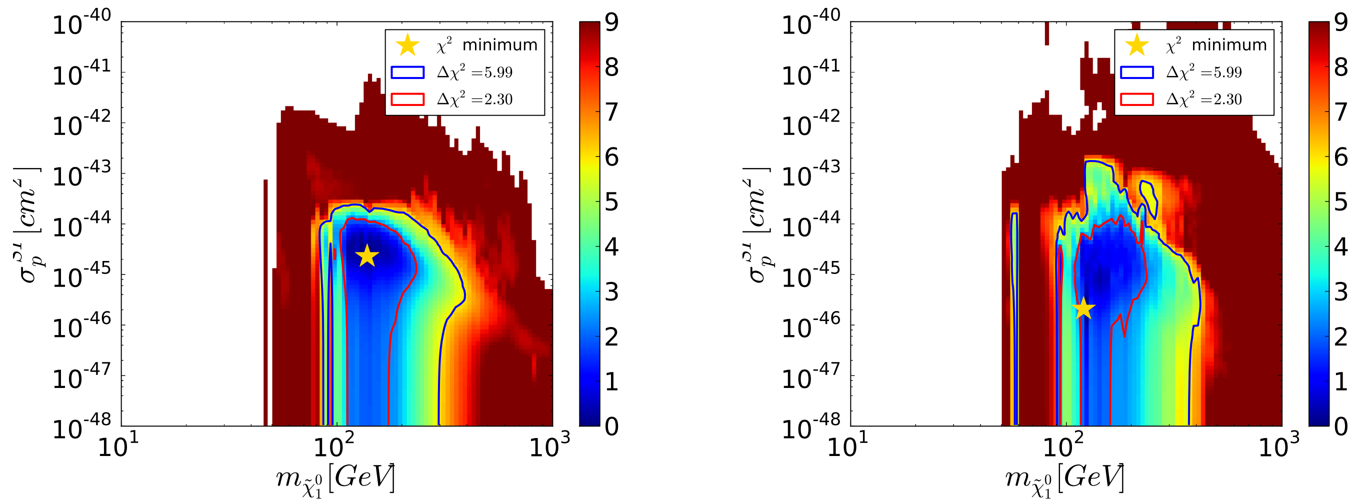

(a) cMSSM (b) NUHM1

Figure 5.5: The 2-D χ^2 parameter space for $\left(m_{\tilde{\chi}_1^0}, \sigma_p^{\mathrm{SI}}\right)$ for the (a) cMSSM and (b) NUHM1 in the pre-LHC regime

In summary, before the LHC era, fits in both the cMSSM and NUHM1 demonstrate a preference for low mass scales, mostly driven by the $\left(g_\mu - 2\right)$ constraint. Both models have well defined 68% CL and 95% CL regions and steep minima. They provide good discovery prospects for direct $E_{\mathrm{T}}^{\mathrm{miss}}$ direct searches, as well as direct higgs searches (e.g. via decays $\mathrm{H} \to \tau\tau$). At this stage there is little to no impact on the parameter space from B-physics constraints, for example $\mathrm{BR}\big(\mathrm{B}_{\mathrm{s}}^{0} \to \mu\mu\big)$, nor from precision electroweak measurements. A break down of the values of the minima and the main contributions can be found in Table 5.3 and Table 5.4 respectively, and these will be discussed in more detail in Section 5.4

5.3 Constraints from the LHC era

The direct searches for SUSY carried out the LHC, such as those described in Chapter 4, significantly increase our reach into the mass scale parameters of the models scanned. Not only this, but the combination of precision and luminosity at the LHC has enabled the probing of the rate of rare decay processes to an order of magnitude more than previously possible, the constraints from which impact the other parameters of the models.

It is possible to modify the χ^2 function described in equation (5.8) to include terms describing the impact of the various searches carried out thus far;

$$\begin{aligned}
\chi^2 = & \sum_i^N \frac{(C_i - P_i)^2}{\sigma(C_i)^2 + \sigma(P_i)^2} \\
& + \sum_i^M \frac{\left(f_{\mathrm{SM}_i}^{\mathrm{obs}} - f_{\mathrm{SM}_i}^{\mathrm{SUSY}}\right)^2}{\sigma\left(f_{\mathrm{SM}_i}\right)^2} \\
& + \chi^2(\text{SUSY search limits}) \\
& + \chi^2_{\mathrm{LEP}}\left(m_{\mathrm{h}^0}\right) \\
& + \chi^2(\text{Direct Searches}) && (5.15) \\
& + \chi^2\left(\mathrm{BR}\left(\mathrm{B}_s^0 \to \mu\mu\right)\right) && (5.16) \\
& + \chi^2(\mathrm{H} \to \tau\tau) && (5.17) \\
& + \chi^2\left(\mathcal{G}\left(m_{\mathrm{h}^0}\right)\right) && (5.18) \\
& + \chi^2\left(m_{\tilde{\chi}_1^0},\ \sigma_p^{\mathrm{SI}}\right). && (5.19)
\end{aligned}$$

The impact of direct searches performed at CMS and ATLAS[4] is contained in the term 5.15 and is described in detail in Section 5.3.1. The combined results of searches for the rare decay $\mathrm{B}_s^0 \to \mu\mu$ are described in the 5.16 term, and the details on the combination as well as the χ^2 function are given in Section 5.3.2. The impact of searches for the decay of heavy Higgs particles through the process $\mathrm{H} \to \tau\tau$, at CMS, are discussed in Section 5.3.2 and included in the term 5.17. Also included is the impact of the reported observation of an SM-like Higgs boson with $m_{h^0} \sim 126\mathrm{GeV}$ discussed in Section 5.3.2 and described by the term 5.18. Finally term 5.19 is inserted to take account of the impact of direct searches for dark matter which put constraints on the mass of the LSP as well as its scattering cross-section with protons. This term is detailed in Section 5.3.3.

5.3.1 Direct searches at the LHC

Direct searches, such as the one discussed in Chapter 4, have the greatest impact on the mass scale parameters of a model. In the case of the search being a combined $E_{\mathrm{T}}^{\mathrm{miss}}$ and leptonic search a degree of sensitivity to the value of $\tan\beta$ is introduced to the limit.

[4] In the analysis presented here a single result from ATLAS is considered

However, for $E_{\mathrm{T}}^{\mathrm{miss}}$ only searches the dependence on $\tan\beta$ is negligible [84].

Multiple methods can be used to construct an approximation of the likelihood function reported by an experiment. The choice of these methods is governed by the amount of information provided by the authors.

In the case of the authors providing a single exclusion contour in the $\left(m_0, m_{1/2}\right)$ plane and reporting the value of their expected and observed number of events, an attempt is made to reconstruct the likelihood function beyond the range of the reported contour. This approach follows [111] in which an estimate is made of the required integrated luminosity, $\mathcal{L}$, for discovery of sparticles of varying masses. The relationship, determined empirically, is

$$\mathcal{M} \propto \mathcal{L}^{1/4}, \tag{5.20}$$

where $\mathcal{M}$ denotes a radial parameter formed of the squark and gluino masses e.g. $\mathcal{M}^2 \sim m_0^2 + m_{1/2}^2$. This implies for radial lines in the m_0 ,$m_{1/2}$ plane the effective event rate scales as $\mathcal{M}^{-4}$. This relationship means it is possible to estimate the effective number of events for the scanned points in the $\left(m_0, m_{1/2}\right)$ plane and, using the reported number of events, assign a χ^2 penalty. It is also possible to take account of any excess observed, i.e. an observation for which the SM should receive a penalty. A second term in the χ^2 function function is therefore provided to allow for a χ^2 penalty at large masses when SUSY decouples,

$$\begin{aligned}
\chi^2 =& \left(\frac{M_{\mathrm{C}}}{M_{\mathrm{point}}}\right)^4, \textit{No excess} \\
\chi^2 =& \chi^2_\infty \left|\frac{M_{\mathrm{C}}}{M_{\mathrm{point}}} - 1\right|^4, \textit{Excess}
\end{aligned} \tag{5.21}$$

where $M^2_{\mathrm{point}} = m_0^2 + m_{1/2}^2$ and M_{C} is chosen to ensure the χ^2 penalty at the experimental contour corresponds to the two-dimensional χ^2 value for the percentage Confidence Level (CL) exclusion at the contour and χ^2_∞ is the χ^2 penalty associated with the excess observed (if any).

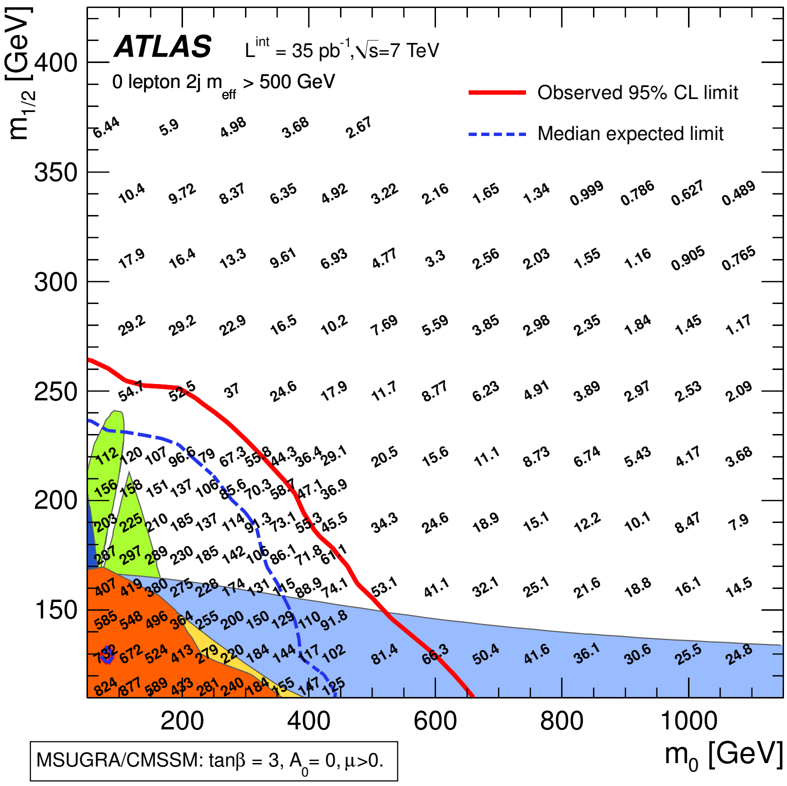

Figure 5.6: An illustrative plot of a variably binned grid of event numbers in the $(m_0, m_{1/2})$ plane used to partially reconstruct the likelihood[6]

When multiple contours are provided, for example the observed 95% CL and 68% CL, it is possible to improve the approximation by perofmring a fit for the exponent in equation (5.21).

Previously other results [6] have provided a grid of effective event numbers for the sensitive regions in the $(m_0, m_{1/2})$ plane. An illustrative example of such a grid is given in Figure 5.6. In this case a contour is constructed spanning the outer edge of the gridded region. Any point lying on the outside of this region is handled by the method described above using the contour inscribing the gridded region. Any point lying in the grid has an effective event number calculated by interpolating between the nearest three grid entries.

In most cases results are published with several limiting constraints, beyond the amount of data provided, such as providing exclusion contours in the context of only the cMSSM where $A_0 = 0$ and $\tan\beta = 10$ and where a limited range of m_0 and $m_{1/2}$ values are used. In these cases it is important to complete steps to validate the insensitivity of these results to A_0 and $\tan\beta$ as well as their relevance to the NUHM1. Also, in the cases of results presented in the $(m_0, m_{1/2})$ plane it is common for the exclusions contour(s) to extend only to some value[5] of $m_{0\text{min}} > 0$, and so it is necessary to validate the behavior of these contours for lower values of m_0 that may be accessible in the NUHM1. To achieve these validation steps a generic detector simulation, `Delphes` [97], is used and loaded with a "card" that provides performance similar to either CMS or ATLAS. This is then used in general to verify the $\mathcal{M}^{-4}$ scaling law used (see equation (5.21)), and specifically to recreate the CL values for each of the contours provided. Figure 5.7 shows the results of this validation procedure for the $\mathcal{M}^{-4}$ scaling law. Along side this simulations are run to verify that the results display insensitivity to A_0 and $\tan\beta$ as well as test the sensitivity of the results to the non-universality parameter in the NUHM1. The searches implemented here demonstrate insensitivity to the non-universality parameter as well as A_0 and $\tan\beta$ [35].

`Delphes` simulations can further be made use of to extend the range in m_0 for exclusion contours provided in the cMSSM such that they can be applied for the lower values accessible in the NUHM1. In all cases tested so far the behavior at low m_0 is independent of the value of $m_{1/2}$.

Here the ATLAS jets + $E_{\mathrm{T}}^{\mathrm{miss}}$ search using 5fb^{-1} of data at 7TeV is implemented [8].

5.3.2 Other searches at the LHC

Other searches for BSM physics have been performed at the LHC. These include searches by the dedicated B-physics experiment LHCb, constraints on $\mathrm{B}_s^0 \to \mu\mu$ from multiple experiments and both searches for heavy Higgs and for the light Higgs from CMS and ATLAS. For each of these a term can be constructed to add to the global χ^2 function in conjunction with the direct searches described above.

[5]The value at which the neutralino is no longer the LSP, see Section 2.4.1

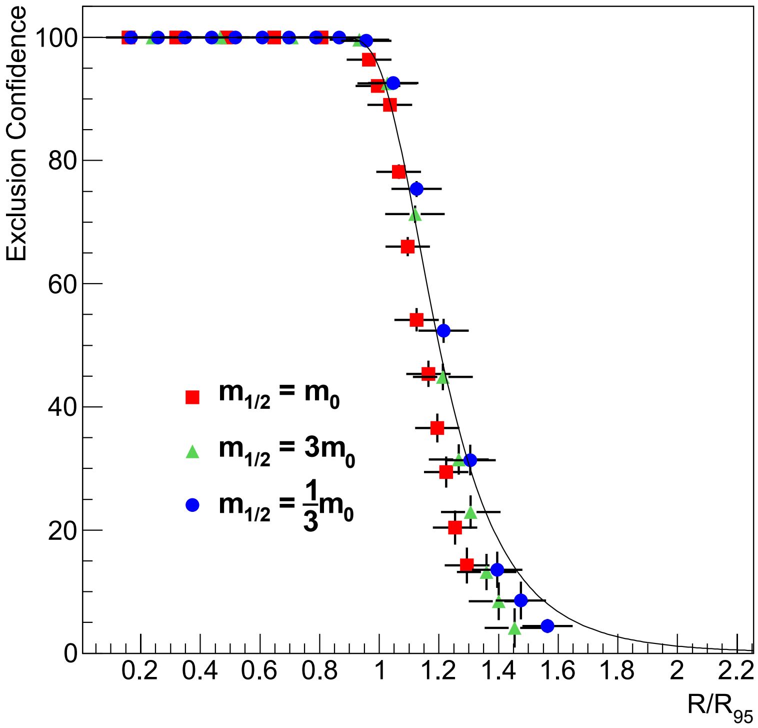

Figure 5.7: Confidence levels for a selection of cMSSM points with $\tan\beta = 10, A_0 = 0$ with varying values of $R \equiv \mathcal{M}/\mathcal{M}_0$, where $\mathcal{M}_0$ is the value of $\mathcal{M}$ at the point on the 95% CL exclusion line with the same ratio of $m_0/m_{1/2}$. The red squares, blue circles and green triangles are taken from rays in the $\left(m_0, m_{1/2}\right)$ with $m_0/m_{1/2} = 1/3, 1, 3$ respectively. The solid line is the % CL value calculated assuming that the number of signal events scale as $\mathcal{M}^{-4}$[35]

CMS and ATLAS: $\mathbf{B_s^0 \to \mu\mu}$

The decay $B_s^0 \to \mu\mu$ is a particularly rare decay for which the branching ratio predicted in the SM is well known[37]. Any deviation from this value would indicate the presence of interference from diagrams originating from non-SM particles. In the case of SUSY the diagrams in Figure 5.8 contribute, indicating that $\mathrm{BR}\big(B_s^0 \to \mu\mu\big)$ is particularly sensitive to the presence of charged and neutral Higgs particles.

While CMS is not designed as a B-physics specific experiment there are several design and operational aspects that allow a competitive measurement of $\mathrm{BR}\big(B_s^0 \to \mu\mu\big)$. These include a high tracking resolution, the hermeticitie of the detector itself, and the ability to reconstruct and match tracks to a large number of primary vertexes. This last point is particularly important as the offline tagging of jets with displaced secondary vertexes allows discrimination between heavy and light flavour jets, and the ability to deal with large number of primary vertexes enables CMS to cope with pile-up effects and thus achieve a high integrated luminosity.

The most recent of these results [108] reports an upper limit of $\mathrm{BR}\big(B_s^0 \to \mu\mu\big) < 7.7\times10^{-9}$ at 95% CL

The ATLAS experiment also released results of a search for the $B_s^0 \to \mu\mu$ decay[9] quoting their limits as $\mathrm{BR}\big(B_s^0 \to \mu\mu\big) < 2.2(1.9) \times 10^{-8}$ at 95% CL (90% CL).

Finally, the CDF experiment also publish searches for $B_s^0 \to \mu\mu$, citing a value $\mathrm{BR}\big(B_s^0 \to \mu\mu\big) < 3.1(1.0) \times 10^{-8}$ at 95% CL (90% CL)[45].

LHCb: $\mathbf{B_s^0 \to \mu\mu}$

The LHCb experiment recently published the first evidence for the $B_s^0 \to \mu\mu$ decay and consequently the first measurement of the branching ratio $\mathrm{BR}\big(B_s^0 \to \mu\mu\big)$ [11]. They report an excess of events in the B_s^0 search window with a significance of 3.5σ and subsequently perform a fit producing a result $\mathrm{BR}\big(B_s^0 \to \mu\mu\big) = \big(3.2^{+1.5}_{-1.2}\big) \times 10^{-9}$. This is consistent with the SM expectation of $(3.23 \pm 0.27) \times 10^{-9}$ [37].

Combination: $B_s^0 \to \mu\mu$

Making use of the signal and background expectations provided in [11], [108], [9], and [45] toy experiments were generated to recreate the quoted measurement and constraints respectively. The χ^2 functions derived from this method can then be combined and used to estimate the impact and behavior of the combination of these constraints for any value of $\mathrm{BR}\big(\mathrm{B_s^0} \to \mu\mu\big)$. Again this gets added to the global χ^2 function as a term denoted

$$\chi^2 = \chi^2\big(\mathrm{BR}\big(\mathrm{B_s^0} \to \mu\mu\big)\big) \tag{5.22}$$

The probability distribution and log-likelihood function for this combination can be seen in Figure 5.9.

There is an important distinction between the value of $\mathrm{BR}\big(\mathrm{B_s^0} \to \mu\mu\big)$ measured by experiment and that calculated for the SM by theoretical means. In the case of experiment, the Time Averaged (TA) value is measured, denoted $\mathrm{BR_{SM,TA}}$, which is not equal to the theoretically calculated value $\mathrm{BR_{SM,TH}}$ due to the difference in lifetimes between the heavier and lighter $\mathrm{B_s^0}$ mesons. We can translate between $\mathrm{BR_{SM,TA}}$ and $\mathrm{BR_{SM,TH}}$ using the relationship[51]

$$\mathrm{BR}\big(\mathrm{B_s^0} \to \mu\mu\big)_{\mathrm{SM,TH}} = \frac{1 - y_s^2}{1 + \mathcal{A}_{\Delta\Gamma} y_s} \times \mathrm{BR}\big(\mathrm{B_s^0} \to \mu\mu\big)_{\mathrm{TA}} \tag{5.23}$$

where $\Delta\Gamma \equiv \Gamma_{\mathrm{L}}^{(s)} - \Gamma_{\mathrm{H}}^{(s)}$; Γ is the decay width and L and H denote the light and heavy mass eigenstates of the $\mathrm{B_s^0}$; $y_s \equiv \frac{\Delta\Gamma_s}{2\Gamma_s}$ and Γ_s is the average decay width of the two mass eigenstates and $\mathcal{A}_{\Delta\Gamma} \equiv \frac{R_{\mathrm{H}} - R_{\mathrm{L}}}{R_{\mathrm{H}} + R_{\mathrm{L}}}$ where the R values are decay coefficients for the two mass eigenstates. In the SM $\mathcal{A}_{\Delta\Gamma} = 1$ and $y_s = 0.088 \pm 0.014$.

Given $\mathrm{BR}\big(\mathrm{B_s^0} \to \mu\mu\big)_{\mathrm{SM,TH}} = (3.2 \pm 0.2) \times 10^{-9}$ we have,

$$\mathrm{BR}\big(\mathrm{B_s^0} \to \mu\mu\big)_{\mathrm{SM,TA}} = \frac{\mathrm{BR}\big(\mathrm{B_s^0} \to \mu\mu\big)_{\mathrm{SM,TH}}}{1 - y_s} = (3.5 \pm 0.2) \times 10^{-9} \tag{5.24}$$

Using this translation we can then accurately compare calculated ratios with the SM value and the experimental results.

CMS: $\mathrm{H} \to \tau\tau$

Searches for a heavy Higgs boson have been carried out at CMS[42] and ATLAS[10]. For the most recent results the search from CMS appears to have the higher degree of sensitivity (see [42] Figure 4 and [10] Figure 4(d)), and so is selected to be the representative constraint applied to the parameter spaces.

Results for heavy Higgs searches are usually presented in two planes, a single contour in the $\left(m_{\mathrm{A}}, \tan\beta\right)$ plane and multiple contours in the $\left(m_{\mathrm{H}}, \sigma \times \mathrm{BR}\right)$ plane. The scan used does not include the value of $(\sigma \times \mathrm{BR})$ for each point, however the relationship

$$(\sigma \times \mathrm{BR}) \propto \tan^2\beta, \tag{5.25}$$

allows the translation of the parameter of the likelihood function into the $\left(m_{\mathrm{A}}, \tan\beta\right)$ plane. This relationship has been checked by evaluating $\sigma \times \mathrm{BR}$ for a representative grid of points[6] in the models considered by using the SM result for $\sigma\left(\mathrm{b}\overline{\mathrm{b}} \to \mathrm{H}_{\mathrm{SM}}\right)$[75] modified by the effective couplings calculated in `FeynHiggs` which are then also used to calculate $\mathrm{BR}(\mathrm{H} \to \tau\tau)$ (including a factor two to take into account the production of the CP-even H and the CP-odd A boson as these have approximately the same production cross-section and decay widths). On top of this it should be noted that the region in which this approximation begins to break down, at higher value of m_{A} and $\tan\beta$, is out of the range of the impact of the search considered here[34] hence this approximation is valid and verified for all regions important to the analysis presented here.

Assuming the χ^2 function takes the form

$$\chi^2 = A(\sigma \times \mathrm{BR})^{p\left(m_{\mathrm{H}}\right)} \tag{5.26}$$

where $p\left(m_{\mathrm{H}}\right)$ is a function of m_{H} where each value is determined by fitting equation (5.26)

[6] Comparing Figure 3 in [42] with the pre-LHC $\left(m_{\mathrm{A}}, \tan\beta\right)$ plane, Figure 5.4, it is apparent that the region of highest impact is for $m_{\mathrm{A}} \sim 400$ and large $\tan\beta$, it is for this region that a grid of points were evaluated

through the contours provided in $\left(m_{\mathrm{H}}, \sigma \times \mathrm{BR}\right)$ space for a given fixed m_{H}, and A is chosen to normalize the function to the χ^2 value associated with the CL value at each exclusion curve provided.

Using equation (5.25) we can replace $(\sigma \times \mathrm{BR})$ in equation (5.26) giving

$$\chi^2 = \chi^2_{\text{contour}} \left(\frac{\tan^2 \beta}{\tan^2 \beta_{\text{contour}}} \right)^{p\left(m_{\mathrm{H}}\right)} \tag{5.27}$$

where A has been replaced with χ^2_{contour} to make the χ^2 boundary condition on the single $\left(m_{\mathrm{A}}, \tan \beta\right)$ plane more clear.

CMS: SM-like Higgs search

In November 2012 both the CMS and ATLAS collaborations reported observations consistent with a SM-like Higgs boson with a mass of 126 GeV/c^2. As discussed in Section 2.2 minimal models of SUSY can support a light SM like Higgs (h^0) in the mass range $85 < m_{\mathrm{h}^0} < 135\mathrm{GeV}/c^2$ and so an observation of $m_{\mathrm{h}^0} = 125\mathrm{GeV}/c^2$ is entirely consistent. However, the nature of the measurement may significantly constrain the viable regions of parameter space for the models considered.

This measurement can be accommodated in the global χ^2 function with a Gaussian term $\mathcal{G}(\mu, \sigma)$,

$$\chi^2 = \mathcal{G}\left(\mu = 125, \sigma^{\exp} = 1.0\mathrm{GeV}, \sigma^{\text{theo}} = 1.5\right) \tag{5.28}$$

5.3.3 Dark Matter

As discussed in Section 2.2 one of the benefits of R-parity conserving SUSY is that it provides a natural dark matter candidate in the form of a stable LSP, the neutralino $\widetilde{\chi}^0_1$. Both direct constraints on the mass of the neutralino and its interactions as well as cosmological constraints can be placed on the parameter space of models of supersymmetry.

Analysis of the Cosmic Microwave Background (CMB), such as in [113], yields measurements of the parameters of a Λ CDM (LCDM) model of the universe [113]. These parameters include $\Omega_c h^2$, the relic density of cold dark matter in the universe, which can be calculated for each model and added to the global function as a term in equation (5.3).

Direct searches for DM interactions provide constraints parameterized by the mass of the LSP ($m_{\tilde{\chi}_1^0}$) and the spin-independent scattering cross-section of protons with the LSP (σ_p^{SI}). The current most sensitive of these comes from the Xenon experiment [21]. These can be added to the global χ^2 function via a term,

$$\chi^2_{\sigma_p^{\mathrm{SI}}} = \chi^2\Big(m_{\tilde{\chi}_1^0},\ \sigma_p^{\mathrm{SI}}\Big), \tag{5.29}$$

Assuming that a search produces an observation of n_{obs} events, with an expectation of $\mu \pm \sigma$, it is possible to construct a Gaussian likelihood $L(\mu' \pm \sigma')$ using a $\mathrm{CL_s}$ calculator[7] and therefore calculate the 90% CL upper limit on the number of events, $n_{p=0.9}$.

The χ^2 value for any particular point can then be calculated by finding the value of σ_p^{SI}, corresponding to a particular $m_{\tilde{\chi}_1^0}$, of the point, for which the measurement reports an exclusion of ($p = 0.9$). Then assuming that,

$$\frac{n_{\mathrm{point}}}{n_{p=0.9}} = \frac{\sigma^p_{\mathrm{point}}}{\sigma^p_{pi=0.9}}, \tag{5.30}$$

the number of events expected at the point, n_{point}, can be calculated and the χ^2 calculated in the regular fashion,

$$\chi^2_{\sigma_p^{\mathrm{SI}}} = \left(\frac{n_{\mathrm{point}} - \mu'}{\sigma'}\right)^2 \tag{5.31}$$

There is some uncertainty in the calculation of σ_p^{SI} due to uncertainty in the value of the $\pi - N$ σ term. In this analysis a value of $\Sigma_{\pi N} = 50\mathrm{MeV}$ is used to account for the case where $\langle N|\, s\bar{s}\, |N\rangle = 0$ and hence $\Sigma_{\pi N} = \sigma_0 \sim 30\mathrm{MeV}$ while also allowing for higher

[7] Implemented in the previously mentioned `Delphes` framework

values that other analyses report[98].

In this case the results implemented are from 225 active days[21], where the collaboration report an observation of $n_{\mathrm{obs}} = 2$ events where they expected $n_{\mathrm{exp}} = 1.0 \pm 0.2$. They report a 90% CL upper limit of $\sigma_p^{\mathrm{SI}} < 2 \times 10^{-45}\mathrm{cm}^2$ for $m_{\tilde{\chi}_1^0} = 55\mathrm{GeV}$, as well as providing a 90% CL contour in $\left(m_{\tilde{\chi}_1^0}, \sigma_p^{\mathrm{SI}}\right)$ parameter space. Using the $\mathrm{CL_s}$ calculator a 90% CL upper limit on $n_{\mathrm{obs}} < 5.1$ is calculated, corresponding to a Gaussian distribution $\mathcal{G}(\mu = 1.0, \sigma = 2.7)$ where $\mu = 1$ is the mean excess $(n_{\mathrm{obs}} - n_{\mathrm{exp}})$ and $\sigma = 2.7$ is chosen to recreate the 90% CL upper limit. These values are then used in equation (5.31) to calculate a χ^2 punishment per point. However, for any particular point in the scan, the value of σ_p^{SI} is allowed to float within a Gaussian defined by the calculated value of σ_p^{SI} and $\sigma(\sigma_p^{\mathrm{SI}})$, that is the uncertainty on σ_p^{SI} coming from the calculation of σ_p^{SI} using $\Sigma_{\pi N}$ and translating the uncertainties through.

As in the case of the direct searches for SUSY the results presented for direct DM searches make some model specific assumptions, i.e. that the local DM density $\rho(\mathrm{DM}) \sim 0.3\mathrm{GeV/cm}^3$ as well as model specific assumptions about the DM velocity distributions. To account for this a fractional uncertainty on σ_p^{SI} of $\sqrt{2}$ is included, though the effect is negligible[35].

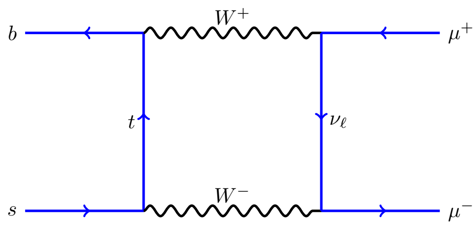

(a)

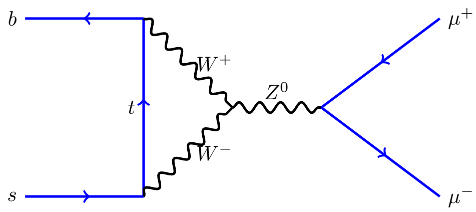

(b)

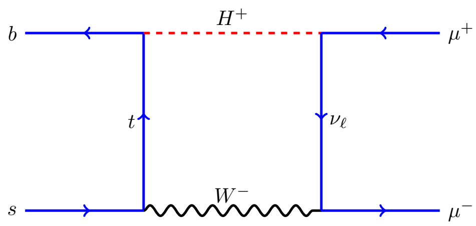

(c)

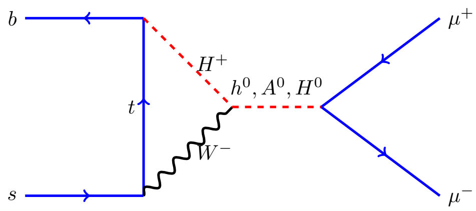

(d)

Figure 5.8: Examples of the (a), (c) box and (b), (d) electroweak penguin diagrams for the SM and SUSY respectively, that contribute to $\mathrm{BR}\left(\mathrm{B_s^0} \to \mu\mu\right)$

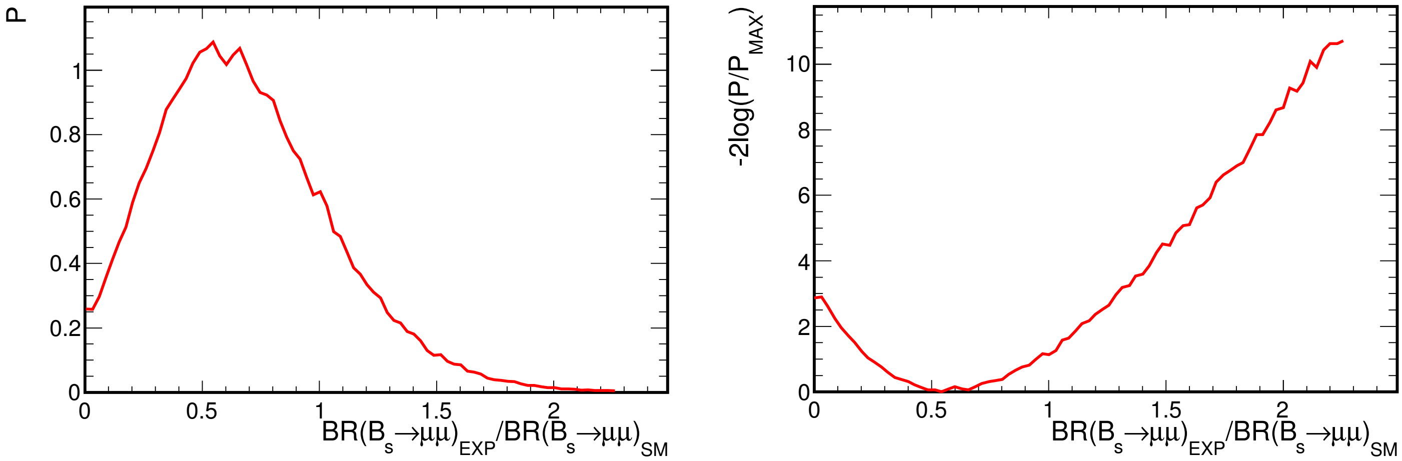

(a) Probability distribution

(b) Log-likelihood function

Figure 5.9: The (a) probability distribution and (b) log-likelihood function found in an unofficial combination of the constraints on $\mathrm{BR}\left(\mathrm{B}_s^0 \to \mu\mu\right)$ from ATLAS, CDF, CMS, and LHCb

	χ^2/n_d	$P(\chi^2, n_d)$	m_0	$m_{1/2}$	A_0	$\tan\beta$	$m_{H_{1,2}}$
cMSSM pre-LHC	21.9/20	0.35	75.93	350.53	84.67	11.80	N/A
cMSSM post-LHC	32.8/23	0.08	300.53	905.00	-1324	16.26	N/A
NUHM1 pre-LHC	19.9/18	0.34	130.37	301.09	-1176	9.50	-9.843×10^5
NUHM1 post-LHC	31.3/22	0.09	237.47	968.81	-1859	15.65	-6.5×10^6

Table 5.3: Listing of the best fit points for the cMSSM and NUHM1 models before and after applying LHC era constraints

	cMSSM pre-LHC	**cMSSM** post-LHC	**NUHM1** pre-LHC	**NUHM1** pre-LHC
$\mathrm{R(BR(b \to s\gamma))}$	1.19	1.19	0.21	0.18
$\mathrm{R(BR(B \to \tau\nu))}$	1.12	1.03	1.11	1.08
$\mathrm{BR}\big(\mathrm{B_s^0} \to \mu\mu\big)$	0	1.22	0	1.70
$a_\mu^{\mathrm{EXP}} - a_\mu^{\mathrm{SM}}$	1.06	8.48	0.43	7.82
m_{W}	0.47	1.50	0.34	1.54
$A_{\mathrm{fb}}(b)$	8.67	6.64	8.18	6.43
$A_\ell(\mathrm{SLD})$	2.20	3.51	2.47	3.68
σ^0_{had}	2.32	2.50	2.37	2.50
R_l	0.92	1.09	1.04	1.12
Direct Searches	-	-	1.73	1.18
DM Searches	-	-	0.12	0.13
$\mathrm{H} \to \tau\tau$	-	-	0.00	0.00

Table 5.4: Leading contributions to the χ^2 at the best-fit points in the cMSSM and NUHM1 before and after applying the LHC-era constraints

5.4 Impact on models from the LHC

It is useful to break down the impact of individual searches on the models as well as the overall impact of the combined post-LHC χ^2 function.

5.4.1 Parameter spaces

For each parameter space two sets of figures are shown in the subsequent sections. Firstly a global $\Delta\chi^2$ plot for each model is shown with the global minimum after application of the LHC-era constraints marked with a star, and the $\Delta\chi^2 \leq 2.3$ and $\Delta\chi^2 \leq 5.99$

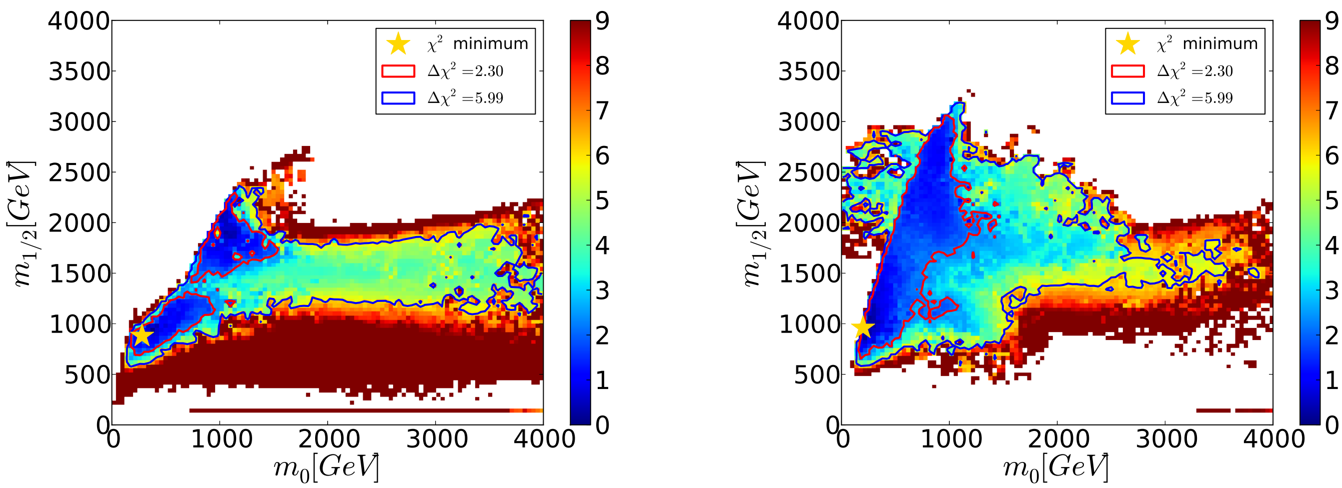

(a) cMSSM (b) NUHM1

Figure 5.10: The 2-D χ^2 parameter space for $(m_0, m_{1/2})$ for the (a) cMSSM and (b) NUHM1 in the post-LHC regime

contours shown in red and blue respectively. Secondly a comparison of the $\Delta\chi^2 = 2.3$ and $\Delta\chi^2 = 5.99$ contours between the pre-LHC and the post-LHC regimes is shown, with the former lines dotted, and the latter solid. These serve to clarify the impact of the LHC-era constraints.

$(\boldsymbol{m_0, m_{1/2}})$

In this plane we expect the main impact of the direct ATLAS jets + $E_{\mathrm{T}}^{\mathrm{miss}}$ search to be present. In both models we now see a rapid rise in χ^2 for values of $m_{1/2} < m_{1/2_{\mathrm{min}}}$. However the global behavior of the χ^2 function is relatively flat, with $100 < m_0 < 4000\mathrm{TeV}$ and $500 < m_{1/2} < 2500\mathrm{GeV}$ included within 95% CL in both models. Hence it should be noted that the overall structure is more important than the specific best-fit points.

Figure 5.10 shows the individual parameter spaces after application of the LHC-era constraints, and Figure 5.11 compares the 68% CL and 95% CL contours for before and after the application of the LHC-era constraints. In the cMSSM a bifurcation in the 68% CL region is now evident. This bifurcation arises due to the impact of the

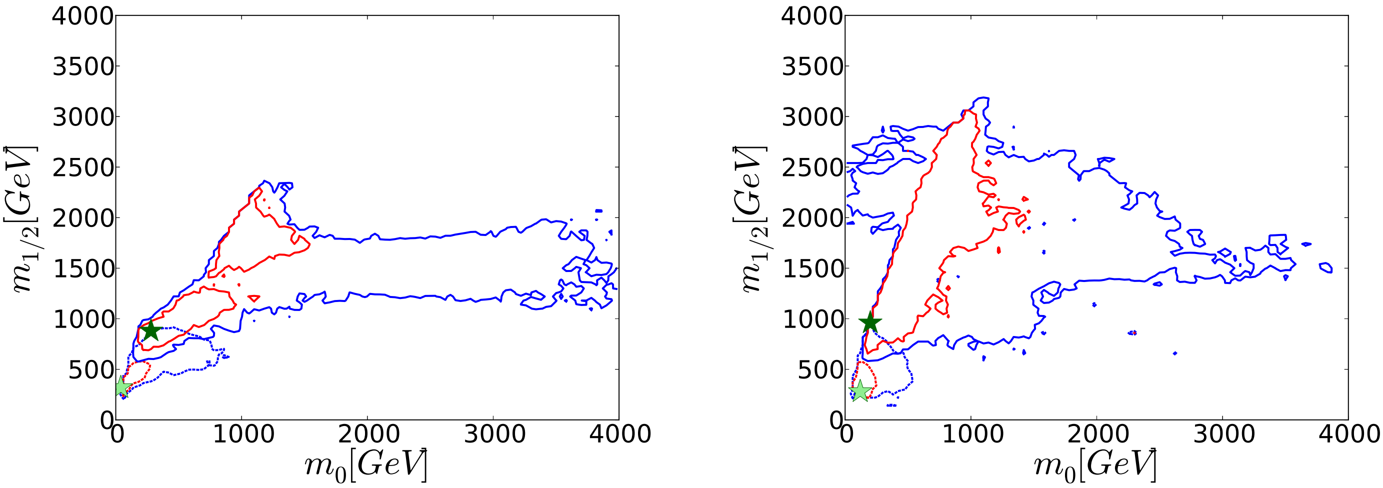

(a) cMSSM

(b) NUHM1

Figure 5.11: $(m_0, m_{1/2})$ parameter space comparing pre-LHC (dotted) and post-LHC (solid) 68% CL (red) and 95% CL (blue) regions for the (a) cMSSM and (b) NUHM1

dark matter relic density constraint. In the low mass island this is satisfied through $\widetilde{\tau}$-$\widetilde{\chi}^0$ co-annihilation, in the higher mass region, $(m_0, m_{1/2}) \sim (1000, 1700\text{GeV})$ the requisite relic density is achieved through a rapid annihilation funnel where $M_A \sim 2m_{\widetilde{\chi}^0}$. The bifurcation appears to a lesser extent in the NUHM1 because here the rapid annihilation funnel can appear at lower $m_{1/2}$ for the same m_0 as in the cMSSM because M_A can be tuned with the non-universality parameter. This also gives rise to the greater extent of the 68% CL contour in m_0 in the NUHM1 with respect to the cMSSM.

It should be noted that small islands are present between the two larger 68% CL islands in the cMSSM containing points with $\Delta\chi^2 < 2.3$ which indicates that it may be possible to reduce or even remove the visually bimodal nature of these contours with a more dense sampling in this region.

In the NUHM1 the 68% CL region is contained in a single contour, and the 95% CL region extends beyond the $\widetilde{\tau}$-$\widetilde{\chi}^0$ co-annihilation region, i.e. into very low m_0 for high $m_{1/2}$. In the cMSSM this region is excluded due to not having a neutralino LSP. In the NUHM1 a neutralino LSP can be maintained, and the constraint on the relic density can be satisfied through the combined effect of multiple neutralino and chargino

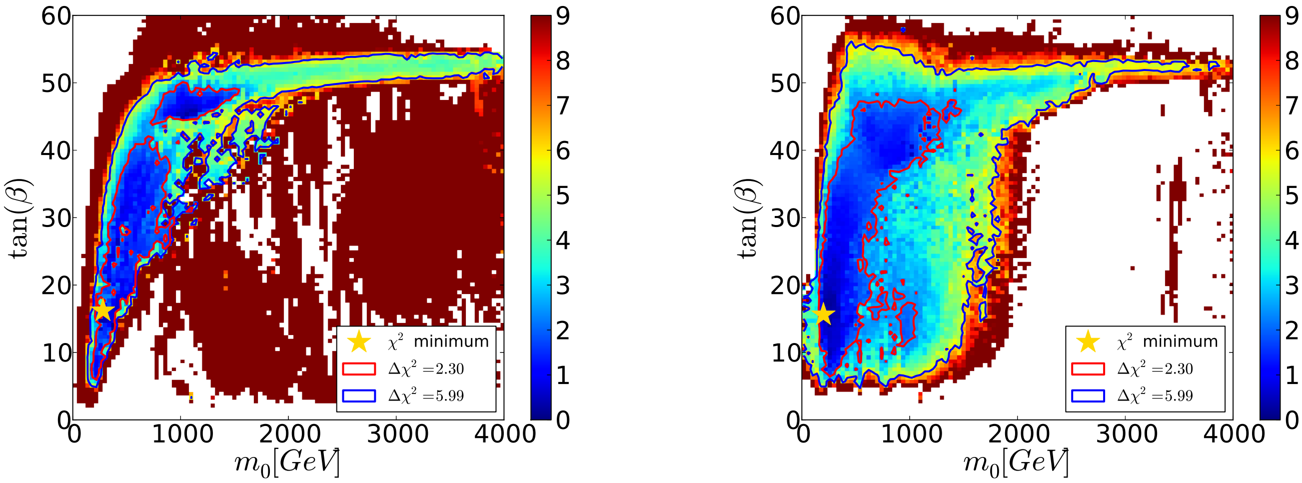

(a) cMSSM

(b) NUHM1

Figure 5.12: The 2-D χ^2 parameter space for $(m_0, \tan\beta)$ for the (a) cMSSM and (b) NUHM1 in the post-LHC regime

co-annihilation processes[35]. The existence of this region as being both valid by the presence of a neutralino LSP as well as satisfying the relic density constraints has been confirmed by testing a selection of the points with multiple public codes for dark matter calculations[8].

While in the cMSSM the 95% CL region appears to extend to higher m_0 (as it did in the pre-LHC results) this is due to the marginally higher minimum χ^2, as the NUHM1 shows a near identically shape in high m_0 χ^2 variation but with respect to a different minimum value.

The light higgs funnel is, while still disfavored, clearly present in the cMSSM for all $m_0 > 700$GeV, but is only visible in the NUHM1 for $m_0 > 3200$GeV.

The impact of the direct searches is then to push the models to much higher values of $m_{1/2}$ for intermediate m_0 ($\lesssim 1500$GeV), as shown in Table 5.3.

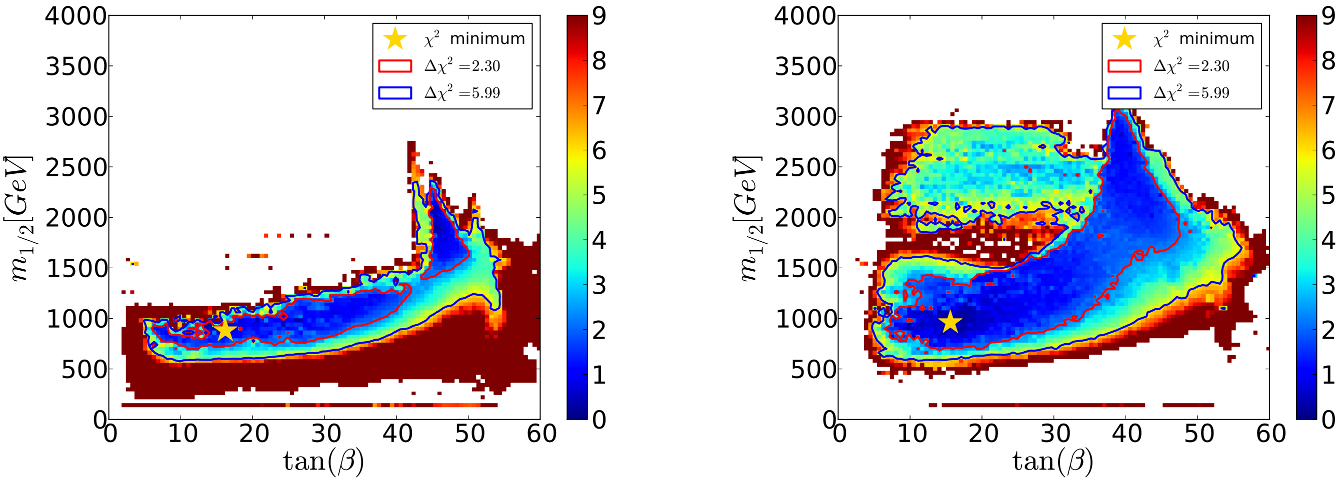

(a) cMSSM

(b) NUHM1

Figure 5.13: The 2-D χ^2 parameter space for $(\tan\beta, m_{1/2})$ for the (a) cMSSM and (b) NUHM1 in the post-LHC regime

$(m_0, \tan\beta)$ and $(\tan\beta, m_{1/2})$

These two planes, Figure 5.12 and Figure 5.13, show that the bifurcation in the cMSSM is also present in $\tan\beta$, though the separation is proportionately smaller with respect to the scale of the variable. It is therefore expected that with dedicated sampling in the intervening region ($\tan\beta \sim 45$) that this separation could be removed, though a bi-modal behavior of the χ^2 function would still be present.

The high $m_{1/2}$ low m_0 region in the NUHM1 can be identified as the separate but large grouping of points in the 95% CL region for $5 < \tan\beta < 30$, again suggesting bimodal behavior and therefore different processes satisfying the DM constraints.

Figure 5.13 shows the presence of the light higgs funnel in both models, importantly now separate from the main mass of points, but these figures demonstrate the independence of this funnel from $\tan\beta$. This independence of both m_0 and $\tan\beta$ explains why such a funnel is not clearly evident in Figure 5.12.

Figure 5.12 demonstrates that if the models are constrained to $m_0 > 2000$GeV then

[8] `MicrOMEGAs`, `DarkSUSY`, `SuperIso`, `SSARD`

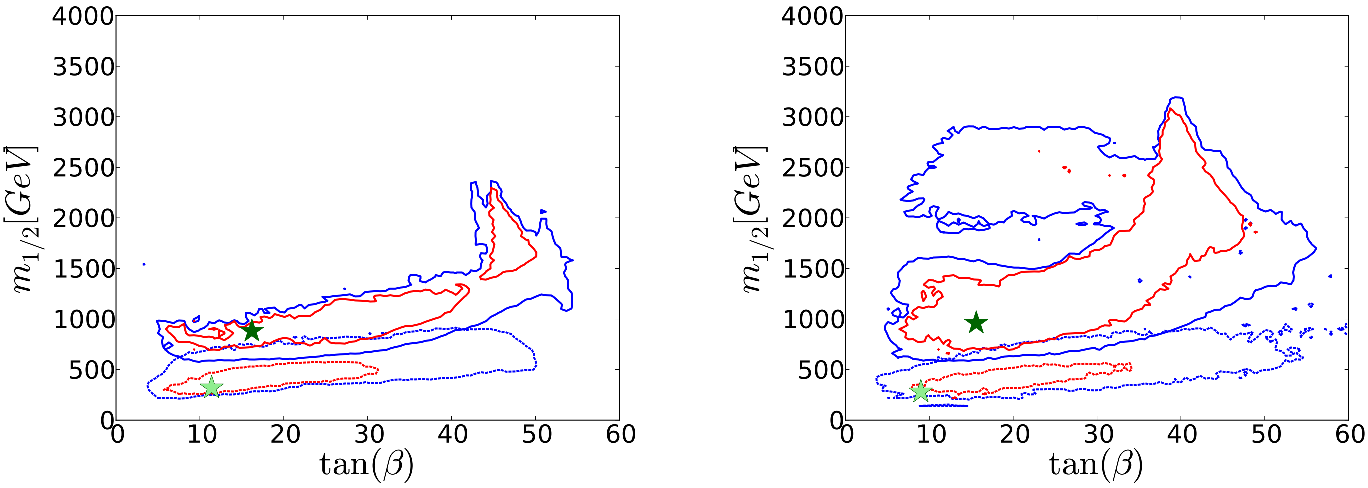

(a) cMSSM (b) NUHM1

Figure 5.14: $(\tan\beta, m_{1/2})$ parameter space comparing pre-LHC (dotted) and post-LHC (solid) 68% CL (red) and 95% CL (blue) regions for the (a) cMSSM and (b) NUHM1

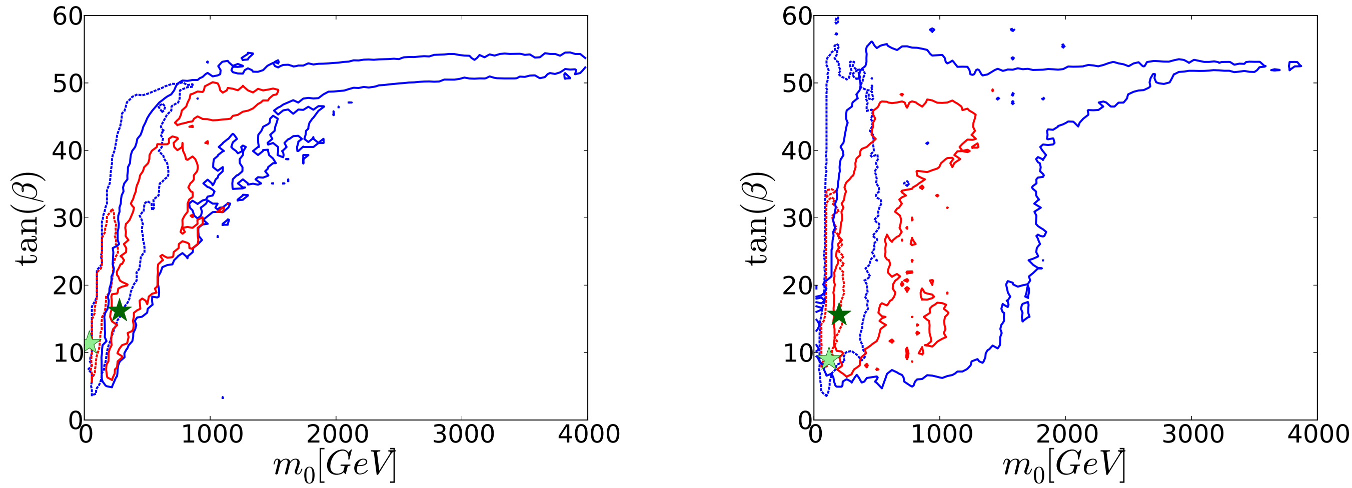

(a) cMSSM (b) NUHM1

Figure 5.15: $(m_0, \tan\beta)$ parameter space comparing pre-LHC (dotted) and post-LHC (solid) 68% CL (red) and 95% CL (blue) regions for the (a) cMSSM and (b) NUHM1

correspondingly high $\tan\beta$ is required in range $45 < \tan\beta < 55$, with the χ^2 rising rapidly on the edges of this region.

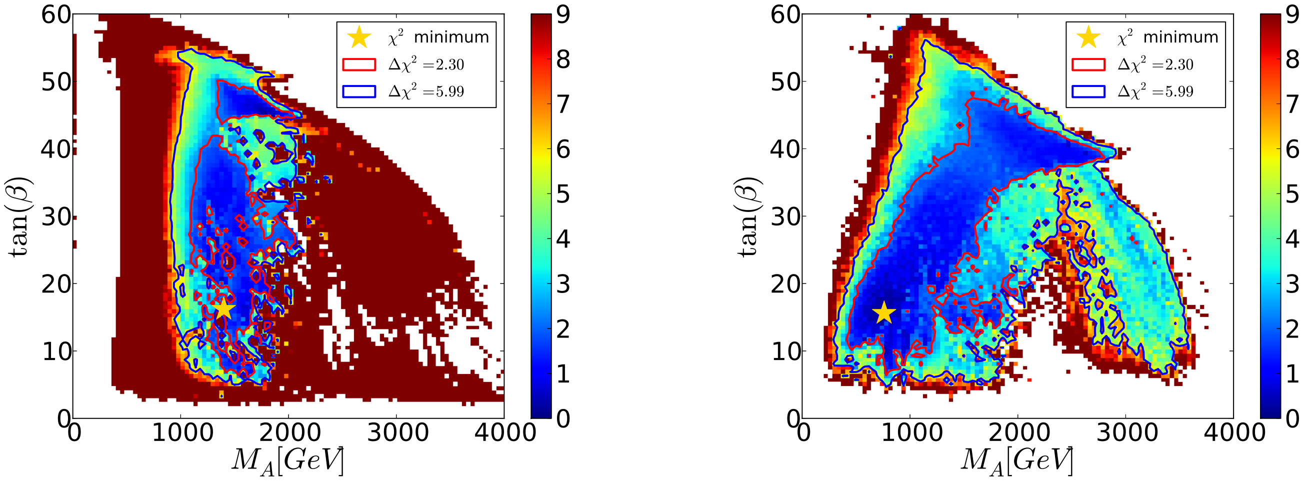

(a) cMSSM (b) NUHM1

Figure 5.16: The 2-D χ^2 parameter space for $(m_A, \tan\beta)$ for the (a) cMSSM and (b) NUHM1 in the post-LHC regime

$(m_A, \tan\beta)$

In Figure 5.16 we expect to see combined impacts from the heavy higgs searches, constraints on $BR(B_s^0 \to \mu\mu)$, and the direct searches for SUSY. The direct searches for SUSY being independent of $\tan\beta$ push the mass scale for M_A up. For higher masses we require a correspondingly higher value of $\tan\beta$. The heavy higgs search from CMS rules out regions of high $\tan\beta$ and low M_A, though after the application of the direct search constraints most of this parameter space is already disfavored and so these searches only impact the edges of the contours. Finally the $BR(B_s^0 \to \mu\mu)$ combination places upper bounds on a combination of M_A and $\tan\beta$ as evidenced by the cut off for high $\tan\beta$ and high M_A in both models where the 68% CL and 95% CL contours closely follow the same line.

At 95% CL the cMSSM is comparatively quite restrictive, allowing $1000 < M_A < 2000$GeV, but the extra freedom of the NUHM1 allows for $400 < M_A < 3500$GeV.

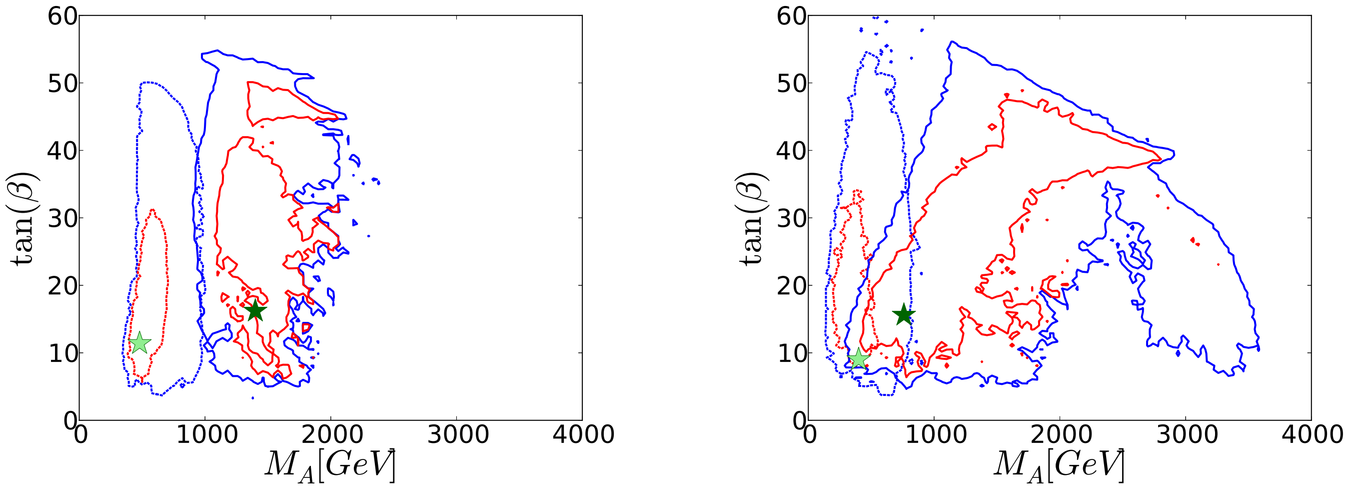

(a) cMSSM (b) NUHM1

Figure 5.17: $(m_{\mathrm{A}}, \tan\beta)$ parameter space comparing pre-LHC (dotted) and post-LHC (solid) 68% CL (red) and 95% CL (blue) regions for the (a) cMSSM and (b) NUHM1

$\left(m_{\tilde{\chi}_1^0}, \sigma_p^{\mathrm{SI}}\right)$

In Figure 5.18 we expect to see the major changes with respect to the pre-LHC era, i.e. the difference between contours in Figure 5.19, originating from a combination of the direct searches and the Xenon direct dark matter searches. The direct searches, by pushing the sparticles to higher masses in $m_{1/2}$ directly raise the preferred masses of the $\tilde{\chi}_1^0$ while also reducing the cross-section σ_p^{SI}. The Xenon constraint, while most sensitive to neutralinos with $m_{\tilde{\chi}_1^0} \sim 100\text{GeV}$ has an impact up to $m_{\tilde{\chi}_1^0} < 1000\text{GeV}$, though the collaboration does not provide results beyond this, as such the displayed region is truncated here.

In the cMSSM, Figure 5.18a, the light higgs funnel is visible for $m_{\tilde{\chi}_1^0} \sim 60\text{GeV}$ where the least disfavored region corresponds to the $m_0 \sim 4000\text{GeV}$ region in the $(m_0, m_{1/2})$ plane. In both models we see a strong preference for $\sigma_p^{\mathrm{SI}} < 10^{-46}\text{cm}^2$, though in the NUHM1 for $m_{\tilde{\chi}_1^0} \sim 1000\text{GeV}$ there is an upper region extending to $\sigma_p^{\mathrm{SI}} \lesssim 10^{-44}\text{cm}^2$ with the upper limit of this being consistent with the highest impact of the Xenon limit for these values of $m_{\tilde{\chi}_1^0}$. It should also be noted that this light higgs funnel region continues to exist up to high values of m_0 where the conditions for EWSB break down. Noting

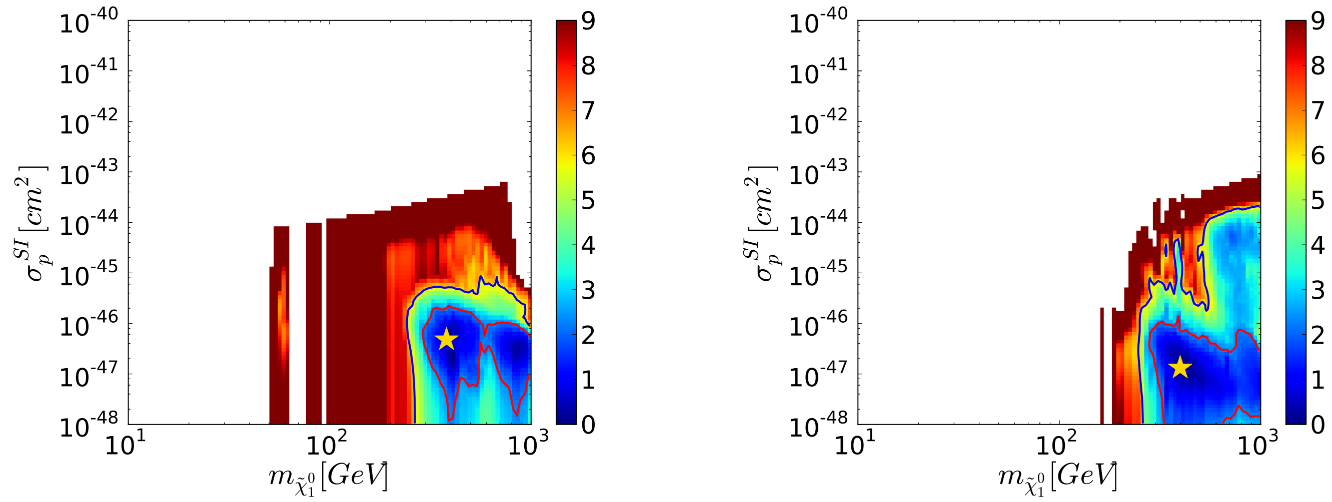

(a) cMSSM

(b) NUHM1

Figure 5.18: The 2-D χ^2 parameter space for $\left(m_{\tilde{\chi}_1^0}, \sigma_p^{\mathrm{SI}}\right)$ for the (a) cMSSM and (b) NUHM1 in the post-LHC regime

that $m_{\mathrm{h}^0} \simeq 121\mathrm{GeV}$ in the funnel, this region is not strongly disfavored by the LHC light higgs constraints, as such one expects this funnel to continue to be present in future analyses.

The bifurcation noted in the cMSSM is not as strongly present replaced by a bimodality in the 68% CL region, due to the log-binning of the plot.

5.4.2 Observables

The figures presented in this section are made up of two contours. One dashed, representing the global χ^2 function without the LHC-era constraints, and one solid representing the global χ^2 function after the LHC constraints have been applied.

The bifurcation of the 68% CL region in the cMSSM is apparent in Figure 5.21, and the bimodality is present in Figures figs. 5.22 to 5.24. For values such as $m_{\tilde{\mathrm{g}}}$, which are determined by $m_{1/2}$, the $\Delta\chi^2$ in the region between the two focal points is sufficiently large to mean there are no points within the 68% CL. Whereas, one can find points in this intermediate region that are contained in the 68% CL contour for observables

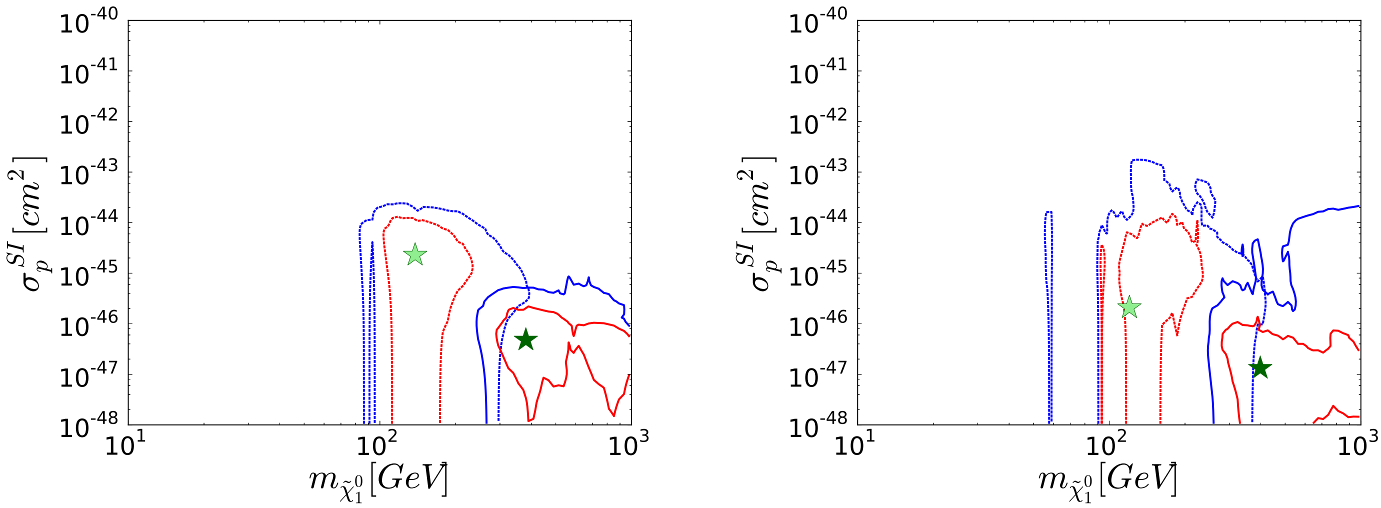

(a) cMSSM (b) NUHM1

Figure 5.19: $\left(m_{\tilde{\chi}_1^0}, \sigma_p^{\mathrm{SI}}\right)$ parameter space comparing pre-LHC (dotted) and post-LHC (solid) 68% CL (red) and 95% CL (blue) regions for the (a) cMSSM and (b) NUHM1

determined by m_0 . This is because for all values of m_0, up to the highest edge of the upper 68% CL contour in Figure 5.10a, there exist points with $\Delta\chi^2 < 2.3$.

As suggested it seems likely that dedicated sampling in this region could find points with $\Delta\chi^2 < 2.3$ and hence restore the 68% CL region to a single contour. However these figures also show the bimodality exists in both models, where there are two distinct preferred regions: one low mass region where the global minimum resides, and a second higher mass region where the $\Delta\chi^2$ value declines. The separation of these two regions of the χ^2 function is mainly driven by the dark matter constraint and hence is more strongly present in observables dependent on $m_{1/2}$ as this input determines $m_{\tilde{\chi}_1^0}$.

$\mathbf{m_{h^0}}$

In Figure 5.20, it is important to note that the $\Delta\chi^2$ functions are generated *without* the constraints on m_{h^0} from LEP and the LHC experiments. This allows the assessment of a models natural preference for the lightest higgs mass. The $\Delta\chi^2$ functions after the LHC constraints have been applied is shown with a red-band denoting the 1.5GeV theoretical

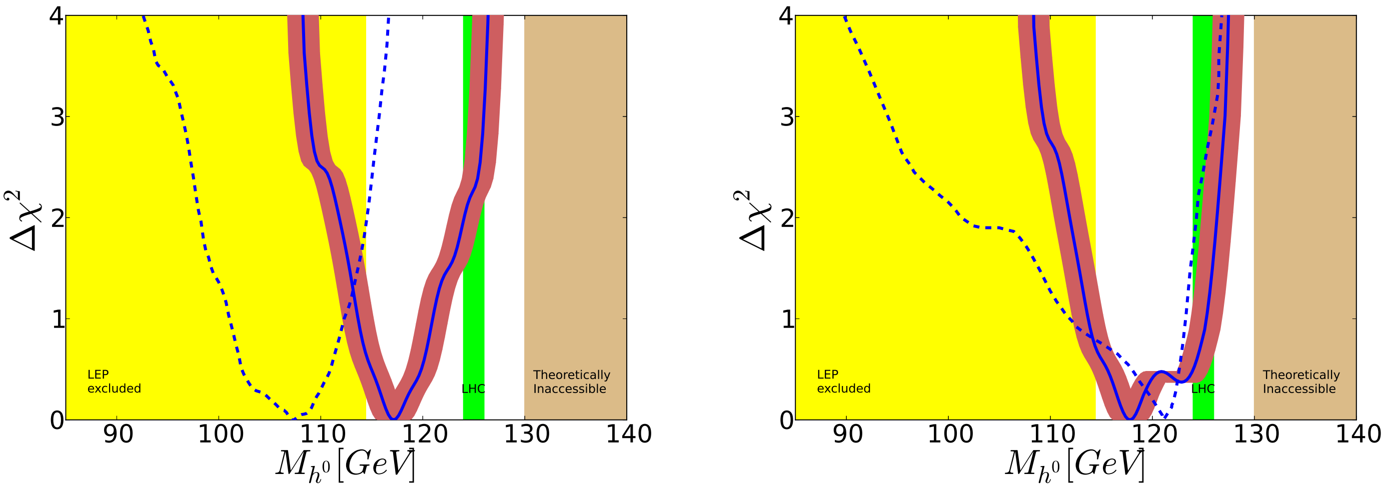

(a) cMSSM (b) NUHM1

Figure 5.20: The 1-D $\Delta\chi^2$ functions for m_{h^0} pre-LHC (dashed) and post-LHC (solid) for (a) cMSSM and (b) NUHM1

uncertainty in the calculation of m_{h^0}. The provisional measurement of 125 ± 1GeV is shown with a green band, and the yellow region demarcates the LEP lower limit of 114.4GeV.

In the case of the NUHM1, Figure 5.20b, we see that the model tolerates a broad range of m_{h^0} for $\Delta\chi^2 < 4$, where $90 < m_{h^0} < 127$GeV, before the LHC constraints are applied. Though after the constraints, while the range has significantly tightened ($110 < m_{h^0} < 127$GeV), the preferred value has dropped. There should not be too much significance attached to this, as there are values with $\Delta\chi^2 < 0.5$ in the range $113 < m_{h^0} < 126$GeV due to the $\Delta\chi^2$ function being relatively flat across large regions of parameter space.

In the cMSSM the preferred value begins around $m_{h^0} = 109$GeV, and allows a much narrower range $93 < m_{h^0} < 116$GeV than in the NUHM1. After the search exclusions are applied a similar width band of $109 < m_{h^0} < 126$GeV centered around $m_{h^0} = 118$GeV is allowed at $\Delta\chi^2 < 4$.

Both models show the ability to produce a light higgs with a mass consistent with the LHC results with $\Delta\chi^2 < 2$.

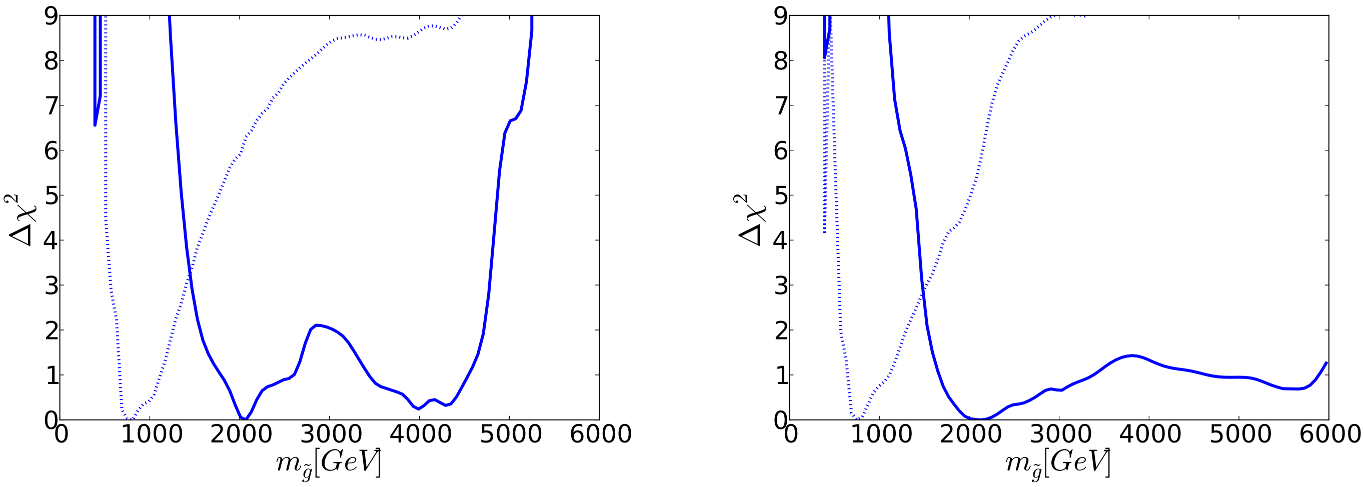

(a) cMSSM (b) NUHM1

Figure 5.21: 1-D $\Delta\chi^2$ functions for $m_{\tilde{g}}$, pre-LHC constraints (dashed lines) and post-LHC constraints (solid lines) for (a) cMSSM and (b) NUHM1

$\mathbf{m_{\tilde{g}}}$

Figure 5.21 shows the one-dimensional $\Delta\chi^2$ function for the gluino mass. For the cMSSM and the NUHM1 in the pre-LHC regime, the preferred value of $m_{1/2}$ is ~ 300GeV and corresponds to the favored value of $m_{\tilde{g}} \sim 700$GeV. After the LHC constraints have been applied and the bimodality emerges, the low mass global minimum is at $m_{\tilde{g}} \sim 2$TeV, with the higher mass secondary minimum at $m_{\tilde{g}} \sim 4$TeV and $m_{\tilde{g}} \sim 5.5$TeV in the cMSSM and NUHM1 respectively. While the χ^2 rises steeply after this second minimum in the cMSSM, the NUHM1 tolerates $m_{\tilde{g}} \gtrsim 6$TeV with $\Delta\chi^2 < 2$. The steep rise in the χ^2 in the cMSSM suggests the possibility of future tension in the model arising from direct searches at higher center of mass energies and the direct dark matter searches. However in the NUHM1 the extra freedom allowing the adjustment of M_A allows regions which maintain $M_A \sim 2m_{\tilde{\chi}_1^0}$ and thereby remove the χ^2 impact of the constraint on $\Omega_c h^2$.

In both models there is a small region at $m_{\tilde{g}} \sim 400$GeV where $5.99 < \Delta\chi^2 < 9$. This is the remnants of the light higgs funnel, discussed earlier in Section 5.2.4, and is the only region with $m_{\tilde{g}} < 1$TeV remaining where $\Delta\chi^2 < 9$.

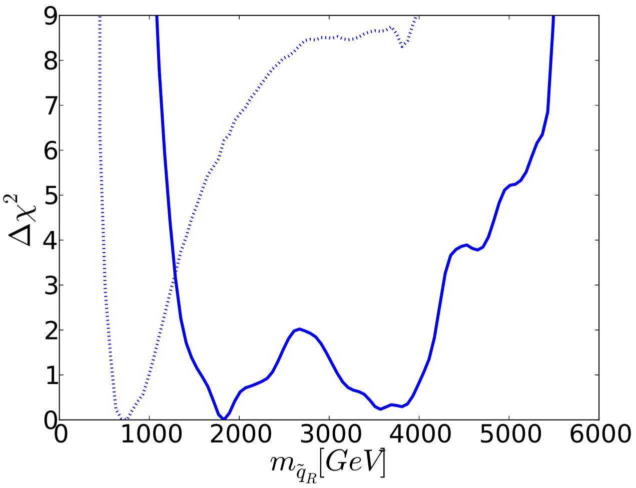

(a) cMSSM

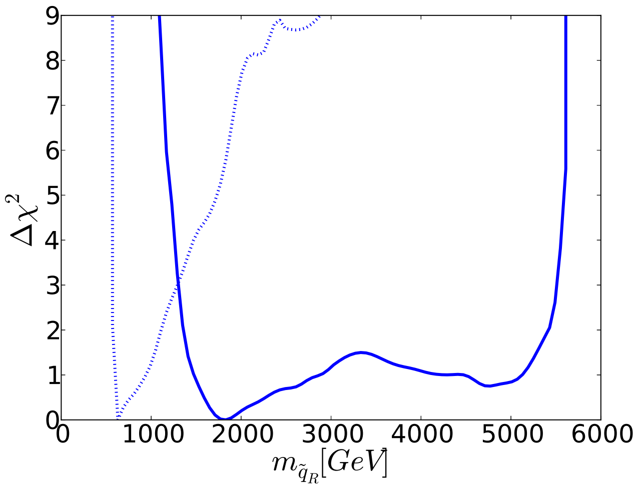

(b) NUHM1

Figure 5.22: 1-D $\Delta\chi^2$ functions for $m_{\tilde{q}_R}$, pre-LHC constraints (dashed lines) and post-LHC constraints (solid lines) for (a) cMSSM and (b) NUHM1

$\mathbf{m_{\tilde{q}_R}}$

Figure 5.22 displays the 1D $\Delta\chi^2$ function for the *average* mass of the super-partners of the five lightest right handed quarks. In both models the preferred value before the LHC constraints are applied is $m_{\tilde{q}_R} \sim 700$GeV with the post-LHC global minimum being $m_{\tilde{q}_R} \sim 2$TeV, and the higher mass secondary minimum at $m_{\tilde{q}_R} \sim 5$TeV and $m_{\tilde{q}_R} \sim 4$TeV in the NUHM1 and cMSSM respectively. In both models the χ^2 rises rapidly at $m_{\tilde{q}_R} \sim 5.5$TeV, corresponding to the similar allowed range of $m_0 \lesssim 4$TeV as in Figure 5.1. All regions of the parameter space with $m_{\tilde{q}_R} < 1$TeV are disfavored with $\Delta\chi^2 > 9$.

$\mathbf{m_{\tilde{t}_1}}$

The $\Delta\chi^2$ functions for the lightest of the two stop-quarks is shown in Figure 5.23. As with the $\Delta\chi^2$ function for $m_{\tilde{q}_R}$ both models have a similar preferred value, before the LHC constraints are applied, of $m_{\tilde{t}_1} \sim 500$GeV. Once the LHC constraints have been applied the models show different preferred masses. The NUHM1's global minimum

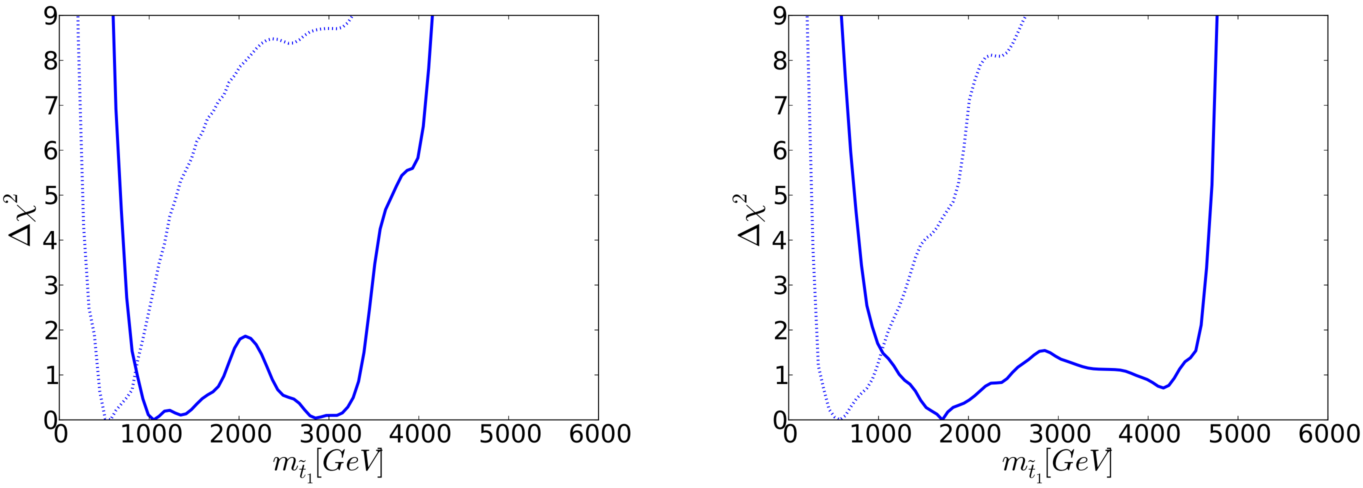

(a) cMSSM (b) NUHM1

Figure 5.23: 1-D $\Delta\chi^2$ functions for $m_{\tilde{t}_1}$, pre-LHC constraints (dashed lines) and post-LHC constraints (solid lines) for (a) cMSSM and (b) NUHM1

is $m_{\tilde{t}_1} \sim 2$TeV, whereas the cMSSM has a lower preferred value $m_{\tilde{t}_1} \sim 1$TeV. The NUHM1 and cMSSM have higher mass secondary minima of $m_{\tilde{t}_1} \sim 4$TeV and $m_{\tilde{t}_1} \sim 3$TeV respectively. At $\Delta\chi^2 < 9$ both models tolerate $m_{\tilde{t}_1} > 500$GeV, with the NUHM1 having all points with $\Delta\chi^2 > 9$ for $m_{\tilde{t}_1} > 4.8$TeV and the similarly the cMSSM for $m_{\tilde{t}_1} > 4.2$TeV.

$\mathbf{m_{\tilde{\tau}_1}}$

Figure 5.24 shows the $\Delta\chi^2$ function for the $\tilde{\tau}_1$. In this observable, an almost direct correspondence to the preferred and allowed ranges of m_0 is present. The minima begin at $m_{\tilde{\tau}_1} \sim 150$GeV for both models, with the lower mass global minima after the LHC constraints at $m_{\tilde{\tau}_1} \sim 400$GeV and the secondary minima at $m_{\tilde{\tau}_1} \sim 1$TeV. In both models $m_{\tilde{\tau}_1} \gtrsim 3$TeV is disfavored with $\Delta\chi^2 > 9$.

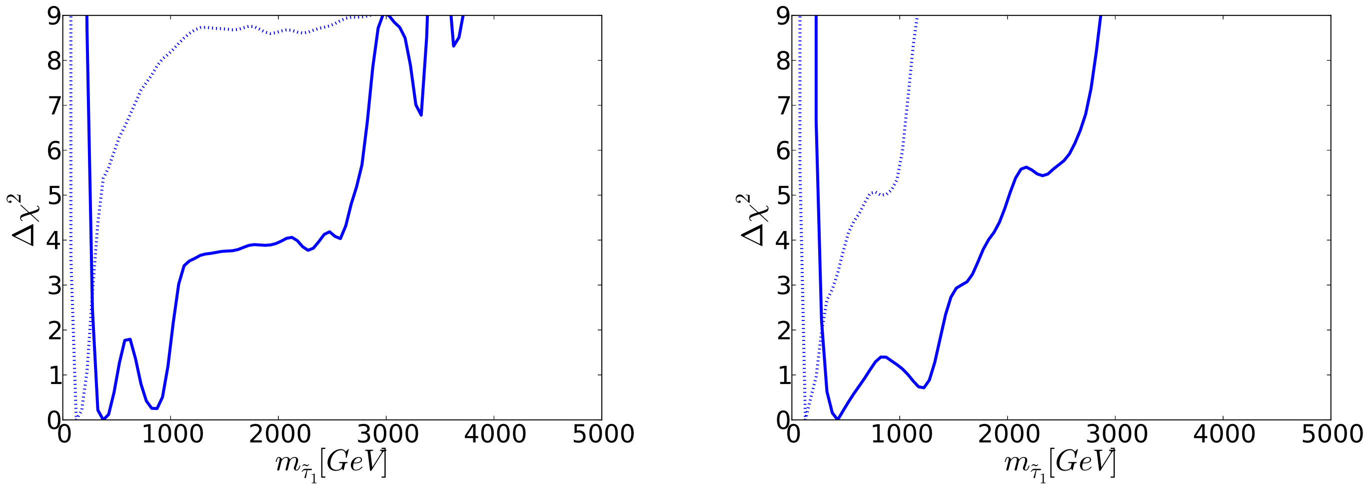

(a) cMSSM

(b) NUHM1

Figure 5.24: 1-D $\Delta\chi^2$ functions for $m_{\tilde{\tau}_1}$, pre-LHC constraints (dashed lines) and post-LHC constraints (solid lines) for (a) cMSSM and (b) NUHM1

$\mathbf{BR}\left(\mathbf{B_s^0} \to \boldsymbol{\mu\mu}\right)$

The one dimensional $\Delta\chi^2$ for the value of $\mathrm{BR}\left(\mathrm{B_s^0} \to \mu\mu\right)$ as a fraction of the SM value is shown in Figure 5.25. Both models, both before and after application of the LHC constraints, prefer values of $\mathrm{BR}\left(\mathrm{B_s^0} \to \mu\mu\right) \sim 1 \times \mathrm{BR}\left(\mathrm{B_s^0} \to \mu\mu\right)^{\mathrm{SM}}$. The main impact of the searches is to constrain the upper values allowed in the models. Before constraints are applied, the NUHM1 has a very shallow minima, tolerating values of $\mathrm{BR}\left(\mathrm{B_s^0} \to \mu\mu\right) > 3 \times \mathrm{BR}\left(\mathrm{B_s^0} \to \mu\mu\right)^{\mathrm{SM}}$ for $\Delta\chi^2 < 2$. Similarly the cMSSM allows for a more compressed range, though allowing similar values at $\Delta\chi^2 < 5$. After the application of the constraints both models disfavor $\mathrm{BR}\left(\mathrm{B_s^0} \to \mu\mu\right) > 2.25 \times \mathrm{BR}\left(\mathrm{B_s^0} \to \mu\mu\right)^{\mathrm{SM}}$ at $\Delta\chi^2 > 9$. There remains no significant discriminating feature between the two models in this observable, and both show a steep minimum around the SM value.

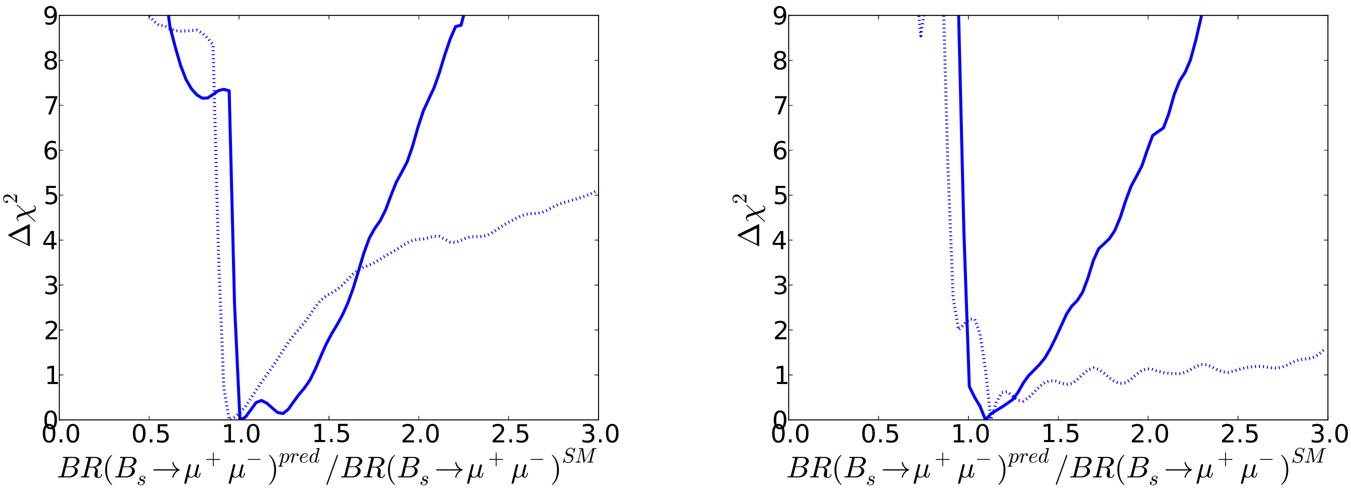

(a) cMSSM (b) NUHM1

Figure 5.25: 1-D $\Delta\chi^2$ functions for $\mathrm{BR}(\mathrm{B}_s^0 \to \mu\mu)$, pre-LHC constraints (dashed lines) and post-LHC constraints (solid lines) for (a) cMSSM and (b) NUHM1

5.5 Impact of LHC-era constraints

In the pre-LHC regime both models strongly prefer low masses, mostly driven by the $(g_\mu - 2)$ constraint. Though low values of $\tan\beta$ are preferred, there is a broad allowed range of values. As a result the models favour squarks and gluinos with $m \sim$ 700GeV.

The direct SUSY searches rule out a great deal of the low mass parameter spaces, forcing the masses of both squarks and gluinos up above 1TeV in both models. The main culprit of $E_{\mathrm{T}}^{\mathrm{miss}}$ signatures that SUSY could produce, the neutralino, is also disfavored strongly for masses $m_{\tilde{\chi}_1^0} < 200\mathrm{GeV}$. There is current strong interest in compressed spectra and third generation models within the experimental and theoretical communities[9] with some interest in the possibility of light stops. In both models stops with $m_{\tilde{t}_1} < 500\mathrm{GeV}$ are also strongly disfavored.

The Xenon constraints on the combination of $\left(m_{\tilde{\chi}_1^0}, \sigma_p^{\mathrm{SI}}\right)$ compounds the effect of the direct SUSY searches by pushing the models to higher neutralino masses and lower cross-

[9]see the presentation of results in these models in Section 4.14.2

sections ruling out $\sigma_p^{\mathrm{SI}} > 2 \times 10^{-44}(1 \times 10^{-45})$ in the NUHM1(cMSSM).

The combined effect of the direct searches for SUSY and DM is to strongly disfavour all low mass regions other than a small region of the light higgs funnel which remains. As the models are pushed to higher masses a bimodality forms caused by the necessity of satisfying the constraint on $\Omega_c h^2$. This bimodality is less obvious in the NUHM1 where we have explicit control of M_A and so can maintain the rapid annihilation funnel through a larger region of the $\left(m_0, m_{1/2}\right)$ parameter space.

The heavy higgs searches serve to limit the maximum value of $\tan\beta$ that is reasonable for a particular mass M_A, however a large portion of the parameter space that these searches would impact is also excluded by the direct SUSY searches ruling out low masses. Again due to the added freedom of $m_{H_{1,2}}$ in the NUHM1 these searches serve to rule out regions where the decoupling would have allowed the NUHM1 to keep lower m_A than allowed in the cMSSM due to the direct SUSY searches.

While we have seen the first measurement of $\mathrm{BR}\left(\mathrm{B_s^0} \to \mu\mu\right)$ this largely serves to increase the cost in χ^2 for going to higher values of $\tan\beta$ without significantly impacting the preferred region of parameter space, given that the preferred region has a value consistent with the observation.

Interestingly, when looking at the models without the constraints on the Higgs mass, Figure 5.20, it is clear that the models can be entirely consistent with the recent Higgs search announcements, and in the case of the NUHM1 a secondary local minimum is found at $m_{\mathrm{h^0}} \simeq 125\mathrm{GeV}$. In the case of the cMSSM the impact of the other searches is to push the preferred Higgs mass closer to $m_{\mathrm{h^0}} = 125\mathrm{GeV}$.

In a more general sense the strongest impact of the searches of the LHC-era is to significantly reduce the P-values associated with the best-fit points of each of the models, Table 5.3. Using just the pre-LHC constraints, both models have $P = 0.35$ with well defined minima. However in the post-LHC regime this falls to $P \simeq 0.08$ with the minima being flat over large ranges of all input parameters. While, as discussed in Section 5.1.1 the frequentist interpretation does not support the statement that the model is excluded at 92% CL, only that the model has $P = 0.08$. It should also be noted that as discussed in Section 5.1.4 the specific value of P should not given undue weighting, only comparative values of P in the same analysis where the same set of constraints have been used between models should be considered. As mentioned it is possible to drastically alter the value of P by adding arbitrary constraints that the model may have zero sensitivity to. However by adding these constraints into consideration the value of n_{dof} is increased with no corresponding change to χ^2 thereby forcing P to decrease.

While there exists tension in these models, between for instance m_{h^0} , $\big(g_\mu - 2\big)$, and the direct searches, it is clear that even at full design energy the LHC is unlikely to be able to probe the outer extents of the current 95% CL regions in either model and therefore is unlikely to further reduce the P-value to any great extent. The usefulness of these models as benchmarks for future searches and analyses is therefore in question.

Chapter 6

Conclusion

This document has detailed a search for supersymmetry in all hadronic final states using the kinematic variable α_T with $4.98\text{fb}^{-1}$of data recorded by the CMS detector at center of mass energy $\sqrt{s} = 7\text{TeV}$ splitting the signal region by the scalar sum of the transverse energy of jets and the number of jets identified as originating from a b-quark. A fit to the SM background expectation was performed, and no significant excess was observed. The results of this search have been presented in the context of the cMSSM where we set $A_0 = 0$ and $\tan\beta = 10$ and find that at 95% CL $m_{1/2} \lesssim 630\text{GeV}$ for low m_0 and $m_{1/2} \lesssim 300\text{GeV}$ at high m_0 are excluded. Also, the result have been shown in multiple third-generation and compressed spectra simplified models. With squark pair production 1^{st} and 2^{nd} generation squarks are excluded for $m_{\tilde{q}} < 750\text{GeV}$ for low m_{LSP}, and bottom squarks are excluded up to approximately 500GeV.

This analysis shows no apparent evidence of SUSY in the 7TeVdataset, however the limits imposed do not significantly reduce the hopes of discovering SUSY with a $E_{\text{T}}^{\text{miss}}$ signature due to a large regions of parameter space with $m_{\text{LSP}} < 1\text{TeV}$ still being unconstrained.

Following this an analysis of the parameter space of both the cMSSM and NUHM1 has been presented. Both electroweak precision measurement and LHC-era direct searches have been applied to the parameter spaces, with particular attention paid to the impact of the LHC-era searches. While obviously the lack of a significant SUSY signal in the searches means that the fit probability of the models is significantly reduced ($\sim 9\%$ in both models) the main result is the flattening of the likelihood and the emergence of a bimodality. We see that in both models the main tension defining this bimodality comes from the constraints on the relic dark matter abundance, combined with the higher mass scales enforced by the direct searches. One would expect that further encroachment into the lower mass regions of the parameter space to begin to remove the lower section of the bimodality leaving only the heavy higgs rapid annihilation funnel region, and thereby further flattening the likelihood. It should be noted that with sufficient further sampling the obvious delineation of the two modes would likely disappear due to the flattening of the global χ^2 function. Given that the NUHM1 provides a region at low m_0 not accessible in the cMSSM, where multiple processes combine to satisfy the relic abundance constraint, it would be prudent, though computationally complex, to investigate the NUHM2. Here the decoupling of $m_{H_{1,2}}$ allows for even greater control over the neutralino masses (allowing us to exchange the bino-like neutralino LSP for a higgsino-like neutralino LSP) and hence is likely to open up a much richer variation of phenomenology that remaining consistent with other constraints.

In short, though there has been no direct evidence of SUSY-like BSM physics thus far, and the impact of the LHC-era searches on models like the cMSSM and the NUHM1 have been significant, even these constrained sub-models of the MSSM still provide rich enough phenomenology to allow for regions of parameter space that could be still compatible with current observations while remaining out of reach of the current generation of searches.

Bibliography

[1] Information about this code is available from K.A. Olive; it contains important contributions from T.Falk, G.Ganis, A. Mustafayev, J. McDonald, K.A. Olive, P. Sandick, Y. Santoso and M. Snednicki.

[2] In: *JINST 3 S08005* (2008). DOI: `doi:10.1088/1748-0221/3/08/S08005`.

[3] *CMS, the Compact Muon Solenoid. Muon technical design report.* 1997.

[4] "Precision Electroweak Measurements and Constraints on the Standard Model". In: (2010). arXiv: `1012.2367 [hep-ex]`.

[5] Georges Aad et al. "Observation of a new particle in the search for the Standard Model Higgs boson with the ATLAS detector at the LHC". In: *Phys.Lett.* B716 (2012), pp. 1–29. DOI: `10.1016/j.physletb.2012.08.020`. arXiv: `1207.7214 [hep-ex]`.

[6] Georges Aad et al. "Search for squarks and gluinos using final states with jets and missing transverse momentum with the ATLAS detector in $\sqrt{s} = 7$ TeV proton-proton collisions". In: *Phys.Lett.* B701 (2011), pp. 186–203. DOI: `10.1016/j.physletb.2011.05.061`. arXiv: `1102.5290 [hep-ex]`.

[7] Georges Aad et al. "Search for squarks and gluinos with the ATLAS detector in final states with jets and missing transverse momentum using $4.7 fb^{-1}$ of $\sqrt{s} = 7$ TeV proton-proton collision data". In: *Phys.Rev.* D87 (2013), p. 012008. DOI: `10.1103/PhysRevD.87.012008`. arXiv: `1208.0949 [hep-ex]`.

[8] Georges Aad et al. "Search for squarks and gluinos with the ATLAS detector in final states with jets and missing transverse momentum using $4.7 fb^{-1}$ of $\sqrt{s} = 7$ TeV proton-proton collision data". In: *Phys.Rev.* D87 (2013), p. 012008. DOI: `10.1103/PhysRevD.87.012008`. arXiv: `1208.0949 [hep-ex]`.

[9] Georges Aad et al. "Search for the decay $B_s^0 \to \mu\mu$ with the ATLAS detector". In: *Phys.Lett.* B713 (2012), pp. 387–407. DOI: 10.1016/j.physletb.2012.06.013. arXiv: 1204.0735 [hep-ex].

[10] Georges Aad et al. "Search for the Standard Model Higgs boson in the H to $\tau^+\tau^-$ decay mode in $\sqrt{s} = 7$ TeV pp collisions with ATLAS". In: *JHEP* 1209 (2012), p. 070. DOI: 10.1007/JHEP09(2012)070. arXiv: 1206.5971 [hep-ex].

[11] R Aaij et al. "First evidence for the decay $B_s \to \mu^-\mu^-$". In: (2012). arXiv: 1211.2674.

[12] T. Aaltonen et al. "Inclusive Search for Squark and Gluino Production in $p\bar{p}$ Collisions at $\sqrt{s} = 1.96$ TeV". In: *Phys. Rev. Lett.* 102 (12 Mar. 2009), p. 121801. DOI: 10.1103/PhysRevLett.102.121801. URL: http://link.aps.org/doi/10.1103/PhysRevLett.102.121801.

[13] V.M. Abazov et al. "Search for squarks and gluinos in events with jets and missing transverse energy using 2.1 fb^{-1} of $p\bar{p}$ collision data at $\sqrt{s} = 1.96$ TeV". In: *Phys.Lett.* B660 (2008), pp. 449–457. DOI: 10.1016/j.physletb.2008.01.042. arXiv: 0712.3805 [hep-ex].

[14] S Abdullin et al. "The Fast Simulation of the CMS Detector at LHC". In: *Journal of Physics: Conference Series* 331.3 (2011), p. 032049. URL: http://stacks.iop.org/1742-6596/331/i=3/a=032049.

[15] S. Agostinelli et al. "GEANT4: A Simulation toolkit". In: *Nucl.Instrum.Meth.* A506 (2003), pp. 250–303. DOI: 10.1016/S0168-9002(03)01368-8.

[16] B.C. Allanach. "SOFTSUSY: a program for calculating supersymmetric spectra". In: *Comput.Phys.Commun.* 143 (2002), pp. 305–331. DOI: 10.1016/S0010-4655(01)00460-X. arXiv: hep-ph/0104145 [hep-ph].

[17] Johan Alwall et al. "MadGraph 5 : Going Beyond". In: *JHEP* 1106 (2011), p. 128. DOI: 10.1007/JHEP06(2011)128. arXiv: 1106.0522 [hep-ph].

[18] G. E. Andrews, R. Askey, and R. Roy. *Special Functions*. Vol. 71. Encyclopedia of Mathematics and its Applications. Cambridge: Cambridge University Press, 1999.

[19] Mario Antonelli et al. "Precision tests of the Standard Model with leptonic and semileptonic kaon decays". In: (2008). arXiv: 0801.1817 [hep-ph].

[20] E. Aprile et al. "Dark Matter Results from 100 Live Days of XENON100 Data". In: *Phys.Rev.Lett.* 107 (2011), p. 131302. DOI: 10.1103/PhysRevLett.107.131302. arXiv: 1104.2549 [astro-ph.CO].

[21] E. Aprile et al. "Dark Matter Results from 225 Live Days of XENON100 Data". In: *Phys.Rev.Lett.* 109 (2012), p. 181301. DOI: 10.1103/PhysRevLett.109.181301. arXiv: 1207.5988 [astro-ph.CO].

[22] A.V. Artamonov et al. "New measurement of the $K^+ \to \pi^+ \nu\bar{\nu}$ branching ratio". In: *Phys.Rev.Lett.* 101 (2008), p. 191802. DOI: 10.1103/PhysRevLett.101.191802. arXiv: 0808.2459 [hep-ex].

[23] D. Asner et al. "Averages of b-hadron, c-hadron, and τ-lepton Properties". In: (2010). arXiv: 1010.1589 [hep-ex].

[24] R. Barate et al. "Search for the standard model Higgs boson at LEP". In: *Phys.Lett.* B565 (2003), pp. 61–75. DOI: 10.1016/S0370-2693(03)00614-2. arXiv: hep-ex/0306033 [hep-ex].

[25] G. Belanger et al. "Indirect search for dark matter with micrOMEGAs2.4". In: *Comput.Phys.Commun.* 182 (2011), pp. 842–856. DOI: 10.1016/j.cpc.2010.11.033. arXiv: 1004.1092 [hep-ph]; G. Belanger et al. "MicrOMEGAs 2.0: A Program to calculate the relic density of dark matter in a generic model". In: *Comput.Phys.Commun.* 176 (2007), pp. 367–382. DOI: 10.1016/j.cpc.2006.11.008. arXiv: hep-ph/0607059 [hep-ph].

[26] G.W. Bennett et al. "Final Report of the Muon E821 Anomalous Magnetic Moment Measurement at BNL". In: *Phys.Rev.* D73 (2006), p. 072003. DOI: 10.1103/PhysRevD.73.072003. arXiv: hep-ex/0602035 [hep-ex]; G.W. Bennett et al. "Measurement of the negative muon anomalous magnetic moment to 0.7 ppm". In: *Phys.Rev.Lett.* 92 (2004), p. 161802. DOI: 10.1103/PhysRevLett.92.161802. arXiv: hep-ex/0401008 [hep-ex].

[27] *b-Jet Identification in the CMS Experiment*. Tech. rep. CMS-PAS-BTV-11-004. Geneva: CERN, 2012.

[28] Christoph Bobeth, Andrzej J. Buras, and Thorsten Ewerth. "$B \to X_s \ell^+ \ell^-$ in the MSSM at NNLO". In: *Nucl.Phys.* B713 (2005), pp. 522–554. DOI: 10.1016/j.nuclphysb.2005.02.011. arXiv: hep-ph/0409293 [hep-ph].

[29] M. Bona et al. "Model-independent constraints on Δ F=2 operators and the scale of new physics". In: *JHEP* 0803 (2008), p. 049. DOI: 10.1088/1126-6708/2008/03/049. arXiv: 0707.0636 [hep-ph].

[30] J. R. Bond and A. S. Szalay. "The collisionless damping of density fluctuations in an expanding universe". In: *The Astrophysical Journal* 274 (Nov. 1983), pp. 443–468. DOI: 10.1086/161460.

[31] Oliver Sim Brüning et al. "LHC Design Report". In: (2004).

[32] O. Buchmueller et al. "Higgs and Supersymmetry". In: *Eur.Phys.J.* C72 (2012), p. 2020. DOI: 10.1140/epjc/s10052-012-2020-3. arXiv: 1112.3564 [hep-ph].

[33] O. Buchmueller et al. "Supersymmetry and Dark Matter in Light of LHC 2010 and Xenon100 Data". In: *Eur.Phys.J.* C71 (2011), p. 1722. DOI: 10.1140/epjc/s10052-011-1722-2. arXiv: 1106.2529 [hep-ph].

[34] O. Buchmueller et al. "Supersymmetry in Light of 1/fb of LHC Data". In: *Eur.Phys.J.* C72 (2012), p. 1878. DOI: 10.1140/epjc/s10052-012-1878-4. arXiv: 1110.3568 [hep-ph].

[35] O. Buchmueller et al. "The CMSSM and NUHM1 in Light of 7 TeV LHC, $B_s to \mu +\mu -$ and XENON100 Data". In: *Eur.Phys.J.* C72 (2012), p. 2243. DOI: 10.1140/epjc/s10052-012-2243-3. arXiv: 1207.7315 [hep-ph].

[36] A.J. Buras et al. "epsilon-prime / epsilon and rare K and B decays in the MSSM". In: *Nucl.Phys.* B592 (2001), pp. 55–91. DOI: 10.1016/S0550-3213(00)00582-4. arXiv: hep-ph/0007313 [hep-ph].

[37] Andrzej J. Buras et al. "On the Standard Model prediction for $BR(B_{s,d} \to \mu^+\mu^-)$". In: *Eur.Phys.J.* C72 (2012), p. 2172. DOI: 10.1140/epjc/s10052-012-2172-1. arXiv: 1208.0934 [hep-ph].

[38] Matteo Cacciari, Gavin P. Salam, and Gregory Soyez. "The anti- k t jet clustering algorithm". In: *Journal of High Energy Physics* 2008.04 (2008), p. 063. URL: http://stacks.iop.org/1126-6708/2008/i=04/a=063.

[39] John M. Campbell, J.W. Huston, and W.J. Stirling. "Hard Interactions of Quarks and Gluons: A Primer for LHC Physics". In: *Rept.Prog.Phys.* 70 (2007), p. 89. DOI: 10.1088/0034-4885/70/1/R02. arXiv: hep-ph/0611148 [hep-ph].

[40] Serguei Chatrchyan et al. "Identification of b-quark jets with the CMS experiment". In: *JINST* 8 (2013), P04013. DOI: 10.1088/1748-0221/8/04/P04013. arXiv: 1211.4462 [hep-ex].

[41] Serguei Chatrchyan et al. "Observation of a new boson at a mass of 125 GeV with the CMS experiment at the LHC". In: *Phys.Lett.* B716 (2012), pp. 30–61. DOI: 10.1016/j.physletb.2012.08.021. arXiv: 1207.7235 [hep-ex].

[42] Serguei Chatrchyan et al. "Search for neutral Higgs bosons decaying to τ pairs in pp collisions at $\sqrt{s} = 7$ TeV". In: *Phys.Lett.* B713 (2012), pp. 68–90. DOI: 10.1016/j.physletb.2012.05.028. arXiv: 1202.4083 [hep-ex].

[43] Serguei Chatrchyan et al. "Search for supersymmetry in final states with missing transverse energy and 0, 1, 2, or at least 3 b-quark jets in 7 TeV pp collisions using the variable alphaT". In: *JHEP* 1301 (2013), p. 077. DOI: 10.1007/JHEP01(2013)077. arXiv: 1210.8115 [hep-ex].

[44] CMS Collaboration. "Determination of jet energy calibration and transverse momentum resolution in CMS". In: *Journal of Instrumentation* 6 (Nov. 2011), p. 11002. DOI: 10.1088/1748-0221/6/11/P11002. arXiv: 1107.4277 [physics.ins-det].

[45] CDF Collaboration. *Tevatron heavy flavour results.* Feb. 2012. URL: https://indico.cern.ch/getFile.py/access?contribId=28&sessionId=7&resId=1&materialId=slides&confId=143360.

[46] The ATLAS Collaboration. "The ATLAS Experiment at the CERN Large Hadron Collider". In: *JINST 3 S08003* (2008). DOI: doi:10.1088/1748-0221/3/08/S08003.

[47] Glen Cowan et al. "Asymptotic formulae for likelihood-based tests of new physics". English. In: *The European Physical Journal C* 71 (2 2011), pp. 1–19. ISSN: 1434-6044. DOI: 10.1140/epjc/s10052-011-1554-0. URL: http://dx.doi.org/10.1140/epjc/s10052-011-1554-0.

[48] G. D'Ambrosio et al. "Minimal flavor violation: An Effective field theory approach". In: *Nucl.Phys.* B645 (2002), pp. 155–187. DOI: 10.1016/S0550-3213(02)00836-2. arXiv: hep-ph/0207036 [hep-ph]; Marcela S. Carena et al. "$b \to s\gamma$ and supersymmetry with large tan Beta". In: *Phys.Lett.* B499 (2001), pp. 141–146. DOI: 10.1016/S0370-2693(01)00009-0. arXiv: hep-ph/0010003 [hep-ph]; G. Degrassi, P. Gambino, and G.F. Giudice. "$B \to X(sgamma)$ in supersymmetry: Large contributions beyond the leading order". In: *JHEP* 0012 (2000), p. 009. arXiv: hep-ph/0009337 [hep-ph]; Marco Ciuchini et al. "Next-to-leading QCD corrections to $B \to X_s\gamma$ in supersymmetry". In: *Nucl.Phys.* B534 (1998), pp. 3–20. DOI: 10.1016/S0550-3213(98)00516-1. arXiv: hep-ph/9806308 [hep-ph]; M. Misiak et al. "Estimate of $BR(B \to X_s\gamma)$ at $O(\alpha_s^2)$". In: *Phys.Rev.Lett.* 98 (2007), p. 022002. DOI: 10.1103/PhysRevLett.98.022002. arXiv: hep-ph/0609232 [hep-ph].

[49] *Data-Driven Estimation of the Invisible Z Background to the SUSY MET Plus Jets Search*. Tech. rep. CMS-PAS-SUS-08-002. 2009. Geneva: CERN, Jan. 2009.

[50] Michel Davier et al. "Reevaluation of the Hadronic Contributions to the Muon g-2 and to alpha(MZ)". In: *Eur.Phys.J.* C71 (2011), p. 1515. DOI: 10.1140/epjc/s10052-012-1874-8,10.1140/epjc/s10052-010-1515-z. arXiv: 1010.4180 [hep-ph].

[51] Kristof De Bruyn et al. "Branching Ratio Measurements of B_s Decays". In: *Phys.Rev.* D86 (2012), p. 014027. DOI: 10.1103/PhysRevD.86.014027. arXiv: 1204.1735 [hep-ph].

[52] S. Dimopoulos, S. Raby, and Frank Wilczek. "Supersymmetry and the scale of unification". In: *Phys. Rev. D* 24 (6 Sept. 1981), pp. 1681–1683. DOI: 10.1103/PhysRevD.24.1681. URL: http://link.aps.org/doi/10.1103/PhysRevD.24.1681.

[53] Savas Dimopoulos and Howard Georgi. "Softly broken supersymmetry and SU(5)". In: *Nuclear Physics B* 193.1 (1981), pp. 150–162. ISSN: 0550-3213. DOI: 10.1016/0550-3213(81)90522-8.

[54] P. A. M. Dirac. "The Quantum Theory of the Electron". In: *Royal Society of London Proceedings Series A* 117 (Feb. 1928), pp. 610–624. DOI: 10.1098/rspa.1928.0023; P. A. M. Dirac. "A Theory of Electrons and Protons". In: *Royal Society of London Proceedings Series A* 126 (Jan. 1930), pp. 360–365. DOI: 10.1098/rspa.1930.0013.

[55] Manuel Drees and Mihoko M. Nojiri. "The Neutralino relic density in minimal $N = 1$ supergravity". In: *Phys.Rev.* D47 (1993), pp. 376–408. DOI: 10.1103/PhysRevD.47.376. arXiv: hep-ph/9207234 [hep-ph].

[56] J. Dunkley et al. "Five-Year Wilkinson Microwave Anisotropy Probe (WMAP) Observations: Likelihoods and Parameters from the WMAP data". In: *Astrophys. J. Suppl.* 180 (2009), pp. 306–329. DOI: 10.1088/0067-0049/180/2/306. arXiv: arXiv:astro-ph/0803.0586 [astro-ph].

[57] John R. Ellis, Dimitri V. Nanopoulos, and K. Tamvakis. "Grand Unification in Simple Supergravity". In: *Phys.Lett.* B121 (1983), p. 123. DOI: 10.1016/0370-2693(83)90900-0.

[58] John R. Ellis et al. "Exploration of the MSSM with nonuniversal Higgs masses". In: *Nucl.Phys.* B652 (2003), pp. 259–347. DOI: 10.1016/S0550-3213(02)01144-6. arXiv: hep-ph/0210205 [hep-ph].

[59] John R. Ellis et al. "Phenomenological constraints on patterns of supersymmetry breaking". In: *Phys.Lett.* B573 (2003), pp. 162–172. DOI: 10.1016/j.physletb.2003.08.056. arXiv: hep-ph/0305212 [hep-ph].

[60] John R. Ellis et al. "Very constrained minimal supersymmetric standard models". In: *Phys.Rev.* D70 (2004), p. 055005. DOI: 10.1103/PhysRevD.70.055005. arXiv: hep-ph/0405110 [hep-ph].

[61] J. Ellis et al. "Phenomenological constraints on patterns of supersymmetry breaking". In: *Physics Letters B* 573 (Oct. 2003), pp. 162–172. DOI: 10.1016/S0370-2693(03)01319-4. eprint: arXiv:hep-ph/0305212.

[62] F. Englert and R. Brout. "Broken Symmetry and the Mass of Gauge Vector Mesons". In: *Phys. Rev. Lett.* 13 (9 Aug. 1964), pp. 321–323. DOI: 10.1103/PhysRevLett.13.321. URL: http://link.aps.org/doi/10.1103/PhysRevLett.13.321.

[63] L. Evans and P. Bryant. "LHC machine". In: *Journal of Instrumentation* 3 (2008), S08001.

[64] Enrico Fermi. "Tentativo di una Teoria Dei Raggi β". Italian. In: *Il Nuovo Cimento* 11.1 (1934), pp. 1–19. ISSN: 0029-6341. DOI: 10.1007/BF02959820. URL: http://dx.doi.org/10.1007/BF02959820.

[65] M. Frank et al. "The Higgs Boson Masses and Mixings of the Complex MSSM in the Feynman-Diagrammatic Approach". In: *JHEP* 0702 (2007), p. 047. DOI: 10.1088/1126-6708/2007/02/047. arXiv: hep-ph/0611326 [hep-ph]; S. Heinemeyer, W. Hollik, and G. Weiglein. "FeynHiggs: A Program for the calculation of the masses of the neutral CP even Higgs bosons in the MSSM". In: *Comput.Phys.Commun.* 124 (2000), pp. 76–89. DOI: 10.1016/S0010-4655(99)00364-1. arXiv: hep-ph/9812320 [hep-ph]; S. Heinemeyer, W. Hollik, and G. Weiglein. "The Masses of the neutral CP - even Higgs bosons in the MSSM: Accurate analysis at the two loop level". In: *Eur.Phys.J.* C9 (1999), pp. 343–366. DOI: 10.1007/s100529900006. arXiv: hep-ph/9812472 [hep-ph]; G. Degrassi et al. "Towards high precision predictions for the MSSM Higgs sector". In: *Eur.Phys.J.*

C28 (2003), pp. 133–143. DOI: 10.1140/epjc/s2003-01152-2. arXiv: hep-ph/0212020 [hep-ph].

[66] Stefano Frixione, Paolo Nason, and Carlo Oleari. "Matching NLO QCD computations with Parton Shower simulations: the POWHEG method". In: *JHEP* 0711 (2007), p. 070. DOI: 10.1088/1126-6708/2007/11/070. arXiv: 0709.2092 [hep-ph].

[67] G. Gabrielse et al. "New Determination of the Fine Structure Constant from the Electron g Value and QED". In: *Phys. Rev. Lett.* 97 (3 July 2006), p. 030802. DOI: 10.1103/PhysRevLett.97.030802. URL: http://link.aps.org/doi/10.1103/PhysRevLett.97.030802.

[68] M. Gell-Mann. "The interpretation of the new particles as displaced charge multiplets". English. In: *Il Nuovo Cimento* 4.2 (1956), pp. 848–866. ISSN: 0029-6341. DOI: 10.1007/BF02748000. URL: http://dx.doi.org/10.1007/BF02748000.

[69] J. Goldstone. "Field theories with Superconductor solutions". English. In: *Il Nuovo Cimento* 19.1 (1961), pp. 154–164. ISSN: 0029-6341. DOI: 10.1007/BF02812722. URL: http://dx.doi.org/10.1007/BF02812722.

[70] Jeffrey Goldstone, Abdus Salam, and Steven Weinberg. "Broken Symmetries". In: *Phys. Rev.* 127 (3 Aug. 1962), pp. 965–970. DOI: 10.1103/PhysRev.127.965. URL: http://link.aps.org/doi/10.1103/PhysRev.127.965.

[71] D. Griffiths. *Introduction to Elementary Particles*. Physics Textbook. Wiley, 2008. ISBN: 9783527406012. URL: http://books.google.co.uk/books?id=w9Dz56myXm8C.

[72] David J. Gross and Frank Wilczek. "Ultraviolet Behavior of Non-Abelian Gauge Theories". In: *Phys. Rev. Lett.* 30 (26 June 1973), pp. 1343–1346. DOI: 10.1103/PhysRevLett.30.1343. URL: http://link.aps.org/doi/10.1103/PhysRevLett.30.1343.

[73] The Tevatron Electroweak Working Group. "Combination of CDF and D0 Results on the Mass of the Top Quark Using Up to 5.6 fb^{-1} of Data". In: (2010). arXiv: 1007.3178 [hep-ex].

[74] G. S. Guralnik, C. R. Hagen, and T. W. B. Kibble. "Global Conservation Laws and Massless Particles". In: *Phys. Rev. Lett.* 13 (20 Nov. 1964), pp. 585–587. DOI: 10.1103/PhysRevLett.13.585. URL: http://link.aps.org/doi/10.1103/PhysRevLett.13.585.

[75] Robert V. Harlander and William B. Kilgore. "Higgs boson production in bottom quark fusion at next-to-next-to leading order". In: *Phys.Rev.* D68 (2003), p. 013001. DOI: 10.1103/PhysRevD.68.013001. arXiv: hep-ph/0304035 [hep-ph].

[76] S. Heinemeyer et al. "*Z* Pole Observables in the MSSM". In: *JHEP* 0804 (2008), p. 039. DOI: 10.1088/1126-6708/2008/04/039. arXiv: 0710.2972 [hep-ph]; S. Heinemeyer et al. "Precise prediction for M(W) in the MSSM". In: *JHEP* 0608 (2006), p. 052. DOI: 10.1088/1126-6708/2006/08/052. arXiv: hep-ph/0604147 [hep-ph].

[77] Peter W. Higgs. "Broken Symmetries and the Masses of Gauge Bosons". In: *Phys. Rev. Lett.* 13 (16 Oct. 1964), pp. 508–509. DOI: 10.1103/PhysRevLett.13.508. URL: http://link.aps.org/doi/10.1103/PhysRevLett.13.508.

[78] Peter W. Higgs. "Spontaneous Symmetry Breakdown without Massless Bosons". In: *Phys. Rev.* 145 (4 May 1966), pp. 1156–1163. DOI: 10.1103/PhysRev.145.1156. URL: http://link.aps.org/doi/10.1103/PhysRev.145.1156.

[79] G.'t Hooft. "Naturalness, Chiral Symmetry, and Spontaneous Chiral Symmetry Breaking". English. In: *Recent Developments in Gauge Theories*. Ed. by G.'t Hooft et al. Vol. 59. NATO Advanced Study Institutes Series. Springer US, 1980, pp. 135–157. ISBN: 978-1-4684-7573-9. DOI: 10.1007/978-1-4684-7571-5_9. URL: http://dx.doi.org/10.1007/978-1-4684-7571-5_9.

[80] Gino Isidori et al. "Flavour physics at large tan(beta) with a Bino-like LSP". In: *Phys.Rev.* D75 (2007), p. 115019. DOI: 10.1103/PhysRevD.75.115019. arXiv: hep-ph/0703035 [HEP-PH]; Gino Isidori and Paride Paradisi. "Hints of large tan(beta) in flavour physics". In: *Phys.Lett.* B639 (2006), pp. 499–507. DOI: 10.1016/j.physletb.2006.06.071. arXiv: hep-ph/0605012 [hep-ph].

[81] F. James and M. Roos. "Minuit: A System for Function Minimization and Analysis of the Parameter Errors and Correlations". In: *Comput.Phys.Commun.* 10 (1975), pp. 343–367. DOI: 10.1016/0010-4655(75)90039-9.

[82] S.F Joglekar. "S-matrix derivation of the Weinberg model". In: *Annals. Phys.* 83 (1974), pp. 427–428.

[83] V Karimäki. *The CMS tracker system project: Technical Design Report*. Technical Design Report CMS. Geneva: CERN, 1997.

[84] Vardan Khachatryan et al. "Search for Supersymmetry in pp Collisions at 7 TeV in Events with Jets and Missing Transverse Energy". In: *Phys.Lett.* B698 (2011), pp. 196–218. DOI: 10.1016/j.physletb.2011.03.021. arXiv: 1101.1628 [hep-ex].

[85] T. W. B. Kibble. "Symmetry Breaking in Non-Abelian Gauge Theories". In: *Phys. Rev.* 155 (5 Mar. 1967), pp. 1554–1561. DOI: 10.1103/PhysRev.155.1554. URL: http://link.aps.org/doi/10.1103/PhysRev.155.1554.

[86] E. Komatsu et al. "Seven-Year Wilkinson Microwave Anisotropy Probe (WMAP) Observations: Cosmological Interpretation". In: *Astrophys.J.Suppl.* 192 (2011), p. 18. DOI: 10.1088/0067-0049/192/2/18. arXiv: 1001.4538 [astro-ph.CO].

[87] LHC. *Accelerators and Technology Sector*. Mar. 2013. URL: https://espace.cern.ch/acc-tec-sector/.

[88] Vittorio Lubicz and Cecilia Tarantino. "Flavour physics and Lattice QCD: Averages of lattice inputs for the Unitarity Triangle Analysis". In: *Nuovo Cim.* B123 (2008), pp. 674–688. DOI: 10.1393/ncb/i2008-10650-3. arXiv: 0807.4605 [hep-lat].

[89] F. Mahmoudi. "SuperIso v2.3: A Program for calculating flavor physics observables in Supersymmetry". In: *Comput.Phys.Commun.* 180 (2009), pp. 1579–1613. DOI: 10.1016/j.cpc.2009.02.017. arXiv: 0808.3144 [hep-ph].

[90] Stephen P. Martin. "A Supersymmetry primer". In: (1997). arXiv: hep-ph/9709356 [hep-ph].

[91] Stephen P. Martin and Michael T. Vaughn. "Two loop renormalization group equations for soft supersymmetry breaking couplings". In: *Phys.Rev.* D50 (1994), p. 2282. DOI: 10.1103/PhysRevD.50.2282, 10.1103/PhysRevD.78.039903. arXiv: hep-ph/9311340 [hep-ph].

[92] Bryn Mathias. "Search for supersymmetry in pp collisions with all-hadronic final states using the α_T variable with the CMS detector at the LHC". In: (2013).

[93] N. Metropolis et al. "Equation of State Calculations by Fast Computing Machines". In: *Journal of Chemical Physics* 21 (June 1953), pp. 1087–1092. DOI: 10.1063/1.1699114.

[94] S. Myers and E. Picasso. "The Design, construction and commissioning of the CERN Large Electron Positron collider". In: *Contemp.Phys.* 31 (1990), pp. 387–403. DOI: 10.1080/00107519008213789.

[95] Tadao Nakano and Kazuhiko Nishijima. "Charge Independence for V-particles". In: *Progress of Theoretical Physics* 10.5 (1953), pp. 581–582. DOI: 10.1143/PTP.10.581. URL: http://ptp.ipap.jp/link?PTP/10/581/.

[96] B. Odom et al. "New Measurement of the Electron Magnetic Moment Using a One-Electron Quantum Cyclotron". In: *Phys. Rev. Lett.* 97 (3 July 2006), p. 030801. DOI: 10.1103/PhysRevLett.97.030801. URL: http://link.aps.org/doi/10.1103/PhysRevLett.97.030801.

[97] S. Ovyn, X. Rouby, and V. Lemaitre. "DELPHES, a framework for fast simulation of a generic collider experiment". In: (2009). arXiv: 0903.2225 [hep-ph].

[98] M.M. Pavan et al. "The Pion nucleon Sigma term is definitely large: Results from a G.W.U. analysis of pi nucleon scattering data". In: *PiN Newslett.* 16 (2002), pp. 110–115. arXiv: hep-ph/0111066 [hep-ph].

[99] Michael E. Peskin and Daniel V. Schroeder. *An Introduction to Quantum Field Theory.* Cambridge, Massachusetts: Perseus Books, 1995.

[100] Joaquim Prades, Eduardo de Rafael, and Arkady Vainshtein. "Hadronic Light-by-Light Scattering Contribution to the Muon Anomalous Magnetic Moment". In: (2009). arXiv: 0901.0306 [hep-ph]; Fred Jegerlehner and Andreas Nyffeler. "The Muon g-2". In: *Phys.Rept.* 477 (2009), pp. 1–110. DOI: 10.1016/j.physrep.2009.04.003. arXiv: 0902.3360 [hep-ph]; M. Davier et al. "Reevaluation of the hadronic contribution to the muon magnetic anomaly using new $e^+e^- \to \pi^+\pi^-$ cross section data from BABAR". In: *Eur.Phys.J.* C66 (2010), pp. 1–9. DOI: 10.1140/epjc/s10052-010-1246-1. arXiv: 0908.4300 [hep-ph]; Joaquim Prades. "Standard Model Prediction of the Muon Anomalous Magnetic Moment". In: *Acta Phys.Polon.Supp.* 3 (2010), pp. 75–86. arXiv: 0909.2546 [hep-ph]; T. Teubner et al. "Update of g-2 of the Muon and Delta Alpha". In: *Chin.Phys.* C34 (2010), pp. 728–734. DOI: 10.1088/1674-1137/34/6/019. arXiv: 1001.5401 [hep-ph]; James P. Miller, Eduardo de Rafael, and B. Lee Roberts. "Muon (g-2): Experiment and theory". In: *Rept.Prog.Phys.* 70 (2007), p. 795. DOI: 10.1088/0034-4885/70/5/R03. arXiv: hep-ph/0703049 [hep-ph]; Dominik Stockinger. "The Muon Magnetic Moment and Supersymmetry". In: *J.Phys.* G34 (2007), R45–R92. DOI: 10.1088/0954-3899/34/2/R01. arXiv: hep-ph/0609168 [hep-ph].

[101] Lisa Randall and David Tucker-Smith. “Dijet Searches for Supersymmetry at the LHC”. In: *Phys.Rev.Lett.* 101 (2008), p. 221803. DOI: 10.1103/PhysRevLett.101.221803. arXiv: 0806.1049 [hep-ph].

[102] A L Read. “Modified frequentist analysis of search results (the CL_s method)”. In: CERN-OPEN-2000-205 (2000).

[103] A L Read. “Presentation of search results: the CL_s technique”. In: *Journal of Physics G: Nuclear and Particle Physics* 28.10 (2002), p. 2693. URL: http://stacks.iop.org/0954-3899/28/i=10/a=313.

[104] Tai Sakuma. *3D SketchUp images of the CMS detector*. Apr. 2013. URL: https://twiki.cern.ch/twiki/bin/view/CMSPublic/SketchUpCMS.

[105] S. Schael et al. “Search for neutral MSSM Higgs bosons at LEP”. In: *Eur.Phys.J.* C47 (2006), pp. 547–587. DOI: 10.1140/epjc/s2006-02569-7. arXiv: hep-ex/0602042 [hep-ex].

[106] E. Schrödinger. “An Undulatory Theory of the Mechanics of Atoms and Molecules”. In: *Phys. Rev.* 28 (6 Dec. 1926), pp. 1049–1070. DOI: 10.1103/PhysRev.28.1049. URL: http://link.aps.org/doi/10.1103/PhysRev.28.1049.

[107] E. Schrödinger. “Quantisierung als Eigenwertproblem”. In: *Annalen der Physik* 385.13 (1926), pp. 437–490. ISSN: 1521-3889. DOI: 10.1002/andp.19263851302. URL: http://dx.doi.org/10.1002/andp.19263851302.

[108] “Search for $B_s^0 \to \mu^+\mu^-$ and $B_0 \to \mu^+\mu^-$ decays”. In: *Journal of High Energy Physics* 2012 (4 2012). DOI: 10.1007/JHEP04(2012)033.

[109] “Search for supersymmetry with the α_{T} variable in the 7 TeV dataset of 2011”. In: CMS-AN-11-517 (2011).

[110] Nathan Seiberg. “Naturalness versus supersymmetric non-renormalization theorems”. In: *Physics Letters B* 318.3 (1993), pp. 469–475. ISSN: 0370-2693. DOI: 10.1016/0370-2693(93)91541-T. URL: http://www.sciencedirect.com/science/article/pii/037026939391541T.

[111] *Simple extrapolations for supersymmetry discovery limits at different LHC centre-of-mass energies and luminosities based on inclusive searches with the ATLAS detector*. Tech. rep. ATL-PHYS-PUB-2011-003. Geneva: CERN, Jan. 2011.

[112] Torbjorn Sjostrand, Stephen Mrenna, and Peter Z. Skands. “PYTHIA 6.4 Physics and Manual”. In: *JHEP* 0605 (2006), p. 026. DOI: 10.1088/1126-6708/2006/05/026. arXiv: hep-ph/0603175 [hep-ph].

[113] D. N. Spergel et al. “First-Year Wilkinson Microwave Anisotropy Probe (WMAP) Observations: Determination of Cosmological Parameters”. In: *The Astrophysical Journal Supplement Series* 148.1 (2003), p. 175. URL: http://stacks.iop.org/0067-0049/148/i=1/a=175.

[114] Dominik Stockinger. “The Muon Magnetic Moment and Supersymmetry”. In: *J.Phys.* G34 (2007), R45–R92. DOI: 10.1088/0954-3899/34/2/R01. arXiv: hep-ph/0609168 [hep-ph].

[115] K. Symanzik. “Small distance behaviour in field theory and power counting”. English. In: *Communications in Mathematical Physics* 18.3 (1970), pp. 227–246. ISSN: 0010-3616. DOI: 10.1007/BF01649434. URL: http://dx.doi.org/10.1007/BF01649434.

[116] Gerard ’t Hooft. “Renormalization of Massless Yang-Mills Fields”. In: *Nucl.Phys.* B33 (1971), pp. 173–199. DOI: 10.1016/0550-3213(71)90395-6.

[117] “The ALICE experiment at the CERN LHC”. In: *JINST 3 S08002* (2008). DOI: 10.1088/1748-0221/3/08/S08002.

[118] The CMS Collaboration. *CMS PAS BTV 09 001 Algorithms for b-Jet identification in CMS.*

[119] *The CMS electromagnetic calorimeter project: Technical Design Report.* Technical Design Report CMS. Geneva: CERN, 1997.

[120] “The CMS experiment at the CERN LHC”. In: *JINST 3 S08004* (2008). DOI: doi:10.1088/1748-0221/3/08/S08004.

[121] *The CMS hadron calorimeter project: Technical Design Report.* Technical Design Report CMS. Geneva: CERN, 1997.

[122] *The CMS magnet project: Technical Design Report.* Technical Design Report CMS. Geneva: CERN, 1997.

[123] R. Trotta et al. “The impact of priors and observables on parameter inferences in the constrained MSSM”. In: *Journal of High Energy Physics* 12 (Dec. 2008), pp. 24–+. DOI: 10.1088/1126-6708/2008/12/024. arXiv: arXiv:hep-ph/0809.3792.

[124] Steven Weinberg. “A Model of Leptons”. In: *Phys. Rev. Lett.* 19 (21 Nov. 1967), pp. 1264–1266. DOI: 10.1103/PhysRevLett.19.1264. URL: http://link.aps.org/doi/10.1103/PhysRevLett.19.1264; Nobelstiftelsen. *Elementary particle theory: Relativistic groups and analyticity. Proccedings of the Eighth Nobel*

Symposium held May 19-25, 1968 at Aspenäsgarden, Lerum, in the county of Älvsborg, Sweden. Nobel symposium. Almqvist & Wiksell, 1968. URL: http://books.google.co.uk/books?id=-UJeAAAAIAAJ; S. L. Glashow, J. Iliopoulos, and L. Maiani. "Weak Interactions with Lepton-Hadron Symmetry". In: *Phys. Rev. D* 2 (7 Oct. 1970), pp. 1285–1292. DOI: 10.1103/PhysRevD.2.1285. URL: http://link.aps.org/doi/10.1103/PhysRevD.2.1285.

[125] Steven Weinberg. "Physical Processes in a Convergent Theory of the Weak and Electromagnetic Interactions". In: *Phys. Rev. Lett.* 27 (24 Dec. 1971), pp. 1688–1691. DOI: 10.1103/PhysRevLett.27.1688. URL: http://link.aps.org/doi/10.1103/PhysRevLett.27.1688.

[126] J. Wess and B. Zumino. "Supergauge Transformations in Four-Dimensions". In: *Nucl.Phys.* B70 (1974), pp. 39–50. DOI: 10.1016/0550-3213(74)90355-1.

[127] Hideki Yukawa. "On the Interaction of Elementary Particles. I^*". In: *Progress of Theoretical Physics Supplement* 1 (1955), pp. 1–10. DOI: 10.1143/PTPS.1.1. URL: http://ptp.ipap.jp/link?PTPS/1/1/.